



Politecnico
di Bari

Repository Istituzionale dei Prodotti della Ricerca del Politecnico di Bari

Long-Lasting Nanoscale Wireless Communications with Energy-Harvesting

This is a PhD Thesis

Original Citation:

Long-Lasting Nanoscale Wireless Communications with Energy-Harvesting / Musa, Vittoria. - ELETTRONICO. - (2022).
[10.60576/poliba/iris/musa-vittoria_phd2022]

Availability:

This version is available at <http://hdl.handle.net/11589/232752> since: 2021-12-28

Published version

Politecnico di Bari
DOI: 10.60576/poliba/iris/musa-vittoria_phd2022

Terms of use:

Altro tipo di accesso

(Article begins on next page)



Department of Electrical and Information Engineering
ELECTRICAL AND INFORMATION ENGINEERING

Ph.D. Program

SSD: ING-INF/03–TELECOMMUNICATIONS

Final Dissertation

Long-Lasting Nanoscale Wireless Communications with Energy-Harvesting

by
Vittoria MUSA:

Supervisor:

Prof. Giuseppe PIRO

Coordinator of Ph.D. Program:

Prof. Mario CARPENTIERI

Course n°34, 01/11/2018-31/10/2021



LIBERATORIA PER L'ARCHIVIAZIONE DELLA TESI DI DOTTORATO

Al Magnifico Rettore
del Politecnico di Bari

Il/la sottoscritto/a Vittoria Musa nato/a a Fasano (BR) il 12/04/1994

residente a Fasano (BR) in via Vito Albano, 5 e-mail vittoria.musa94@gmail.com

iscritto al 3° anno di Corso di Dottorato di Ricerca in Ingegneria Elettrica e dell'Informazione ciclo XXXIV

ed essendo stato ammesso a sostenere l'esame finale con la prevista discussione della tesi dal titolo:

Long-Lasting Nanoscale Wireless Communications with Energy-Harvesting

DICHIARA

- 1) di essere consapevole che, ai sensi del D.P.R. n. 445 del 28.12.2000, le dichiarazioni mendaci, la falsità negli atti e l'uso di atti falsi sono puniti ai sensi del codice penale e delle Leggi speciali in materia, e che nel caso ricorressero dette ipotesi, decade fin dall'inizio e senza necessità di nessuna formalità dai benefici conseguenti al provvedimento emanato sulla base di tali dichiarazioni;
- 2) di essere iscritto al Corso di Dottorato di ricerca Ingegneria Elettrica e dell'Informazione ciclo XXXIV, corso attivato ai sensi del "Regolamento dei Corsi di Dottorato di ricerca del Politecnico di Bari", emanato con D.R. n.286 del 01.07.2013;
- 3) di essere pienamente a conoscenza delle disposizioni contenute nel predetto Regolamento in merito alla procedura di deposito, pubblicazione e autoarchiviazione della tesi di dottorato nell'Archivio Istituzionale ad accesso aperto alla letteratura scientifica;
- 4) di essere consapevole che attraverso l'autoarchiviazione delle tesi nell'Archivio Istituzionale ad accesso aperto alla letteratura scientifica del Politecnico di Bari (IRIS-POLIBA), l'Ateneo archiverà e renderà consultabile in rete (nel rispetto della Policy di Ateneo di cui al D.R. 642 del 13.11.2015) il testo completo della tesi di dottorato, fatta salva la possibilità di sottoscrizione di apposite licenze per le relative condizioni di utilizzo (di cui al sito <http://www.creativecommons.it/Licenze>), e fatte salve, altresì, le eventuali esigenze di "embargo", legate a strette considerazioni sulla tutelabilità e sfruttamento industriale/commerciale dei contenuti della tesi, da rappresentarsi mediante compilazione e sottoscrizione del modulo in calce (Richiesta di embargo);
- 5) che la tesi da depositare in IRIS-POLIBA, in formato digitale (PDF/A) sarà del tutto identica a quelle **consegnate**/inviata/da inviarsi ai componenti della commissione per l'esame finale e a qualsiasi altra copia depositata presso gli Uffici del Politecnico di Bari in forma cartacea o digitale, ovvero a quella da discutere in sede di esame finale, a quella da depositare, a cura dell'Ateneo, presso le Biblioteche Nazionali Centrali di Roma e Firenze e presso tutti gli Uffici competenti per legge al momento del deposito stesso, e che di conseguenza va esclusa qualsiasi responsabilità del Politecnico di Bari per quanto riguarda eventuali errori, imprecisioni o omissioni nei contenuti della tesi;
- 6) che il contenuto e l'organizzazione della tesi è opera originale realizzata dal sottoscritto e non compromette in alcun modo i diritti di terzi, ivi compresi quelli relativi alla sicurezza dei dati personali; che pertanto il Politecnico di Bari ed i suoi funzionari sono in ogni caso esenti da responsabilità di qualsivoglia natura: civile, amministrativa e penale e saranno dal sottoscritto tenuti indenni da qualsiasi richiesta o rivendicazione da parte di terzi;
- 7) che il contenuto della tesi non infrange in alcun modo il diritto d'Autore né gli obblighi connessi alla salvaguardia di diritti morali od economici di altri autori o di altri aventi diritto, sia per testi, immagini, foto, tabelle, o altre parti di cui la tesi è composta.

Luogo e data Fasano, 22/12/2021

Firma Vittoria Musa

Il/La sottoscritto, con l'autoarchiviazione della propria tesi di dottorato nell'Archivio Istituzionale ad accesso aperto del Politecnico di Bari (POLIBA-IRIS), pur mantenendo su di essa tutti i diritti d'autore, morali ed economici, ai sensi della normativa vigente (Legge 633/1941 e ss.mm.ii.),

CONCEDE

- al Politecnico di Bari il permesso di trasferire l'opera su qualsiasi supporto e di convertirla in qualsiasi formato al fine di una corretta conservazione nel tempo. Il Politecnico di Bari garantisce che non verrà effettuata alcuna modifica al contenuto e alla struttura dell'opera.
- al Politecnico di Bari la possibilità di riprodurre l'opera in più di una copia per fini di sicurezza, back-up e conservazione.

Luogo e data Fasano, 22/12/2021

Firma Vittoria Musa



Politecnico
di Bari

Department of Electrical and Information Engineering
ELECTRICAL AND INFORMATION ENGINEERING

Ph.D. Program

SSD: ING-INF/03–TELECOMMUNICATIONS

Final Dissertation

Long-Lasting Nanoscale Wireless Communications with Energy-Harvesting

by

Vittoria Musa:

Vittoria Musa

Referees:

Prof. Angelo Coluccia

Prof. Marco Di Renzo

Supervisor:

Prof. Giuseppe Piro

Giuseppe Piro

Coordinator of Ph.D Program:

Prof. Mario Carpentieri

Mario Carpentieri

Course n°34, 01/11/2018-31/10/2021

Declaration of Authorship

I, Vittoria MUSA, declare that this thesis titled, “Long-Lasting Nanoscale Wireless Communications with Energy-Harvesting” and the work presented in it are my own. I confirm that:

- This work was done wholly or mainly while in candidature for a research degree at this University.
- Where any part of this thesis has previously been submitted for a degree or any other qualification at this University or any other institution, this has been clearly stated.
- Where I have consulted the published work of others, this is always clearly attributed.
- Where I have quoted from the work of others, the source is always given. With the exception of such quotations, this thesis is entirely my own work.
- I have acknowledged all main sources of help.
- Where the thesis is based on work done by myself jointly with others, I have made clear exactly what was done by others and what I have contributed myself.

Signed: Vittoria Musa

Date: 22/12/2021

“Se camminassimo solo nelle giornate di sole non raggiungeremmo mai la nostra destinazione.”

Paulo Coelho

POLITECNICO DI BARI

Abstract

Faculty Name

Department of Electric and Information Engineering

Doctor of Philosophy

Long-Lasting Nanoscale Wireless Communications with Energy-Harvesting

by Vittoria MUSA

The advance of nanotechnologies recently promoted the development of nano-devices enabling promising applications in different fields. Given the restricted size of nano-devices, the scientific literature introduced two novel communication paradigms for their interaction: terahertz band communications and molecular communications. However, the design of long-lasting transmission schemes (i.e., supported by renewable energy sources) in this context still represents an open research topic. In the last years, piezoelectric nanogenerators emerged as a turning point in the design of energy-aware and energy harvesting transmission schemes at the nanoscale. Accordingly, this thesis considers their adoption in electromagnetic communications in the terahertz band and in diffusion-based molecular communications, proposing power control strategies based on feedback control theory. Here, the transmission power is dynamically set proportionally to the available energy budget by using a closed-loop control scheme. Furthermore, concerning the diffusion-based molecular communications, this thesis proposes a novel methodology for optimally tuning the number of molecules to release on a per-frame basis, while guaranteeing the simplicity of the transmission process, energy constraints and target Bit Error Rate values. To this end, the thesis also formulates an optimization problem willing to minimize an objective function depending on the available energy budget and the number of enqueued packets. Computer simulations are used to validate the formulated analytical models, depict the behavior of the proposed approaches in conceivable scenarios, and demonstrate the unique ability of the conceived approaches to ensure the expected performance level.

Contents

Declaration of Authorship	iii
Abstract	vii
Personal Scientific Contributions	1
Introduction	3
1 Introduction to the Internet of Nano-Things	7
1.1 Molecular Communications	9
1.1.1 Applications of Molecular Communications	9
Medical Applications	9
Industrial Applications	11
Environmental Applications	12
1.1.2 The Transmission Process	12
Modulation Techniques	12
Coding Techniques	13
1.1.3 The Propagation Process	15
Walkway-Based Propagation	16
Flow-Based Propagation	16
Diffusion-Based Propagation	17
1.1.4 The Reception Process	17
Receiver Models	18
Detection Techniques	19
1.1.5 Energy-Aware Molecular Communications and Energy- Harvesting Schemes	20
Energy Models for Diffusion-based Molecular Communications	20
Energy-Harvesting Techniques at the Nanoscale	21
1.2 Terahertz-Band Communications at the Nanoscale	22
1.2.1 Applications of Terahertz-Band Communications at the Nanoscale	22
Software-Defined Metamaterials	22
Wireless Robotic Materials	23
In-Body Communications	24
On-Chip Communications	24
1.2.2 The Network Layer	24

	Relaying and Forwarding Protocols	24
	Routing Protocols	25
1.2.3	The Link Layer	28
	Network Topologies for MAC Protocols	28
	Channel Access Mechanisms	29
	Initial Access Mechanisms	30
1.2.4	The Physical Layer	31
	Modulation Schemes	31
	Transmission Strategies	31
1.2.5	Energy-Harvesting and Energy-Aware Schemes for Terahertz-Band Communications	32
2	Channel Modeling and Energy-Aware Transmission Strategies for Terahertz Communications	33
2.1	The System Model	34
2.1.1	Total Signal Path Loss	34
2.1.2	Molecular Noise Temperature and Noise Power Spectral Density	38
2.1.3	The Considered Transmission Techniques	39
	The Transmission Strategies	41
2.1.4	Analysis of Physical Transmission Rates and Communication Ranges	44
	The Computed SNR	44
	The Obtained Channel Capacity	46
2.1.5	Final Considerations	48
2.2	The Control System	49
2.2.1	Transmission Scheme and Resulting Channel Capacity	49
2.2.2	The Conceived Control Law	51
	Equilibrium Point	52
	Acceptable Value for the Proportional Gain	52
	Stability Analysis	53
2.2.3	Numerical Results	54
2.2.4	Final Considerations	58
3	Feedback Control Approaches in Diffusion-Based Molecular Communications	61
3.1	The System Model	62
3.1.1	Transmission Process	62
3.1.2	Propagation Process	63
3.1.3	Reception Process	64
3.1.4	Harvesting and Discharging Processes	64
3.2	The Conceived Continuous Time Control System	65
3.2.1	Stability Analysis	67
3.2.2	Numerical Investigations	70

3.2.3	Final Considerations	72
3.3	The Conceived Discrete Time Control System	73
3.3.1	State Equation and Equilibrium Points	74
3.3.2	Analysis of the Bounds of the Proportional Gain	76
3.3.3	Stability Analysis	80
3.3.4	Impact of the Proportional Gain on Both Output Variance and Time Constant	81
3.3.5	Discussion on Implementation and Computational Complexity	83
3.3.6	Performance Evaluation	83
	Transmission Requirements	84
	Equilibrium Point vs Acceptable Values of the Proportional Gain	85
	Analysis of the State Variable at the Equilibrium	87
	Energy Consumption	88
	Achieved Performance	89
	Impact of the Duty Cycle on Both Variance of the Output and Time Constant	91
3.3.7	Final Considerations	95
4	An Optimized Transmission Scheme for Diffusion-Based Molecular Com-	
	munications	97
4.1	The Considered System Model	98
4.1.1	Reference Models for Transmitter, Propagation, and Reception .	99
4.1.2	Developed Noise Model	102
4.2	The Conceived Optimization Problem	105
4.2.1	Formulation of the Objective Function	106
4.2.2	Formulation of the Constraints	108
4.2.3	Final Formulation of the Optimization Problem	108
4.3	Numerical Results	109
4.3.1	Optimal Threshold and Minimum Voltage	110
4.3.2	Validation of the Noise Model	111
4.3.3	Behavior of the Optimization Problem	111
4.3.4	Average Performance of the Optimization Problem	114
	Voltage probability	114
	Enqueued packets	114
	Consumed Energy	117
	Resulting BER	117
4.4	Final Considerations	120
	Conclusions	121
	Acknowledgements	123
	Bibliography	125

List of Figures

1.1	The main models used for transmission, propagation, and reception processes in molecular communications field.	9
1.2	Main applications of molecular communications.	10
1.3	Possible modulation techniques.	14
1.4	Three main receiver models.	18
1.5	The main protocols used at different layer of the protocol stack for terahertz band communications at the nanoscale.	23
1.6	Amplify-and-Forward and Decode-and-Forward relaying schemes. . .	25
2.1	The possible considered transmitter and receiver configurations. . . .	35
2.2	Absorption path loss as a function of frequency and transmission range, evaluated for the top-down configuration.	36
2.3	Spreading path loss as a function of frequency and transmission range, evaluated for the top-down configuration.	36
2.4	Total path loss as a function of frequency and transmission range. . .	37
2.5	Molecular absorption noise temperature as a function of frequency and transmission range.	40
2.6	Examples of pulses generated with the pulse-based communication scheme.	43
2.7	SNR obtained for the top-down configuration with flat transmission. .	45
2.8	SNR obtained for the top-down configuration with pulse-based transmission.	45
2.9	SNR obtained for the top-down configuration with optimal transmission.	46
2.10	SNR obtained for the bottom-up configuration with flat transmission. .	46
2.11	SNR obtained for the bottom-up configuration with pulse-based transmission.	47
2.12	SNR obtained for the bottom-up configuration with optimal transmission.	47
2.13	Channel capacity as a function of the transmission range, evaluated for the top-down configuration.	48
2.14	Channel capacity as a function of the transmission range, evaluated for the bottom-up configuration.	48
2.15	The reference scenario.	49

2.16	(a) Harvesting mechanism and (b) equivalent circuit modeling harvesting and discharging processes.	51
2.17	The investigated closed-loop control scheme.	52
2.18	Upper bound of the channel capacity.	55
2.19	Variation of the state variable, $V_c(t)$, in the time domain.	56
2.20	Variation of the consumed energy in the time domain.	57
2.21	Variation of (a) the state variable and (b) the consumed energy in the time domain during the transmission of a sequence of packets by considering three different acceptable values of g , $\lambda = 10^{-2}$ frames/s, $M = 40$ bit, and $d = 4$ mm.	59
3.1	The considered system model for transmission, propagation, and reception processes.	62
3.2	The considered transmission scheme.	64
3.3	The conceived continuous closed-loop control scheme.	66
3.4	Equilibrium point, V_∞ , as a function of the proportional gain, g , when (a) $C_n = 0.9$ nF and $h_n = 0.6$ pC, and (b) $C_n = 9$ nF and $h_n = 6$ pC. . . .	70
3.5	Modulus of the pole of the closed-loop control scheme, $ X $, as a function of the proportional gain, g , when (a) $C_n = 0.9$ nF and $h_n = 0.6$ pC, and (b) $C_n = 9$ nF and $h_n = 6$ pC.	71
3.6	Variation of the state variable, $V_c(t)$, in the time domain during the transmission of a long sequence of bits, by considering three different acceptable values of g , $C_n = 9$ nF, $h_n = 6$ pC, and $v_n = 0.42$ V.	72
3.7	The conceived closed-loop control scheme.	73
3.8	Minimum and maximum amount of energy required to transmit a frame.	85
3.9	Equilibrium point, V_∞ , as a function of the proportional gain g	86
3.10	The state variable, $V_c(k)$, as a function of the time when $N = 10$	87
3.11	The state variable, $V_c(k)$, as a function of the time when $N = 30$	88
3.12	The consumed energy as a function of the time when $N = 10$	89
3.13	The consumed energy as a function of the time when $N = 30$	90
3.14	The average BER as a function of the time when $N = 10$. The dotted line represents the target BER of 5%.	91
3.15	The average BER as a function of the time when $N = 30$. The dotted line represents the target BER of 5%.	92
3.16	The variance of the output, $\sigma_{V_c}^2$, as a function of the idle time, T_i	93
3.17	The average state variable as a function of the time when a perturbation of the inputs occurs.	94
4.1	The considered system model for transmission, propagation, and reception processes.	98
4.2	The considered transmission scheme with alternating ON and OFF periods with variable t_{OFF}	99

4.3	(a) Optimal threshold as a function of the communication distance d and the number of emitted molecules per bit m and (b) minimum required voltage as a function of the communication distance d , the frame size N , and the target BER \hat{P}_e	110
4.4	Analytical and simulation results for (a) the mean, (b) the variance for 0-bits, and (c) the variance for 1-bits of the noise at the output of the receiver as a function of the communication distance and the number of emitted molecules.	112
4.5	(a) Load current sequence, (b) voltage across the ultra-nanocapacitor, (c) number of packets in the queue, and (d) resulting consumed energy as a function of the time and the weight γ when a single realization is performed and with $N = 10$, $d = 30\mu\text{m}$, $\bar{t}_{OFF} = 100\text{s}$, and target BER = 5%.	113
4.6	Probability that the voltage across the ultra-nanocapacitor is lower than ϵ as a function of the communication distance d , the average off time \bar{t}_{OFF} , the target BER, and the frame size N	115
4.7	Number of packets in the queue as a function of the communication distance d , the average off time \bar{t}_{OFF} , the target BER, and the frame size N	116
4.8	Consumed energy as a function of the communication distance d , the average off time \bar{t}_{OFF} , the target BER, and the frame size N	118
4.9	BER as a function of the communication distance d , the average off time \bar{t}_{OFF} , the target BER, and the frame size N	119

List of Tables

1.1	Comparison of communication paradigms for nanonetworks.	8
1.2	Comparison between active and passive transport mode.	16
1.3	Comparison between Contributions Focusing on Micro and Nanoscale Scenarios	20
1.4	Classification of existing link layer protocols.	28
2.1	List of the main symbols used in this Section.	50
2.2	Summary of simulation parameters.	54
2.3	List of the minimum and maximum acceptable proportional gain val- ues.	55
3.1	List of the main analytical symbols.	63
3.2	List of Proportional Gain Values Used in the Performance Evaluation .	85
4.1	List of Main Symbols Used in This Chapter	100
4.2	List of Simulation Parameters	109

List of Acronyms

AWGN	Additive White Gaussian Noise
BER	Bit Error Rate
CNT	Carbon Nano-Tube
CSK	Concentration Shift Keying
CSMA/CA	Carrier Sense Multiple Access with Collision Avoidance
DMC	Diffusion-based Molecular Communication
FDTD	Finite-Difference Time-Domain
FTDMA	Frequency and Time Division Multiple Access
GNR	Graphene Nano-Ribbons
ICT	Information and Communications Technology
ICW	Inter-cellular Calcium Waves
IoNT	Internet of Nano-Things
IoT	Internet of Things
IRSK	Isomer-based Ratio Shift Keying
ISI	Inter-Symbol Interference
LDPC	Low Density Parity Check
LLC	Logical Link Control
MAC	Media Access Control
MAP	Maximum a posteriori Probability
ML	Maximum Likelihood
MoCo	Molecular Coding
MoSK	Molecular Shift Keying
NoC	Networks-on-Chip

OOK	On-Off Keying
PPM	Pulse Position Modulation
RTSK	Release Time Shift Keying
SNR	Signal to Noise Ratio
TDMA	Time Division Multiple Access
TS-OOK	Time Spread On-Off Keying
WNoC	Wireless NoC
ZnO	Zinc Oxide

Personal Scientific Contributions

The most significant scientific contributions generated during the PhD are listed in what follows. Those works have been accepted for publication in international journals and conferences or they are still waiting for revision.

Submitted Papers, waiting for revision:

- (S₁) V. Musa, G. Piro, L. A. Grieco, and G. Boggia, "Optimal and Energy-Harvesting Transmission Scheme for Diffusion-Based Molecular Communications", Submitted to IEEE Transactions on Wireless Communications.

International Journals:

- J₁) V. Musa, G. Piro, L. A. Grieco, and G. Boggia, "A Lean Control Theoretic Approach to Energy-Harvesting in Diffusion-Based Molecular Communications", IEEE Communications Letters, vol. 24, no. 5, pp. 981-985, 2020, doi: <https://doi.org/10.1109/LCOMM.2020.2972900>.
- J₂) V. Musa, G. Piro, L. A. Grieco, and G. Boggia, "A Feedback Control Strategy for Energy-Harvesting in Diffusion-Based Molecular Communication Systems", IEEE Transactions on Communications, vol. 69, no. 2, pp. 831-844, 2021, doi: <https://doi.org/10.1109/TCOMM.2020.3038796>.

International Conferences:

- C₁) V. Musa, G. Piro, L. A. Grieco, and G. Boggia, "Towards Long-Lasting Nanoscale Wireless Communications in the Terahertz Band for Biomedical Applications", Proc. of IEEE International Conference on Ad Hoc Networks and Wireless (AdHoc-Now), Bari, Italy, October, 2020
- C₂) F. Vista, V. Musa, G. Piro, L. A. Grieco, and G. Boggia, "Network Intelligence with Quantum Computing in 6G and B6G: Design Principles and Future Directions", Proc. of IEEE Workshops on Network Management For 6G Communication Systems (NETMAN6G), in conjunction with GLOBECOM 2021, Madrid, Spain, December, 2021

Chapter in International Edited Books:

- B₁) V. Musa, G. Piro, P. Bia, L. A. Grieco, D. Caratelli, L. Mescia, and G. Boggia, "Channel Modeling and Capacity Analysis for Nanoscale Communications and Networking", In Nanoscale Networking and Communications Handbook, pp. 101-125, CRC Press, 2019.

B_2) F. Vista, V. Musa, G. Piro, L. A. Grieco, and Gennaro Boggia, "Boosting Machine Learning Mechanisms in Wireless Mesh Networks Through Quantum Computing", In *Wireless Mesh Networks for IoT and Smart Cities: Technologies and Applications*, IET Press, 2021 (in press).

This PhD thesis describes the results reported in works S_1 , J_1 , J_2 , C_1 , and B_1 . The scientific contributions in C_2 and B_2 , instead, refer to research activities conducted during the last part of the PhD, focusing on topics not involved in the thesis.

Introduction

Nowadays, the innovation process triggered by nanotechnologies is boosting the development of integrated devices with size ranging from one to a few hundred of nanometers. These nano-devices are particularly interesting for Information and Communications Technology (ICT), biomedical, industrial and military applications, promoting the revolutionary evolution of the Internet of Things (IoT) paradigm towards the Internet of Nano-Things (IoNT). Given the restricted size of involved nano-antennas, the interaction among nano-devices, allowing the expansion of their capabilities, cannot be supported by traditional communication paradigms. Accordingly, the scientific literature proposed two innovative communication paradigms: electromagnetic communications, exploiting electromagnetic waves in the terahertz band due to the relationship between the wavelength and the wave frequency; molecular communications, encoding the information messages in specific properties of molecules.

In this context, nano-devices are required to transmit information without exceeding their available energy budget and preserving energy for successive communications (i.e., long-lasting communications). While the communication procedure (i.e., the generation, release, and reception of molecules or the transmission and reception of electromagnetic waves) cause a non-negligible amount of energy consumption, nano-devices can exploit a limited energy budget available within battery with restricted size. Accordingly, it is of paramount importance to conceive advanced techniques offering long-lasting communication capabilities at the nanoscale. On the one hand, nano-devices can operate as self-sustaining devices by retrieving energy from their surrounding. Though the scientific literature on harvesting-communication systems at the macroscale is significantly large and embraces many methodologies applicable to heterogeneous communication technologies and application domains, traditional approaches (e.g., those leveraging solar, wind, and thermal energy) seem to be inefficient at nanoscales. Here, it is preferable to use different energy harvesting models, based on mechanical and chemical sources, such as piezoelectric nanogenerators made up by Zinc Oxide (ZnO) nanowires which harvest energy from external vibrations (e.g., the human heart-beat in in-vivo applications). On the other hand, some interesting energy-aware communication mechanisms are proposed for nanoscale scenarios. With reference to molecular communications, the most promising solution is the molecule harvesting concept, according to which the energy cost due to the generation of molecules can be reduced by retrieving chemical material from the surrounding environment.

Considering terahertz band communications, instead, energy-aware transmission schemes usually manage the transmission time, the data dissemination, and the channel access. However, the information about the available energy budget has never been exploited for conceiving power control mechanisms in nanoscale wireless communication systems.

Under these premises, this thesis mostly investigates the joint integration of energy-harvesting mechanisms and energy-aware transmission schemes aiming at sustaining long-lasting wireless communications at the nanoscale. Here, the harvesting process is based on ZnO-based piezoelectric nanogenerators, while the discharging process strongly depends on the considered communication procedure. The resulting transmission power is properly tuned by simultaneously considering harvesting and discharging processes. A detailed description of the chapters constituting the thesis is provided in what follows.

Chapter 1 mainly discusses the many facets of the IoNT. Specifically, it gives an overview of the main existing transmission, propagation, and reception models for molecular communications and the most relevant protocols used at different layer of the protocol stack for terahertz band communications, evaluating pros and cons of every approach. For both the communication schemes, it also presents the fundamental applications in different domains (e.g., medical, industrial, and environmental) and the existing energy models, energy-aware transmission schemes, and energy-harvesting techniques, highlighting their main advantages and limitations.

Chapter 2 is mainly focused on energy-aware transmission strategies for terahertz band communications. Firstly, it investigates the physical transmission rates and the communication ranges reachable in the human tissues by modeling the communication channel as a non-homogeneous and dispersive stratified medium. This system model is, then, considered for properly conceiving a power control mechanism based on feedback control theory which dynamically tunes the instantaneous transmission power according to the available energy budget.

Chapter 3, instead, proposes a feedback control approach for dynamically adapting the transmission power (i.e., the number of emitted molecules) in a diffusion-based molecular communication scenario. In this case, the considered system model describes the transmission, propagation, reception, harvesting and discharging processes. The resulting control strategies are modeled with a continuous-time and a discrete-time nonlinear state equation, thus tuning the transmission power on a per-bit and on a per-frame basis, respectively.

Finally, Chapter 4 investigates an optimization problem for diffusion-based molecular communication system. To this end, it firstly proposes an analytical expression of the mean and variance of the noise at the output of the reception procedure in order to properly formulate the Bit Error Rate (BER). Then, it presents a novel optimization problem which selects the transmission power (i.e., the number of emitted molecules) on a per-frame basis minimizing the probability that the energy budget goes under a target value and the number of enqueued packets, while

satisfying energy and performance constraints.

The thesis closes with the Conclusions, summing up the main findings and drawing future research directions.

Chapter 1

Introduction to the Internet of Nano-Things

The innovation process triggered by nanotechnology is rapidly realizing the idea to deploy network architectures at the nanoscale, made up by integrated devices with size ranging from one to few hundred of nanometers. These devices are able to interact with each other, thus enabling new pioneering applications in ICT, biomedical, industrial, and military domains [1]. Accordingly, the time is ready to conceive innovative networking methodologies, protocols, and algorithms, which properly embrace the main facets of nanoscale communication systems, while fulfilling the requirements of enabled applications. However, at this embryonic stage of the research, any activity focusing on nanoscale networking should ground its roots to solid studies that carefully describe how the information is really exchanged between transmitter and receiver at the nanoscale. In particular, nano-devices can communicate by exploiting different communication paradigms like electromagnetic, acoustic, touch or molecular communications [2], which are briefly summarized in Table 1.1 and discussed in what follows:

- *Molecular Communication.* Molecular communication methods promise to enable data exchange among bio-inspired nano-devices [3]. Starting from numerous mechanisms already presented in nature, properties of biochemical particles are used to encode and transmit information messages. Released molecules, then, propagate through an aqueous medium according to a walkway-based (i.e., molecules follow a predefined path), a flow-based (i.e., molecules propagate in a guided fluid), or a diffusion-based (i.e., molecules freely diffuse in the medium) communication [4].
- *Electromagnetic Communication.* Electromagnetic communications exploit traditional electromagnetic waves as information carrier, by using its properties (such as amplitude, phase, and delay) to encode and decode the information messages. In this context, the terahertz band can be used as the operational frequency range for future electromagnetic nano-transceivers. This frequency band has been recently enabled by the emerging of new graphene-based materials, like Carbon Nano-Tube (CNT) and Graphene Nano-Ribbons (GNR) [5].

TABLE 1.1: Comparison of communication paradigms for nanonetworks.

	Electromagnetic communications	Molecular communications	Acoustic communications	Touch communications
Communication carrier	Electromagnetic waves	Molecules	Acoustic waves	Transient Microbot
Signal type	Electronic and optical	Chemical	Sound	Chemical
Propagation speed	Light	Extremely slow	Sound	Slow
Media	Space, cables	Aqueous	Fluid, solid	Aqueous
Range	Long distance	Short distance	Medium distance	Medium distance
Noise source	Electromagnetic fields and signals	Particles and molecules in medium	Interfering sounds	Particles and molecules in medium

Several studies already considered the biological effects of THz radiation on the human body [6], reporting no strong evidence of hazardous side effects.

- *Acoustic Communication.* Acoustic communication techniques produce slight pressure variations in the medium (fluid or solid), while satisfying the wave equation. The behavior of acoustic waves is represented by a complex number reporting both the amplitude and phase of waves. Acoustic communications have been evaluated for in-vivo ultrasonic communications (by examining their effectiveness, power requirements and effects on nearby tissue) [7] and opto-ultrasonic communications (by studying generation and propagation models and analyzing hazards and design challenges in wireless body area nanonetworks) [8], [9]. Features of acoustic communications make them particularly suitable for nano-device coordination over distances of around $100\mu\text{m}$ when frequencies between 10 MHz and 300 MHz are used [10].
- *Touch Communication.* Recent progresses in nanotechnology, bioresorbable radio frequency electronics, and engineered bacteria paved the way for the realization of transient microbot systems willing to accomplish tasks and, then, dissolve in the human body [11], [12]. Touch communication paradigms exploit swarm of transient microbots as information carriers, by controlling and tracking them through an external macro-unit [13]. Differently from the molecular communication, in touch communications the transmission and reception processes correspond to the loading and unloading of delivered drug particles [14]. Moreover, the adoption of active information carriers allows the communication over longer distances than the molecular communication paradigm.

Since the interest of the scientific community in the last years mainly focuses on molecular and electromagnetic communications [15], this thesis work will deeply discuss these two communication paradigms.

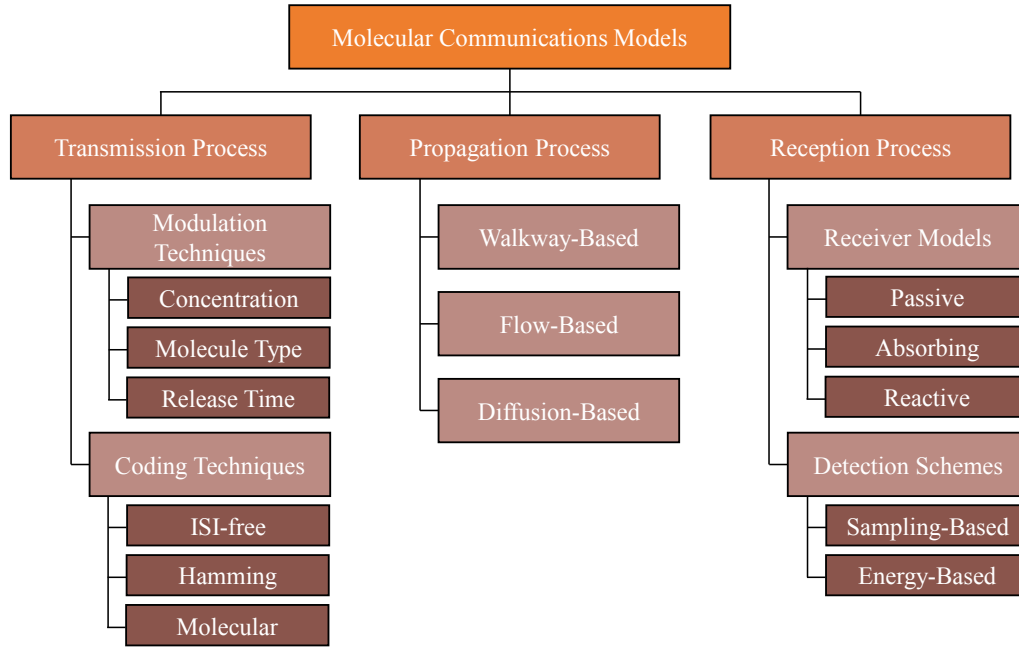


FIGURE 1.1: The main models used for transmission, propagation, and reception processes in molecular communications field.

1.1 Molecular Communications

The scientific literature on molecular communication systems significantly addresses the design and evaluation of transmission, propagation, and reception processes [16]. In what follows, it is firstly provided an overview of the main possible applications area enabled by this innovative communication paradigm. Then, the main communication models adopted by the scientific community for molecular communications are discussed, summarizing the main models used for transmission, propagation, and reception process (see Figure 1.1). Finally, this Section presents energy-harvesting and energy-aware solutions already proposed for molecular communication systems.

1.1.1 Applications of Molecular Communications

The development of molecular communications enables a wide area of innovative applications in different fields, such as medical, industrial, and environmental. Figure 1.2 summarizes the main enabled use cases which will be deeply discussed in what follows.

Medical Applications

Among the possible applications enabled by this new communication paradigm, the medical field in terms of diagnostic and treatment surely emerges as the most challenging and promising scenario due to the inherent bio-compatibility of molecular communications [3], [17], [18]. Specifically, there are many biomedical applications

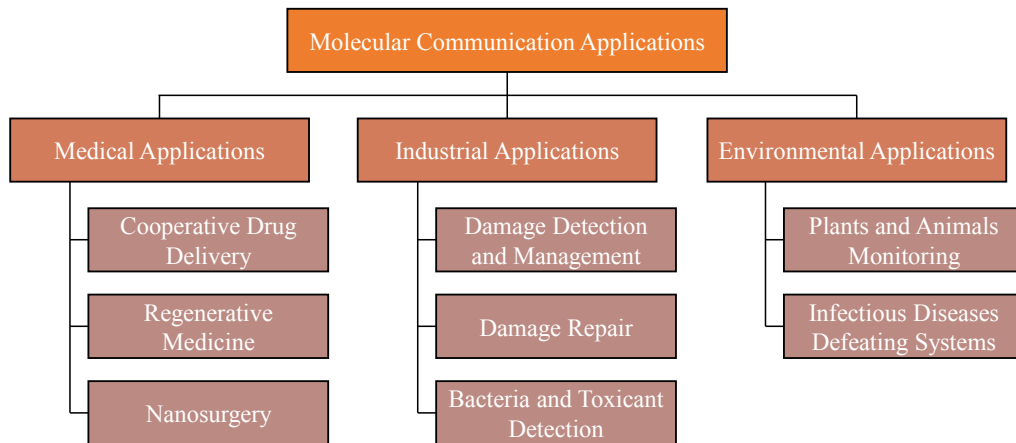


FIGURE 1.2: Main applications of molecular communications.

where nano-devices can sense the information but also make some actions when needed.

- *Cooperative Drug Delivery.* One of the most promising applications of molecular communications in nano-medicine is the drug delivery system [18]–[21], which aims at providing localized administration of drugs only where therapy is needed. This way, it is possible to maximize the therapeutic effect of drug molecules, also avoiding side effects on the healthy parts of the body. In fact, drug particles are encapsulated into small-sized natural [22], [23] or synthetic [24] drug carriers, which are injected nearby the infectious area and spread within the bloodstream or around the vascular vessels and interstitial barriers to reach the target location [25]. Around the target, nano-devices can coordinate their motion and control their spatial distribution in a self-organized manner by exploiting a novel molecular communication paradigm, known as mobile molecular communication. In this case, sender and receiver nano-devices assume a dynamic behavior, continuously changing their position during the communication procedure. A specific goal of this spatial control is to form a cluster of drug carriers around the target where embedded drug molecules are released [26].
- *Regenerative Medicine.* Another valuable application of molecular communications is the regenerative medicine [27]. Here, damaged tissues and organs are directly replaced by using recruited or transplanted cells. The main process exploited in this procedure is the cellular signaling which can be enabled by Diffusion-based Molecular Communications (DMCs) [25]. If successful, these technologies could provide alternative treatments for patients with organ and tissue disease. In fact, the involved molecules can control the response of cells and manage the formation of new tissues. Synthetic biology already demonstrated the applicability of molecular communication for regenerative medicine through pattern formation with *E. coli* bacteria [27], [28]. Also in

this case, the mobile molecular communication paradigm can be studied as a promising scheme to improve this application scenario [26].

- *Nanosurgery.* Molecular communications can be also used to enable a new branch of surgery, called nanosurgery, where coordinated nano-devices or nano-robots, with specific tasks and instruments, perform interventions directly into the patient's body [29]. The nanosurgery, supervised by human surgeons, can be exploited for intracellular surgeries reaching precision unachievable by traditional human manipulation [25]. Main conceivable interventions in this sense are: removal of microvascular obstructions; reconditioning of vascular endothelial cells; noninvasive tissue and organ transplantation; reparation of damaged extracellular and intracellular structures; and replacement of chromosomes inside human cells [30].

Industrial Applications

Though the medical field emerges as the most promising application scenario for molecular communications, they can be also applied in other complex medium, such as liquid or explosive gas environments [31]. In fact, there are lots of scenarios (e.g., explosive gas and underground) that are not suitable for manual operations (e.g., detection, management, and repairing). In this cases, nano-devices can overcome these weaknesses and enhance the operation efficiency. Accordingly, the following industrial applications can be considered as well for molecular communications:

- *Damage Detection and Management.* One of the potential applications in the industrial field is the detection and management of damage (e.g., corrosion) of pipes or devices. In fact, like in healthcare domain, nano-robots can be exploited for monitoring the concentration of specific bio-marks. Collected data can be, then, transmitted to a remote computer in order to predict the location of future corrosion in the pipe or device at the early stage [31], [32].
- *Damage Repair.* Nano-devices and nano-robots can be equipped with sensor and communication systems in order to remotely collaborate with high computational computers and detect damage in infrastructures. At the same time, they can exploit specific actuators and instruments to perform more complex tasks. For example, the high computational computer can remotely control nano-robots in order to carry out repair work, thus avoiding large-scale road-work [31].
- *Bacteria and Toxicant Detection.* The quality control procedure can also be considered as an industry application enabled by molecular communications. In this case, nano-devices can successfully detect small bacteria or toxicant substances in products distributed across the country (e.g., the water) or in the air, also when traditional sensors fail due to their high sensitivity [31]. It is important to note that the biocompatibility has a key role in the design of transmitter

and receiver nano-devices. Specifically, in the last years the scientific literature studied possible solutions for the ecological integration of nanodevices in the environment proposing novel biocompatible materials, such as polymers, soft organic electronics, dendrimers, and hydrogels [16].

Environmental Applications

The high sensibility of nano-devices can be also exploited for several environmental applications:

- *Plants and Animals Monitoring.* Nano-devices equipped with chemical nano-sensors can be used to detect or release chemical composites which are usually naturally released by the plants in the air in order to attract natural predators of dangerous insects or to regulate their blooming. Furthermore, molecular communications can be used to manage pheromones concentration in the air, thus controlling the behaviors of animals attract by them [31].
- *Infectious Diseases Defeating Systems.* Nano-networks with chemical nano-actuators can also release the same natural volatile substances able to attract natural predators of worms [33]. The release process can be triggered, for example, by a command center that interacts with microscale sensor devices.

1.1.2 The Transmission Process

With reference to the transmission process, the transmitter nano-device generally encodes information in a physical property of molecules (such as concentration, type, or release time). To this aim, information to be transmitted is firstly mapped to a sequence of bits through source and channel coding in order to 1) reduce the number of bits and 2) introduce additional bits to the information, thus providing error correction.

Modulation Techniques

Several modulation techniques have been already proposed for molecular communication systems, such as Concentration Shift Keying (CSK), On-Off Keying (OOK), Molecular Shift Keying (MoSK), Isomer-based Ratio Shift Keying (IRSK), Pulse Position Modulation (PPM) and Release Time Shift Keying (RTSK). They exploit the following properties of biochemical particles.

- *Concentration or Number of Molecules.* Binary information is encoded with the number or concentration of released molecules. The CSK mechanism, for instance, encodes the binary information through a variable number of emitted molecules: the transmitter releases Q_0 and Q_1 molecules for the bit 0 and the bit 1, respectively [34], [35]. A simpler implementation of the aforementioned CSK approach is the OOK scheme [36]–[38]. Here, only 1-bits are encoded

with burst of molecules, while no biochemical entities are released for 0-bits. These modulation schemes can be compared to the traditional amplitude shift keying, where the message is encoded in the amplitude of the electromagnetic waves.

- *Type of Particles.* The information can be also encoded through the type of the emitted molecules as in the MoSK modulation technique [35]. In this case, a molecule of the first type is used to transmit the bit 0, while a second type of molecule is emitted to encode the bit 1. The work in [39] proposes a particular implementation of the MoSK modulation scheme, namely IRSK, where the information is encoded in the ratio of isomers (i.e., molecules composed by the same number and type of atoms placed in different orientations). These schemes correspond to traditional frequency shift keying modulation techniques.
- *Release Time.* The PPM transmission scheme adopts the time of release to encode the binary information dividing the symbol duration in two slots: the instantaneous emission of molecules in the first slot corresponds to the transmission of the bit 0, otherwise the emission in the second slot is used to encode the bit 1 [40]. A more complex solution, namely RTSK, is studied in [41]. Here, the information is encoded by varying the amount of time between consecutive bursts of released molecules. The corresponding traditional modulation scheme is the phase shift keying.

Among the others, PPM and RTSK solutions are extremely complex because they require precise synchronization between transmitter and receiver. MoSK and IRSK, instead, are strongly limited by the number of molecules that can be selectively received. Accordingly, at the time of this writing, OOK is frequently considered by most of the scientific contributions due to its simple implementation in constrained communication systems available at the micro and nanoscale [16]. Figure 1.3 illustrates the main molecule properties that can be used for encoding a binary information, also comparing the proposed schemes with traditional modulation techniques.

Coding Techniques

Channel codes are used to mitigate the effect of noise introduced by the channel during molecules propagation (e.g., the Inter-Symbol Interference (ISI) effect due to previously transmitted symbols). Usually, they insert redundancy bits useful for detecting and/or correcting decoding errors. Given the limited amount of energy of nano-devices, energy efficiency of employed channel codes represents an important aspect to be taken into account during the design of coding techniques. Accordingly, the scientific literature proposed several simple parity codes or cyclic codes for molecular communication systems [16], instead of more advanced and computational complex codes developed for traditional communication systems, such as

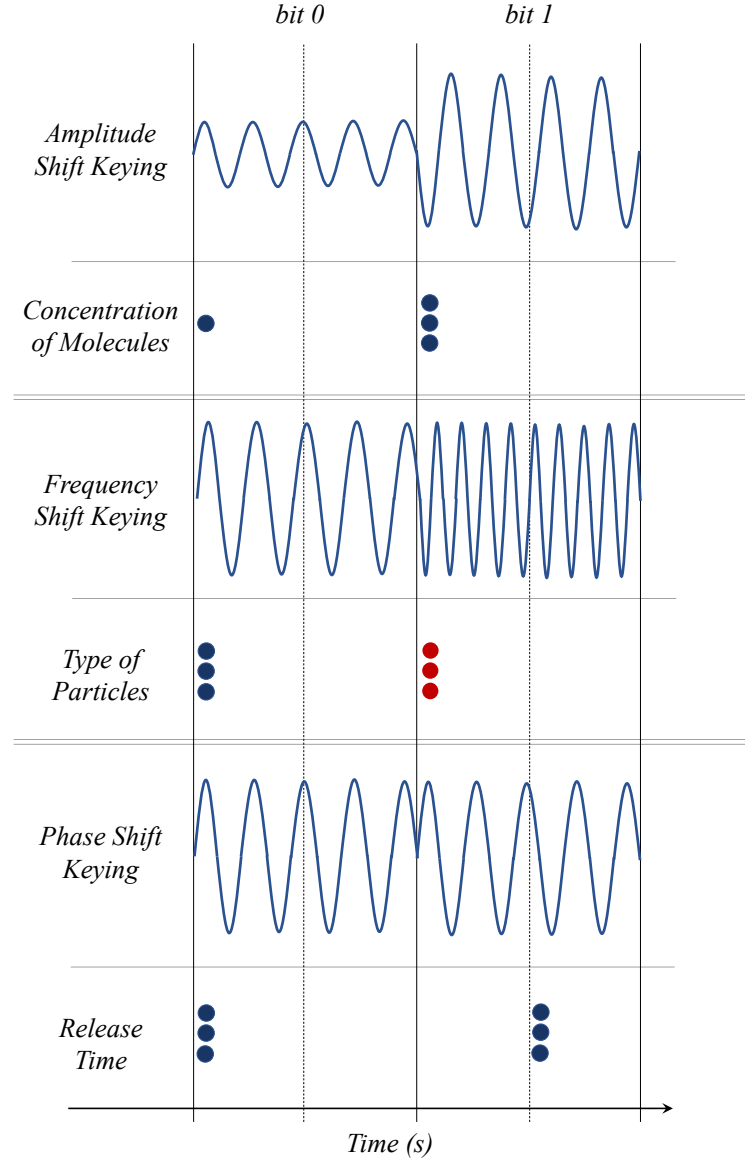


FIGURE 1.3: Possible modulation techniques.

Turbo codes [42] or Low Density Parity Check (LDPC) codes [43]. The main coding techniques studied and evaluated for molecular communications are listed below.

- *ISI-Free Coding*. ISI-free coding schemes aims at avoiding the problems related to ISI effects by simply adding a number of bits to the original frame. Specifically, the encoding scheme is denoted by three parameters, that is n , k , and l . The parameter n represents the number of bits sent for each k bit of information, while l is the number of maximum delay time-slots that molecules can have without causing interference. For instance, the ISI-free coding scheme proposed in [44] is an ISI-free (4,2,1), where respectively $n = 4$, $k = 2$ and $l = 1$. Consequently, this code guarantees the elimination of errors due to the molecules arriving only in the successive time-slot.

- *Hamming Code*. The Hamming code is a coding technique, belonging to linear block codes, usually identified by two parameters (n, k) , where n is the number of bits sent for each k bit of information. In this context, $M = n - k$ represents the number of parity bits introduced, while the length of the message encoded using the Hamming technique given a frame of N bits is equal to $L = Nn/k$. The possible number of combinations identifying a message in the Hamming code (n, k) and composing its dictionary is 2^k . In this context, a key parameter is the minimum distance of the code, defined as the minimum number of bits that differ between two words belonging to the same dictionary of the Hamming code (n, k) . Starting from the minimum distance, in fact, it is possible to derive the number of recognizable errors and the number of correctable errors by the coding technique. The adoption of Hamming codes for molecular communications is particularly suitable only for larger distances, while they are energy inefficient at small communication distances due to the energy required to transmit the extra parity bits [45]. To partially solve this problem, the scientific community studies a Hamming Minimum Energy Code (MEC), which maintains the desired code distance to keep reliability while also minimizing the energy consumption [46].
- *Molecular Coding (MoCo)*. Differently from aforementioned schemes which are obtained by extending existing coding techniques, few works developed novel coding schemes properly tailored for molecular communication systems, such as the MoCo technique [47]. In this case, the Hamming distance metric is replaced by the MoCo distance function: it is defined by computing the transition probability (i.e., the probability to receive the codeword x instead of the codeword y). Accordingly, the MoCo code construction aims at finding the codewords that maximize the minimum pairwise MoCo distance. Note that the MoCo distance is not symmetric and, in turns, it can not be defined as a metric. Specifically, [47] demonstrated that the $(4,2)$ block code generated with MoCo outperforms the equivalent Hamming code in terms of error rate. However, the generation of MoCo codes strictly depends on the channel properties and variations. Accordingly, it requires significant computational resource at the transmitter side and brings to a non-negligible overhead communication due to the code synchronization procedure [16].

1.1.3 The Propagation Process

Emitted molecules propagate in the aqueous medium to reach the receiver sphere by following a passive or an active propagation mode [19]. Passive mode concerns molecules that randomly diffuse in all the available directions, while active mode refers to particles that directionally propagate to specific locations. Commonly, active mode allows information to reach far nodes, requiring, however, energy supply and communication infrastructures. Typical examples of active transport mode are

TABLE 1.2: Comparison between active and passive transport mode.

Propagation Mode	Active Mode	Passive Mode
Molecules Propagation	Directional	Random
Range	Long Distance	Short Distance
Number of Required Molecules	Small	High
Communication Infrastructure	Required	Not Required
Energy Supply	Required	Not Required
Average Transmission Delay	Low	High and Highly Dynamic

the walkway-based propagation and the flow-based propagation. Passive mode, instead, is particularly suitable when a molecular communication infrastructure is not available and the amount of energy is strongly limited (i.e., it does not require energy supply). However, with passive mode emitted particles randomly diffuse in the medium, thus requiring a large number of molecules to reach quite far destinations [48]. The most widespread passive transport method for molecular communications is the diffusion-based propagation scheme. Table 1.2 summarizes the main differences between active and passive transport mode.

Walkway-Based Propagation

In the walkway-based architectures, molecules connect transmitter and receiver through pre-defined pathways by using carrier substances, such as molecular motors [49], [50]. A molecular motor is a protein or protein complex that transforms chemical energy (e.g., ATP hydrolysis) to change the position or structure of the molecular motor. In this model, the information molecules are bind to the molecular motor which, using chemical energy, guides molecules to the receiver [51]. Alternatively, information molecules can be transported by bacterial motors [52]: according to chemical concentrations in the surrounding environment, bacteria move directionally and exchange information through the conjunction process [53]. Typically, walkway-based communications allow information molecules to be transported over longer distance than the traditional diffusion-based communications. Furthermore, they provide a communication mechanism with a very high reliability even when the number of information molecules is small. On the other hand, this architecture requires high level of chemical energy to be consumed and complex communication infrastructures [49].

Flow-Based Propagation

In the flow-based architectures, molecules diffuse in the aqueous medium by following guided and predictable flows [49]. Specifically, nano-devices can exploit existing flows in biological systems. In this case, since biological systems naturally operate at the nanoscale, it is simpler to guarantee the bio-compatibility of the communication process. An example of this propagation paradigm is the hormonal communication through the blood streams inside the human body. The flow-based propagation

can also be realized by using carrier entities whose motion can be constrained along specific paths. In this case, information molecules pass through existing gap junctions, inspired from inter-cellular communication in nature. For instance, one type of cell-cell communication, widely used by multi-cellular organisms, is the calcium signaling [54]. Here, the information is encoded through changes in the concentration of calcium ions (Ca^{2+}). The increased Ca^{2+} concentration propagates cell to cell using gap junctions that directly connect the interior of one cell and that of another. This mechanism allows coordinated actions between adjacent cells. Specifically, the system is composed of a transmitting pair (i.e., source and destination devices) and an Inter-cellular Calcium Waves (ICW)-capable intermediary cells [55]. The transmitter nano-device encodes the information with an ICW stimulating the closest intermediary cell. Then, the calcium signal propagates through the intermediary and adjacent cells through existing gap-junctions until the destination device is reached [56]. Calcium signaling allows to interconnect adjacent cells with a high communication speed and long operational range in a bio-compatible manner. However, it is feasible only when a pre-defined path or flow exists between the transmitter and receiver nano-device.

Diffusion-Based Propagation

DMC is one of the fundamental communication mechanisms used by biological systems. It is based on passive transport mode: here, molecules released by the transmitter passively propagate via random motion, namely Brownian motion. Differently from other approaches based on walkway-based and flow-based transport mechanisms, DMC allows molecules to randomly diffuse in all the available directions, instead of moving alongside specific paths [57], [58]. Therefore, though DMC systems require a large number of molecules to reach far destinations, they are particularly suitable when the available energy is low and/or biological communication infrastructures (i.e., gap junctions or molecular motors) are not available [4]. An example of DMC system in nature is quorum sensing, that is a communication mechanism for bacterial cells. In quorum sensing, bacterial cells release and detect an autoinducer into the environment in order to estimate the number of nearby bacteria [53]. When the estimated concentration of bacteria in the environment is sufficiently high, the bacteria start transcribing DNA to perform group functions (e.g., generate luminescence) [59].

1.1.4 The Reception Process

Molecules reaching the destination nano-devices are, finally, received and detected by the receiver. It is usually described as a spherical device which captures propagating molecules in different ways. Specifically, Figure 1.4 depicts the main receiver

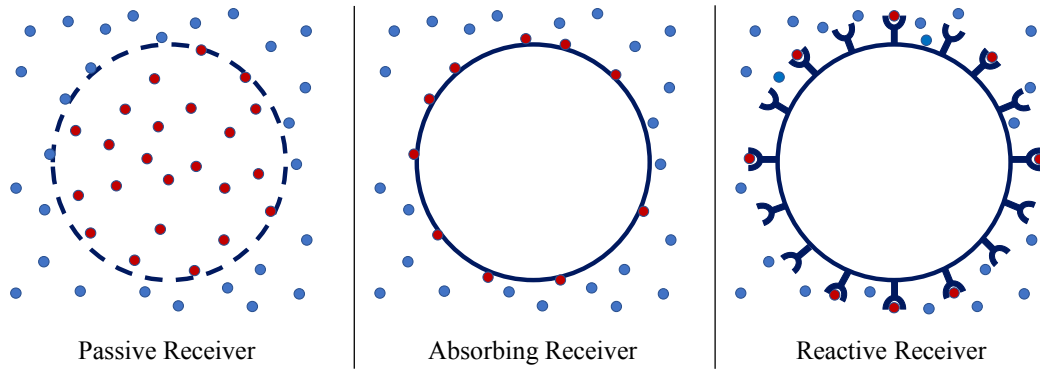


FIGURE 1.4: Three main receiver models.

models studied by the scientific community, known as passive, absorbing, or reactive receiver. Finally, received molecules are converted in a binary signal according to one of the detection techniques described in the following.

Receiver Models

The receiver is usually described as a spherical device which captures propagating molecules in different ways (see Figure 1.4):

- *Passive Receiver.* Most of the current scientific literature, like [60]–[63], models the receiver sphere as an ideal device, namely passive receiver. In this case, the receiver simply counts the number of molecules reaching the destination volume, while ignoring the impact of biochemical reactions implemented at the receiver side. Though this scheme allows to guarantee the simplicity of the considered system model by only focusing on the transport of molecular messages to the receiver location, its physical correspondence is highly doubtful [16].
- *Absorbing Receiver.* The works discussed in [64]–[67] introduce a more complex receiver model, namely absorbing receiver. Here, the receiver surface is supposed to be completely covered by hypothetical receptors. Any molecule that hits the surface of the nano-device at the destination side can be absorbed and degraded by the receptors. Then, the received molecules are removed by the medium and do not interfere with successive transmissions. Even if the physical correspondence of this model with actual molecules receivers is questionable, it is widely adopted by the scientific community due to the obtained upper performance limits [16]. However, ignoring the ligand-receptor reactions, which often leads to further model complexities, stands as a major drawback of these two approaches.

- *Reactive Receiver.* Another modeling approach, discussed in [37], [68]–[70], takes into account a more realistic reception process, based on the ligand-receptor mechanism. Here, the transmitted molecules (i.e., ligands) can reversibly react with a limited number of proteins placed on the receiver surface (i.e., receptors). The resulting reception mechanism is modeled through a second-order reversible reaction and provides a satisfactory representation of what happens in nature, with the possibility to extract punctual information related to the actual sampling time instants.

Though the ligand-receptor model is more realistic than the others approaches, most of the scientific contributions still consider the passive or the absorbing receiver in their system models due to their simplicity [16].

Detection Techniques

Besides the reception process, several detection methods can be used to evaluate the received signal. All these available approaches can be divided in two main categories, namely sampling-based and energy-based detection schemes [71]:

- *Sampling-Based Detection Scheme.* The sampling-based approach, described in [37], [72]–[75], considers the instantaneous number of molecules received by the destination nano-device. The work in [37] employs a Maximum Likelihood (ML) detection method for a ligand-receptor receiver. The receptor occupation ratio is used as a measure of the received signal, tackling also the problem of the receptor saturation. At the same time, by taking into account a ligand-receptor receiver, the number of received molecules in a time slot can be computed as the difference between the number of bounds at the end and the one at the beginning of the symbol duration [72]. The obtained number of molecules can be, then, compared with a fixed threshold to evaluate the received bit. In [73], a M-ary CSK-based system is formulated by considering an optimum receiver, where the Maximum a posteriori Probability (MAP) and ML detectors are taken into account as possible approaches. Similarly, the work in [74] considers a sequence detection approach based on the MAP and ML criteria. Here, a sub-optimal linear equalizer (i.e., Minimum Mean-Square Error) and a decision-feedback equalizer are proposed to reduce the complexity and improve the performance of the system, respectively. Sampling-based detection without any knowledge of the system model and channel conditions can be also performed by exploiting the potential of artificial neural network methods in the presence of ISI [75].
- *Energy-Based Detection Scheme.* The energy-based detection, investigated in [76]–[78], computes the total amount of molecules absorbed by the receiver during a given time interval, usually equal to the symbol duration. The paper

TABLE 1.3: Comparison between Contributions Focusing on Micro and Nanoscale Scenarios

Contributions	Communication Scenarios			Energy Harvesting			Total Energy Consumption	Energy-Aware
	Neural	Terahertz	DMC	Molecule Harvesting	Chemical	Piezoelectric		
[39], [45], [79] [80], [81]			✓				✓	
[82]–[84]					✓			
[85]–[93]						✓		
[94]–[98]		✓				✓	✓	✓
[99], [100]	✓					✓	✓	✓
[101]–[105]			✓	✓				✓

in [76] describes a strength-based signal detector, where the receiver accumulates molecules during the entire symbol duration, produces a test statistic and compares the computed strength to a fixed threshold. On the contrary, the works in [77], [78] propose an adaptive-threshold detection approach where the value of the threshold is computed in each time slot depending on the previous received bits, considering a variable memory length and the only ISI as noise contribution.

Among the available detector schemes, most of the current scientific literature used the amplitude-based one during the system modeling [16].

1.1.5 Energy-Aware Molecular Communications and Energy-Harvesting Schemes

At micro and nanoscale, devices can perform simple tasks by leveraging a limited amount of energy due to restricted battery size [4]. Therefore, given that the local generation and release of molecules (i.e., hormones, pheromones, proteins, DNA, and RNA) cause a non-negligible amount of energy consumption, the energy issue is a key aspect that should be taken into account during the design of DMC systems [16]. Table 1.3 summarizes the existing works focusing on the energy issue at the micro and nanoscale, which are deeply discussed in what follows.

Energy Models for Diffusion-based Molecular Communications

Models able to quantify the amount of energy consumed during the transmission process in DMCs have been already provided by the scientific literature. As a starting point, the energy required to synthesize, carry and emit information molecules at the transmitter side can be evaluated by considering the basic eukaryotic cells as perfect models for bio-inspired nanodevices [39], [79]. Unlike the active transmission (i.e., molecular motors), DMCs do not demand any additional external energy for delivering the information molecules [80]. Moreover, besides the modulation process, the transmitter can encode and decode binary information to improve the performance of the communication system. In this case, the transmitter needs a further amount of energy to generate and emit parity check bits [45], [81]. However,

given the limited battery size of these nanodevices, the developing of advanced techniques able to guarantee long-lasting communication capabilities at both micro and nanoscales is of paramount importance.

Energy-Harvesting Techniques at the Nanoscale

Nowadays, the scientific literature on energy harvesting methodologies at macro-scale is flourishing and envisages the possibility to retrieve electrical energy from different sources to supply communicating nodes. Accordingly, many types of energy harvesting schemes have been considered, like solar, thermal, piezoelectric, wind, and hydroelectric [106]–[109]. Nevertheless, the amount of harvested energy is strictly correlated with the application case and the time spent for the harvesting process. Then, while traditional mechanisms (e.g., solar, thermal, and wind energy harvesting methods) are inefficient in micro and nanoscale scenarios, other energy harvesting models have been successfully introduced in this field, including mechanical and chemical sources [110]–[112]. The chemical and biochemical energies, evaluated in [82]–[84], can be harvested by enzymatic fuel cells (i.e., biofuel cells), where enzymes are used as cathode, anode, or both, instead of traditional metals to make this technology compliant with the micro and nanoscale constraints. The biofuel (e.g., glucose, hydrogen or methanol) is oxidized at the anode side releasing electrons which are driven through an electrical circuit toward the cathode side. Accordingly, the chemical energy of the biofuel is converted into electrical one. At the same time, the amount of energy required by the nanodevices can be also harvested by mechanical sources (e.g., from vibrations or motions). In this context, piezoelectric nanogenerators composed by lead zirconate titanate (PZT) [92], [93] or ZnO [85]–[91] nanowires are the most promising energy harvesting techniques at the micro and nanoscale. Here, the vibrations or motions existing in the surrounding environment bent or compress the nanowires generating an electric current at their ends which charges an ultra-nanocapacitor [113], [114]. The sources compressing the nanowires can have a wide range of frequencies depending on the considered application scenario (i.e., 1 Hz for the human heartbeat) [87].

Some contributions already envisaged the adoption of piezoelectric nanogenerators to feed nanodevices willing to communicate through electromagnetic waves in wireless nano-sensors networks at the Terahertz band [94]–[98] or to selectively stimulate peripheral nerves in the human body through light signals [99], [100].

Regarding the DMC scenario, preliminary attempts in this direction have been investigated in [101]–[105]. The work in [101] presents DIRECT, a networking model where the system resources are considered as discrete elements (i.e., molecules). Differently from the electromagnetic case, molecules diffuse in the medium without physical attenuation and, consequently, they can be completely reused. Based on this premise, the work [102] introduces the molecule harvesting concept, according to which the energy cost due to the generation of molecules can be reduced by retrieving chemical material from the surrounding environment. The received

molecules can be stored in a reservoir in order to be reused during subsequent transmission processes. The work [103] considers the capacity degradation due to the limited molecule production at the transmitter side. Here, the state of the transmitter (i.e., the number of molecules available in the reservoir) is updated according to the number of released and captured molecules in the previous time slot. An additional energy saving can be achieved by exploiting relay nodes, as described in [104] and [105]. In these works, a simultaneous molecular information and energy transfer (SMIET) system is presented, reducing the synthesis cost by recovering the information molecules from the environment and adopting a two-hop molecular communication system. Unfortunately, none of the works presented in [101]–[105] consider all the energy needs related to the communication process and the actual energy budget available within nano-devices, as explicitly highlighted in [105].

1.2 Terahertz-Band Communications at the Nanoscale

The interaction among nano-devices can be also enabled by nanoscale wireless communications in the terahertz band [115]. In the last years, in fact, the introduction of graphene-based nanoantennas generating electromagnetic waves in the terahertz band (i.e., from 0.1 to 10 THz) made the communication feasible at the nanoscale and in human tissues [116]. For this reason, the scientific community is nowadays targeting terahertz band communications providing several studies on the different layers of the protocol stack [117], as well as the possible channel models, the energy-harvesting solutions, and the possible enabled application areas [118].

Fig. 1.5 summarizes the main protocols used at the network, link, and physical layer in terahertz band communications at the nanoscale which will be deeply discussed in what follows.

1.2.1 Applications of Terahertz-Band Communications at the Nanoscale

Terahertz band communications at the nanoscale enable a plethora of novel application domains. Among the others, this Section considers the most promising fields categorized as software-defined metamaterials, wireless robotic materials, in-body communications, and on-chip communications [117].

Software-Defined Metamaterials

The propagation of electromagnetic waves, especially in high frequency scenarios, strongly suffers from absorption losses due to obstacles in the communication medium. To overcome these issues, the scientific literature is focusing on the development of manufactured structures able to control the behavior of electromagnetic waves, i.e., metamaterials and metasurfaces [119]. These outstanding materials are composed of periodic array of subwavelength elements, called unit cells,

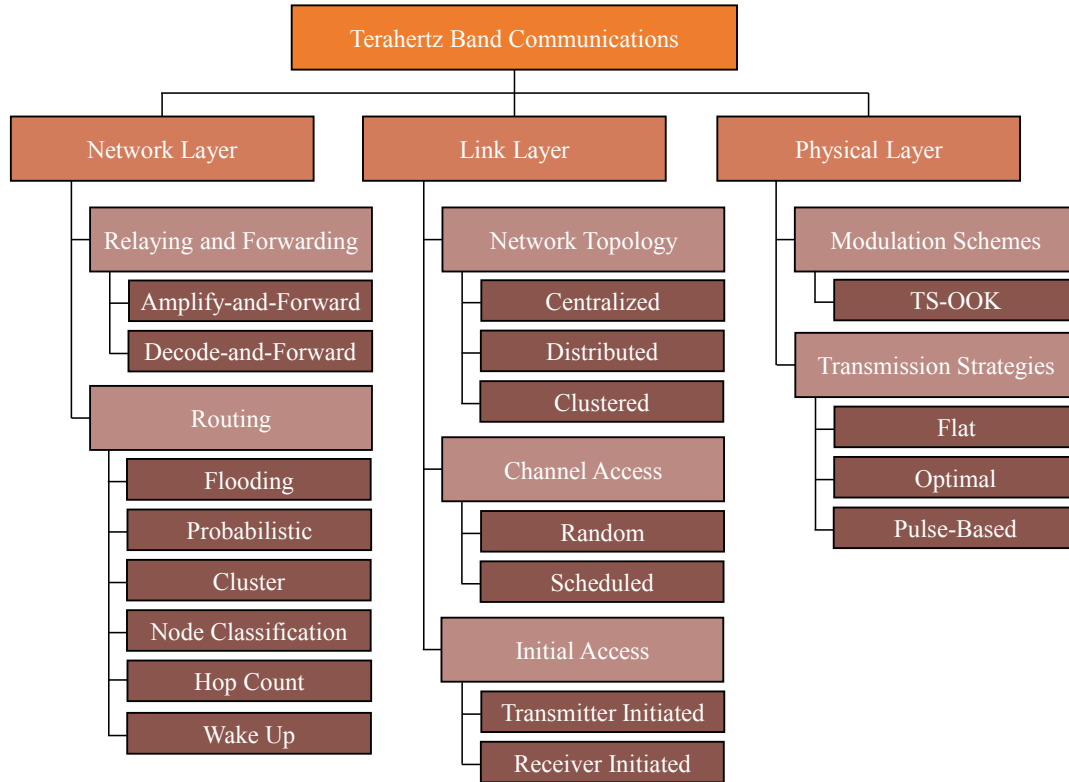


FIGURE 1.5: The main protocols used at different layer of the protocol stack for terahertz band communications at the nanoscale.

which can be dynamically reconfigured in order to realize programmable metamaterials (i.e., software-defined metamaterials) [120]. Software-defined metamaterials are largely adopted in wireless communications for realizing intelligent reflecting surfaces [121], developing simplified architectures [122], or supporting holographic imaging [123]. The reprogramming is managed by communication network of controllers where each controller handles associated unit cells. Given the limited dimensions of controllers, terahertz band communications appears as a promising paradigm to support the interaction between controllers and associated unit cells [124].

Wireless Robotic Materials

Differently from software-defined metamaterials, wireless robotic materials are expected to support innovative multi-functional and programmable composites able to dynamically adapt their physical properties based on information collected from the surrounding environment [125]. Specifically, wireless robotic materials are suggested for realizing airfoils tuning their aerodynamic profile, vehicles able to camouflage themselves, bridges which detect and repair damage, robotic skins and prosthetics with a realistic sense of touch [125], tactile sensing skin, and nanodevices reproducing patterns for camouflage [126]. In this context, the network is expected to completely cover the object (e.g., the vehicle or the human body) in a dense way.

Accordingly, terahertz band communications emerges as a promising paradigm for the communication of size-limited elements of robotic materials [126].

In-Body Communications

The most promising application scenarios for nano-devices is, without any doubt, the biomedical field. In fact, nano-devices can be implanted, ingested, or worn by humans in order to realize drug-delivering and advanced immune systems, biohybrid implant solutions, pervasive health monitoring, and genetic engineering [2]. Usually, these mobile nano-devices are able to reach small regions of the human body in a bio-compatible way in order to perform sensing (e.g., early detection of malicious agents such as viruses, bacteria, or cancer cells) and actuation (e.g., release specific treatments according to the targeted drug delivery mechanism) operations [17]. Given the size limitations and the high expected number of involved medical nano-devices, the communication among them and with outside-world controllers is enabled by terahertz band communications [117].

On-Chip Communications

In the last decade, processors performance has been enhanced by means of more cores integrated within the same chip. To provide interconnection on the same chip, the scientific literature widely studied the so-called Networks-on-Chips (NoCs) scheme by considering initially wired connections and, then, Wireless NoC (WNoC) in order to avoid undesired delays, power requirements, and area overhead [127]. In fact, WNoCs allows to reduce the propagation delay, enhance the reconfigurability, and improve the scalability in terms of delay, throughput, and energy consumption [128]. Furthermore, nanoscale WNoCs have been recently proposed by exploiting graphene-based nano-antennas. In this context, the inter-core communication is enabled by electromagnetic waves in the terahertz band [117], [129].

1.2.2 The Network Layer

The definition of routing and forwarding protocols is essential for achieving the communication between nodes belonging to the same nano-network [130]. However, given the limited capabilities of nano-devices in terms of memory, channel, and energy, traditional routing and forwarding protocols cannot be applied to nano-networks, thus needing for simple, scalable, and optimized protocols [131].

Relaying and Forwarding Protocols

In nano-networks, each node or only a subset of them should be equipped with relaying and forwarding functionalities in order to successful transmit packets between no-adjacent nodes. Specifically, the main relaying and forwarding schemes deployed for terahertz-band communications at the nanoscale are discussed below.

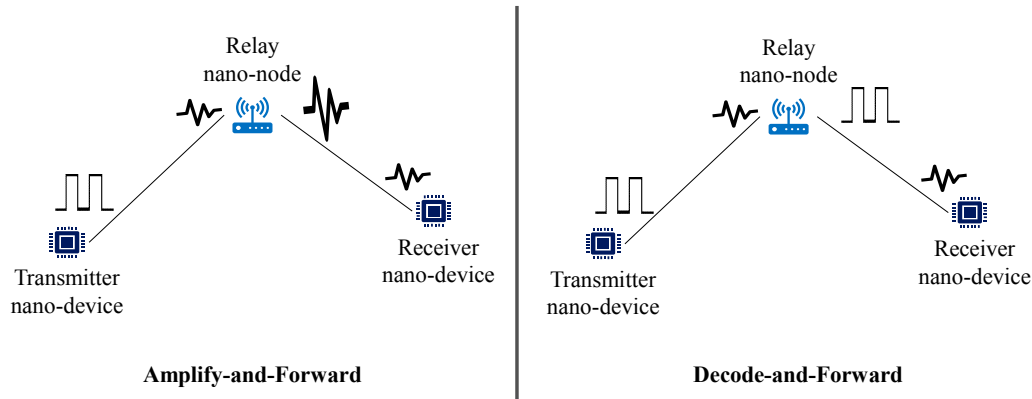


FIGURE 1.6: Amplify-and-Forward and Decode-and-Forward relaying schemes.

- *Amplify-and-Forward.* Amplify-and-Forward is a simple cooperative strategy for ad-hoc networks with critical power constraints, thus resulting as an optimal solution for terahertz band communications at the nanoscale. Specifically, it involves non-regenerative repeater which simply amplifies the received signal in the analogue domain at the relays without further signal processing. Accordingly, relay nodes has only to simply amplify the received signal before re-transmitting it [132].
- *Decode-and-Forward.* Decode-and-Forward schemes are rooted in the communication principle of regenerative repeaters. In this case, the relay node must perform a more complex operation by decoding (demodulating) the signal received from the source node before forwarding the encoded (modulated) signal to the destination nano-device. Though this strategy requires more effort from the transmitter nano-device, the noise effect due to the propagation in the channel is strongly reduced, thus further improving the communication performance in terms of Signal to Noise Ratio (SNR) [132].

Figure 1.6 depicts the amplify-and-forward and decode-and-forward relaying schemes.

Routing Protocols

The scientific community widely explored innovative routing protocols completely feasible with energy, memory, and computational constrained scenarios. Specifically, the main routing protocols proposed for terahertz-band communications are summarized in what follows.

- *Flooding-Based Routing Scheme.* The flooding-based routing scheme is the most straightforward communication protocol. Here, the received packet is unconditionally retransmitted to all the involved nodes in the nano-network without any constraint [131]. Though this strategy is advantageous due to its simplicity, reliability through redundant transmissions, and lack of topology-dependent

initialization, it is highly inefficient because unmodified flooding involves a high number of redundant transmissions [117]. However, reducing the number of packet retransmissions and providing efficient networking and application services is still an open issue. To provide an initial solution to this problem, some works proposed an adaptive flooding scheme where wireless nano-nodes can deactivate themselves based on some performance levels (e.g., signal to interference ratio, number of available resources) [133], [134].

- *Probabilistic-Based Routing Scheme.* To preserve the communication efficiency, some works propose probabilistic-based routing strategies to forward incoming packets in 2D [135] or 3D topologies [136], [137]. The probabilistic routing scheme can consider the energy harvesting process of nano-devices [135], [136] or not [137]. Furthermore, the suggested routing protocol can be either single hop or multi-hop [135]. In each hop, the nano-sensor itself or a nano-controller takes a forwarding decision based on a probability value which can be computed considering energy savings through multi-hop transmission [135], [136] or generating a random value to be compared with a fixed threshold [137]. Though this approach avoids the high number of redundant transmission highlighted in the flooding scheme, it has a complexity which drastically increases with the number of hops. Furthermore, the computation of periodic forward probability increases the processing overhead [131].
- *Cluster-Based Routing Scheme.* As a means of reducing the complexity at the nano-controller and the computation overhead at each nano-sensor, the scientific community proposes a novel solution, known as cluster-based routing scheme [131]. In this case, all the collected data is sent to a nano-controller which manages the forwarding behavior of the whole cluster. The cluster is composed of a cluster coordinator, cluster members, and cooperative relays [138], [139]. Specifically, each nano-node verifies the amount of available energy and, accordingly, participate or not in forming the cluster. Periodically, it is defined the coordinator choosing among all the nano-nodes constituting the cluster. Some works, like [140], [141], introduce an energy model to the routing process by joining the energy harvesting and consumption. Other works also consider a dynamic scenario where mobile nano-nodes periodically select the appropriate nano-controller when they have data to send [142]. This decision is based on the distance from the nano-controller, the residual energy, and the traffic load of the nano-controller. However, the cluster-based routing schemes present some main weaknesses: 1) since all the collected data is transmitted to a single nano-controller, the energy of this nano-controller will expire quickly; 2) the computation complexity at each nano-sensor can be excessive; 3) the overhead generated by cluster creation strongly increases when nano-sensors move [131].

- *Node Classification-Based Routing Scheme.* With the aim of improving communication performance and decreasing the number of packet re-transmissions, many works of the state of the art propose to limit the number of forwarding nano-sensors. Specifically, they conceived a new routing protocol, named node classification-based routing scheme, where each nano-node classifies itself as a retransmitter (i.e., the node forwards incoming packets) or a simple user node (i.e., the node only receives packets without any re-transmission) [133], [134], [143]. The self-classification can be performed by each nano-node based on its signal to interference ratio level [133], the local packet reception statistics [134], or past statistics of packet reception [143]. Though this scheme reduces the number of re-transmitted packets, there is no defined path for the data packet. Accordingly, each retransmitter node receiving a packets blindly forwards it, thus generating high level of broadcast exchange packets overhead [131].
- *Hop Count-Based Routing Scheme.* Data packets can also be re-transmitted based on the number of hops between transmitter and receiver nano-devices. Usually, it can be done by following two phases: the first one, named setup or addressing phase, is used to retrieve the number of hops between each node and four anchor nodes; the second one, named operation phase, distributes the packets across the shortest path [144]. The same routing scheme is used also for 3D scenarios [145], [146] and over curvilinear paths [147]. Though the proposed schemes allow reducing the number of hops during the communication procedure, they do not apply sleeping techniques and do not consider any energy harvesting scheme or energy consumption model. Furthermore, they still suffer from high computation and memory overheads [131].
- *Wake Up-Based Routing Scheme.* The energy of nano-devices can be preserved by posing them in a sleep state in appropriate time instant. Exploiting this ability of nano-devices to change their state from active to sleep, the scientific community proposed an innovative routing scheme, called wake up-based routing scheme. Here, a central rotating entity can be used to periodically select a nano-device and change its state [131]. Other works also consider an energy-harvesting scheme based on a piezoelectric system [148], [149]. In this case, when a data packet must be sent, a nano-controller transmit a broadcast activation message and select the nano-sensors in its activation area to be activated based on the current amount of available energy. To avoid high delays and waste of energy due to activated and not selected nano-sensors, nano-devices can be gradually activated only if their energy is within a given range of values [150].

TABLE 1.4: Classification of existing link layer protocols.

Contributions	Network Topology	Channel Access	Initial Access
[154]	Centralized	-	Transmitter Initiated
[155], [156]	Centralized	Scheduled (TDMA)	Transmitter Initiated
[157]	Centralized	Random (CSMA)	Transmitter Initiated
[158]	Centralized	-	Receiver Initiated
[159]	Distributed	Random (CSMA)	Transmitter Initiated
[152], [160]–[162]	Distributed	Scheduled (TDMA)	Transmitter Initiated
[163]–[165]	Distributed	Scheduled (TDMA)	Receiver Initiated
[142], [166], [167]	Clustered	Scheduled (TDMA)	Transmitter Initiated
[168], [169]	Distributed	Random	Transmitter Initiated
[170]	Clustered	Scheduled (FTDMA)	Transmitter Initiated
[171]	Distributed	Scheduled (FTDMA)	Transmitter Initiated
[134]	Distributed	-	Transmitter Initiated
[172]	Centralized/Distributed	Random (CSMA)	Receiver Initiated
[173]	Distributed	Random (CSMA)	Receiver Initiated

1.2.3 The Link Layer

The link layer protocols can be classified in two different sub-layers based on their main functionalities: the Media Access Control (MAC) sub-layer, aimed at coordinating the access to the channel in case of concurrent transmissions; the Logical Link Control (LLC) sub-layer, used for recovering lost bits during transmission and propagation processes [117]. Due to restricted capabilities of nano-devices in terms of computation complexity and energy budget, traditional MAC and LLC protocols cannot be directly applied to terahertz-band nano-networks [151], [152]. Accordingly, the scientific community proposed several new link layer protocols in the last decade [153]. In what follows, they are analyzed by considering the networks topologies, the channel access mechanisms, and the initial access mechanisms (see Table 1.4).

Network Topologies for MAC Protocols

Existing MAC protocols can be firstly categorized according to their network topology. Different network topologies, denoted below as centralized, clustered, and distributed, are properly conceived for different application scenarios.

- *Centralized Topology.* In the centralized topology, the coordination among involved nano-devices is provided by a central node, like a controller or an access point. Due to limited energy and computational capabilities of traditional nano-devices, this topology is particularly feasible for nanoscale applications [154]–[157]. In this case, nano-sensors simply send collected information to a controller, usually capable of performing heavy computation, scheduling and transmission tasks, thus preserving their limited energy budget [158]. Though the reduced energy consumption of the centralized approach, it presents several issues in terms of complexity, scalability, and delivery latency [117].

- *Distributed Topology.* To strongly reduce the network complexity and the communication latency, the scientific community on nano-networks also proposed several distributed topologies. In this case, each node autonomously and locally determines its optimal transmission time in order to maximize the traffic rate while guaranteeing delivery deadlines [159] or to maximize the ratio between the transmission time and the energy harvesting time [160]. However, in this approach each node must be aware of environment and physical layer conditions in order to manage itself, also requiring higher computational capabilities [163], [164].
- *Clustered Topology.* The cluster-based topology provides a trade-off between centralized and distributed networks. In clustered topology, in fact, a limited number of nodes forms a group and elects a cluster head which manages the cluster behavior and transmits collected information to external gateways [153]. The cluster head can be a nano-device with higher computational and energy capabilities, responsible for assigning transmission and harvesting slots to nano-devices based on their energy budget [166] or managing inter and intra-cluster communications in dense nano-networks [142], [167].

Channel Access Mechanisms

In nano-networks, the scientific literature mainly focuses on channel access protocols based on random or scheduled mechanisms, thus guaranteeing the strict constraints of nano-devices. These two approaches are discussed below.

- *Random Channel Access.* In random channel access, each node transmit information when it is needed in a random way without waiting. The very short duration of transmitted pulse in terahertz band communications, in fact, drastically reduces the probability of having collisions [153]. Accordingly, several works propose different random access schemes, such as carrier sensing-based protocols (e.g., slotted Carrier Sense Multiple Access with Collision Avoidance (CSMA/CA) [157], [159]), Aloha-based channel access schemes (e.g., Smart-MAC) [168], or random channel access with multiple radios [169]. However, these mechanisms are not suitable for applications in which higher number of nano-nodes are used. In fact, when the number of nodes is higher, random access schemes can pose several challenges including collisions, transmission delays, and higher energy consumption which cannot be satisfied by the limited sensing, computation, battery and memory capacity of nano-devices [153].
- *Scheduled Channel Access.* Scheduled channel access mechanisms aim at solving the energy issue by designing in advance the channel slots at the cost of high synchronization overhead and, thus, high latency and low throughput [153]. Specifically, two main scheduled approaches are developed for nano-networks: the Time Division Multiple Access (TDMA) and the Frequency and

Time Division Multiple Access (TDMA). In TDMA-based mechanisms, nano-devices transmit information data only in assigned time slots. The time slot assignment can be performed by a nano-controller based on the dimension of data to be transmitted, the energy budget of nano-nodes, or the communication distance [155], [156], [166]. To manage very high number of nodes, instead, the scientific literature proposes the FTDMA-based scheme. In this case, the time slot selection is combined with frequency selection strategies in order to minimize energy consumption and increase channel capacity [170], [171].

Initial Access Mechanisms

The communication between transmitter and receiver nano-node starts with an initial handshake mechanism useful for defining physical parameters and beam alignment [153]. Nano-networks mainly exploits two type of handshake protocols which are transmitter initiated or receiver initiated.

- *Transmitter Initiated MAC Protocols.* Most of terahertz band MAC protocols consider a transmitter initiated mechanism where the transmitter nano-device starts the handshake procedure whenever it has data to send [152]. In this case, the transmitter send a transmission request containing communication parameters and channel coding scheme which are, then, accepted by the receiver nano-device with a transmission confirmation message. Transmitter initiated MAC protocols are usually adopted in distributed networks aiming at maximize the throughput without considering the energy efficiency [159], [161]. However, they can be also combined with energy harvesting schemes in order to balance the energy harvesting and consumption procedures [134], [162], [167]. Though these MAC protocols provide simplicity, low delay and high throughput, they suffer from high handshake overhead, thus reducing communication performance [153].
- *Receiver Initiated MAC Protocols.* Communication performance can be improved by considering receiver initiated MAC protocols. In fact, when the transmitter nano-device sends a message, it can be received only if the receiver nano-device has enough energy for the reception procedure. Accordingly, in order to save energy and reduce communication overhead, the handshake procedure can be initiated by the receiver itself when it has sufficient energy budget. In this case, the receiver nano-device transmits a request to receive packet to the whole nano-networks, thus communicating the amount of available energy and its status. This scheme is largely considered for centralized nano-networks [163]–[165], also reducing the message overhead by following a one-way handshake scheme [172], [173].

1.2.4 The Physical Layer

The physical layer allows to transform logical bits in an analogical signal and transmit it through a physical link which interconnects the transmitter and receiver nano-devices. Accordingly, this layer defines the modulation scheme adopted to encode the binary information and the transmission strategies (i.e., how the transmission power is distributed in the frequency domain).

Modulation Schemes

In terahertz-band communications, the information is generally encoded by using short pulses spread over a large bandwidth. Among all the possible approaches, the scientific literature considers the Time Spread On-Off Keying (TS-OOK) as the most promising modulation technique for the nanoscale, able to ensure both high energy and communication efficiency [116] [174]. With TS-OOK, a logical 1 is encoded as a short pulse and a logical 0 is encoded as a silence. Moreover, the time interval between two consecutive pulses is much longer than the pulse duration. Consequently, three important advantages are ensured: the nano-devices have not to be synchronized; the medium can be shared among multiple users without risk of collisions; the nano-devices can harvest energy during off periods [117].

Transmission Strategies

At the nanoscale, communication performance in terms of capacity and SNR strongly depends on the transmission strategy describing different distribution of the transmitted power in the frequency domain. Nowadays, the scientific literature mainly considered three transmission strategy, described below.

- *Flat Transmission Strategy.* The simplest way to allocate power in frequency domain is the flat communication strategy. In this case, the transmission power is uniformly distributed across the entire bandwidth without any criteria or restrictions [1]. The resulting power spectral density is flat for frequencies belonging to the operative bandwidth, otherwise it is equal to 0.
- *Optimal Transmission Strategy.* The optimal communication scheme allocate the transmission power in order to maximize the channel capacity based on the properties of communication channel (i.e., the total signal power must be optimally distributed in the sub-bands which experience better channel conditions) [1]. To this end, it is formulated an optimization problem solved by following three constraints: first, the total transmission power must be lower than the maximum available power over the entire operative bandwidth; second, the power allocated in a single sub-band must be a fraction of the total transmission power; third, the transmission sub-channels must be adjacent.

- *Pulse-Based Transmission Strategy.* Given that the aforementioned transmission strategies appear as ideal power allocation schemes, the scientific literature focuses on a third possible approach, named pulse-based communication. In this case, the transmitter nano-device exploits innovative graphene-based nano-antennas to generate a pulse modeled with a n -th derivative of a Gaussian shape [1].

1.2.5 Energy-Harvesting and Energy-Aware Schemes for Terahertz-Band Communications

Restricted dimensions of nano-devices strongly limit the amount of energy budget useful for communication purposes at the terahertz band, thus impairing network performance [131]. Accordingly, the scientific literature evaluated different strategies for feeding nano-devices and providing continuous operations, such as the adoption of nano-batteries and energy harvesting schemes. For instance, nano-batteries composed by lithium [175] or silicon atoms encapsulated by a conductive carbon layer [176] are presented as potential opportunity for powering nano-devices. However, given the size restrictions and typical application scenarios, nano-batteries can be hard to replace once they are exhausted [131]. Regarding energy harvesting mechanisms, instead, it is worthwhile to note that traditional harvesting techniques (exploiting solar, thermal, and wind sources) are inefficient at the nanoscale. Thus, it is important to introduce new energy harvesting models, like those using mechanical and chemical sources [110], [165]. Among the others, piezoelectric nanogenerators composed by lead zirconate titanate [93] or Zinc Oxide [85] nanowires are widely considered as promising solutions for retrieving energy at the nanoscale. Here, the vibrations or motions existing in the surrounding environment bend or compress the nanowires generating an electric current at their ends which charges an ultra-nanocapacitor [114]. The sources compressing the nanowires can have a wide range of frequencies depending on the considered application scenario (e.g., 1 Hz for the human heartbeat, 50 Hz for the air conditioning system of an office) [94].

Nowadays, several contributions already studied the usage of piezoelectric nanogenerators in nanoscale wireless communications. For example, [94] and [177] model the energy state of nano-devices through Markov chain, while jointly considering the energy harvesting rate and the energy consumption due to the communication process. The study presented in [162] theoretically investigates the achievable throughput of energy harvesting nanonetworks. Other contributions formulate energy-aware mechanisms at different levels of the protocol stack: the energy budget is used to define the time between two consecutive transmissions at the physical layer [97], to control data dissemination in a wireless nano-sensor network [135], [141], and to properly manage the MAC protocol [159], [160], [163]–[166].

Chapter 2

Channel Modeling and Energy-Aware Transmission Strategies for Terahertz Communications

The first Chapter of this thesis work demonstrated that the new frontier of nanotechnology is mainly supporting the design of novel and advanced biomedical applications. Here, the interaction among involved nano-devices can be enabled by nanoscale wireless communications in the terahertz band [117]. Starting from these premises, this Chapter firstly investigates physical transmission rates and communication ranges reachable in human tissues by modeling the communication channel as a non-homogeneous and dispersive stratified medium, where each layer (stratum corneum, epidermis, dermis and fat) is defined by its dielectric properties and thickness [178]. Here, the electromagnetic field and the Poynting vector are calculated by using the Finite-Difference Time-Domain (FDTD) technique, able to directly solve the Maxwell equations in time domain. Starting from the aforementioned channel model, the total path loss (expressed as the sum of spreading and absorption path loss), the molecular noise temperature, and the noise power spectral density are evaluated as a function of the communication frequency and the distance between transmitter and receiver. To make the study more general as possible, two system configurations (i.e., bottom-up and top-down) and three transmission strategies (i.e., flat, pulse-based, and optimal) are considered. In this context, since the communication process is energy-consuming, the usage of energy-aware and energy harvesting mechanisms is extremely important to achieve long-lasting communications at the nanoscale [110]. Accordingly, this Chapter also investigates a power control mechanism based on the feedback control theory by considering a specific system configuration and transmission scheme. The control law is properly conceived for managing the communication in human tissues, where nano-devices are equipped with a piezoelectric nanogenerator. The amount of energy spent to transmit an information message is dynamically tuned by a proportional controller in a closed-loop control scheme which jointly considers harvesting and discharging processes.

2.1 The System Model

To deal with nanoscale communications and networking, it is important to know how the signal propagates across the medium. Accordingly, this Section develops an accurate channel model, taking into account two possible configurations depicted in Figure 2.1. The first one refers to the top-down configuration, where it is assumed that the transmitter is positioned outside the human body (but attached to the skin) and the receiver is implanted. The second one refers to the bottom-up configuration, where the position of transmitter and receiver is inverted with respect to the previous case. The resulting channel model embraces absorption path loss, spreading path loss, molecular noise temperature, and noise power spectral density. Such models will be used for evaluating the SNR and the communication capacity as a function of the distance between transmitter and receiver.

2.1.1 Total Signal Path Loss

The total signal path loss, i.e., $A(f, z)$, defines the total level of attenuation offered to the signal that propagates across the medium as a function of the distance between transmitter and receiver z and the communication frequency f . According to [1], it jointly takes care about the absorption path loss due to the absorption of human tissues, i.e., $A_{abs}(f, z)$, and the spreading path loss generated by the expansion of waves in human body, i.e., $A_{spread}(f, z)$. Thus, $A(f, z)$ is defined as:

$$A(f, z) = A_{spread}(f, z) + A_{abs}(f, z). \quad (2.1)$$

On the one hand, when an electromagnetic wave propagates through the medium, several molecules are excited and start to vibrate. In this case, part of the energy carried by the electromagnetic wave is lost or converted to kinetics energy [1]. The absorption path loss or molecular loss, i.e., $A_{abs}(f, z)$, describes the attenuation produced by the vibration of molecules as a function of both distance between transmitter and receiver, d , and communication frequency, f , that is:

$$A_{abs}(f, z) = 10 \log \frac{\mathbf{S}(f, z)}{\mathbf{S}(f, z_0)} = 10k(f)d \log e, \quad (2.2)$$

where \mathbf{S} is the Poynting vectors, z_0 is the z -coordinate of the reference section, $d = z - z_0$ is the considered path length and $k(f)$ is the medium absorption coefficient.

On the other hand, the spreading path loss, i.e., $A_{spread}(f, z)$, refers to the attenuation due to the expansion of an electromagnetic wave propagating through a given medium. It is defined as:

$$A_{spread}(f, z) = 20 \log \left(4\pi \int_{z_0}^z \frac{dz}{\lambda_g(f, z)} \right), \quad (2.3)$$

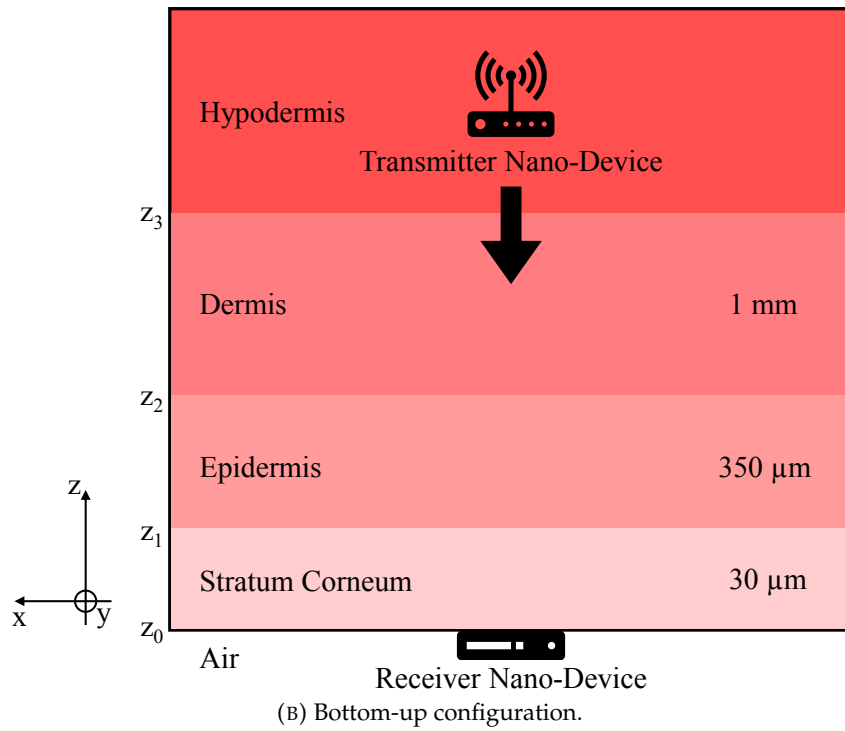
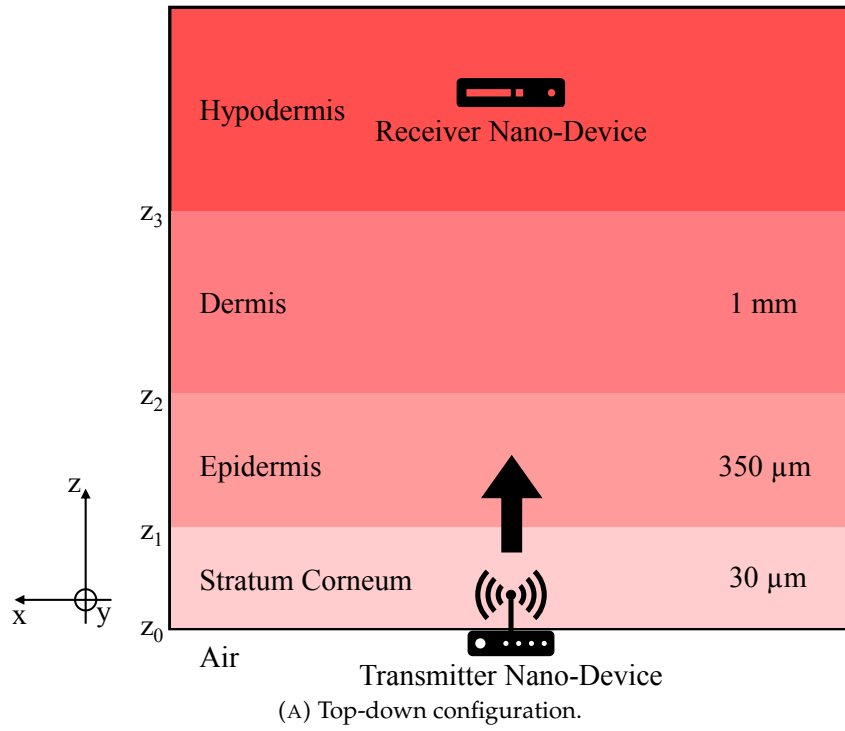


FIGURE 2.1: The possible considered transmitter and receiver configurations.

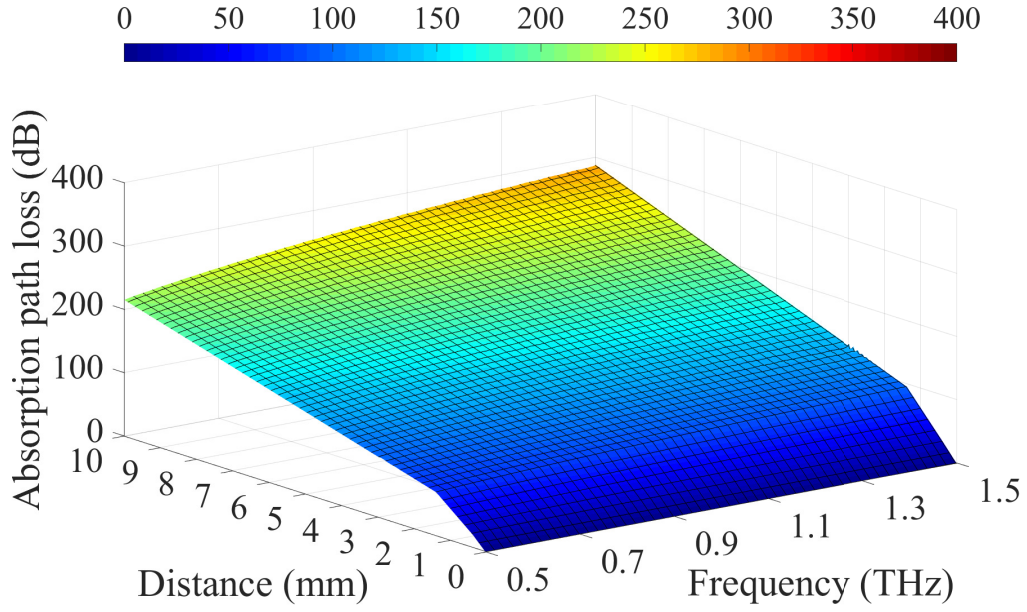


FIGURE 2.2: Absorption path loss as a function of frequency and transmission range, evaluated for the top-down configuration.

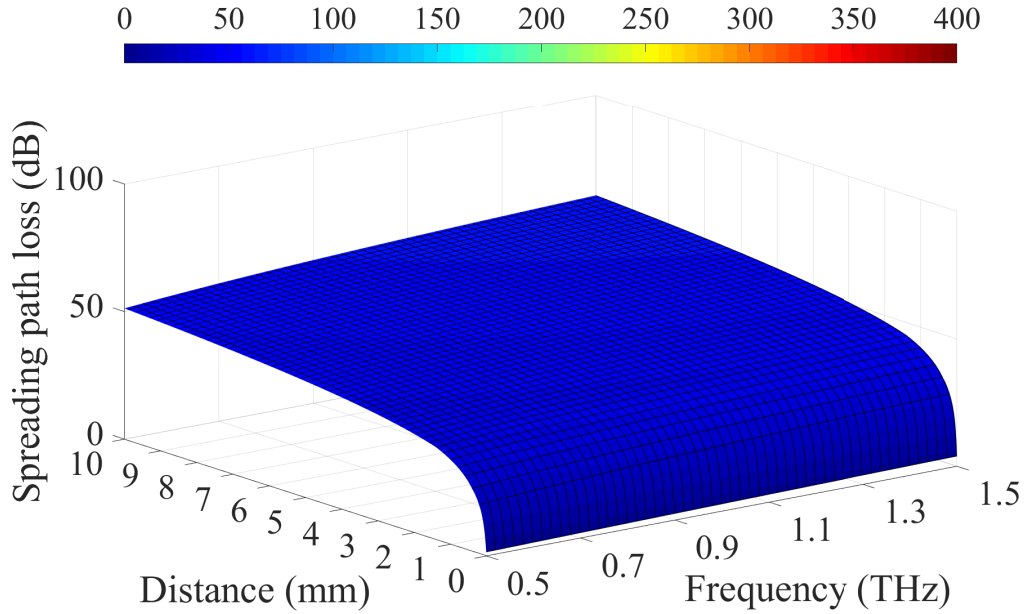
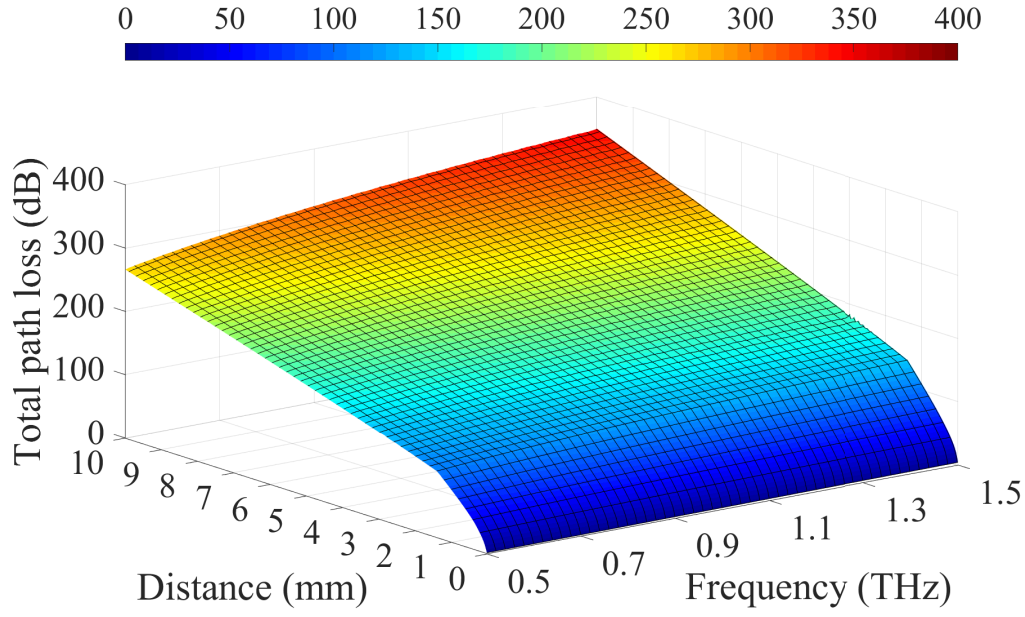


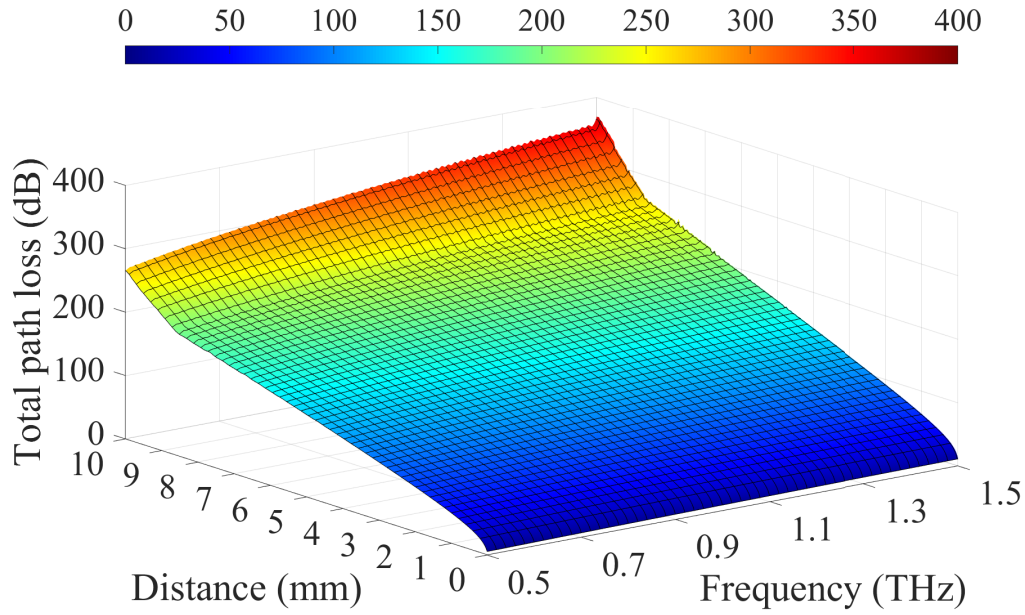
FIGURE 2.3: Spreading path loss as a function of frequency and transmission range, evaluated for the top-down configuration.

where λ_g takes into account the stratified medium and depends on the distance from the air-skin interface. Specifically, λ_g can be expressed as [178]:

$$\lambda_g(f, z) = \begin{cases} \lambda_{g,1}(f, z) & 0 \leq z \leq z_1 \\ \lambda_{g,2}(f, z) & z_1 \leq z \leq z_2 \\ \lambda_{g,3}(f, z) & z_2 \leq z \leq z_3 \\ \lambda_{g,4}(f, z) & z \geq z_3, \end{cases} \quad (2.4)$$



(A) Top-down configuration.



(B) Bottom-up configuration.

FIGURE 2.4: Total path loss as a function of frequency and transmission range.

where

$$\lambda_{g,k} = \frac{\lambda_0}{\sqrt{\frac{\epsilon'_k}{2} \left[\sqrt{1 + \left(\frac{\epsilon''_k}{\epsilon'_k} + \frac{\sigma_k}{f\epsilon_0\epsilon'_k} \right)^2} + 1 \right]}} \quad k = 1, 2, 3, 4 \quad (2.5)$$

is the wavelength of the propagating wave within the k -th lossy medium, while λ_0 is the free-space wavelength.

Given the stratified channel model reported in Figure 2.1 and the resulting analytical formulations, Matlab scripts have been used to illustrate the behavior of the channel model in conceivable nanoscale scenario. Specifically, the absorption path loss offered by human tissues in the bandwidth from 0.5 THz to 1.5 THz is shown in Figure 2.2. Without loss of generality, the reported results consider the top-down configuration. The absorption path loss clearly appears as a frequency-selective attenuation, which grows up when both transmission range and communication frequency increase.

Figure 2.3, instead, depicts the obtained spreading path loss in human tissues as a function of the transmission range and the communication frequency, evaluated for the top-down configuration. In general, the spreading path loss registers considerably high values at the nanoscale. But, in this specific use case, it appears negligible with respect to the level of attenuation provided by the absorption path loss.

Finally, Figure 2.4 shows the total path loss as a function of the distance between transmitter and receiver and the communication frequency, by taking into account both top-down and bottom-up configurations. Generally, the total path loss grows up when the communication frequency and the transmission range increase. However, the comparison between Figure 2.4 (a) and Figure 2.4 (b) shows how the outer skin layers introduce higher attenuation levels than the inner ones. Moreover, by comparing Figure 2.4 (a) with both Figure 2.2 and Figure 2.3, it is evident how the total path loss is mainly influenced by the molecular absorption, which generates a loss up to 6 times higher than the one introduced by the expansion phenomenon. Just to provide an example, with reference to the considered communication bandwidth, the maximum value of the spreading path loss is 60.3 dB, while the absorption path loss registers a maximum value equal to 287.2 dB. Moreover, reported results fully confirm that the Terahertz band is strongly frequency-selective: in fact, the propagation loss significantly increases with both communication frequency and transmission range.

2.1.2 Molecular Noise Temperature and Noise Power Spectral Density

Molecular absorption also generates the molecular noise. Specifically, the equivalent molecular noise temperature is computed as [178]:

$$T_{eq}(f, z) = T_0 \varepsilon(f, z) = T_0 \left[1 - \frac{\mathbf{S}(f, z)}{\mathbf{S}(f, z_0)} \right], \quad (2.6)$$

where T_0 is the reference temperature, equal to normal body temperature (i.e., $T_0 = 310\text{K}$), $\mathbf{S}(f, z)$ is the Poynting vector, and $\varepsilon(f, z)$ is the channel emissivity.

Starting from the equivalent noise temperature $T_{eq}(\omega, z)$, it is possible to evaluate the noise power spectral density, i.e., $N(\omega, z)$, as reported below:

$$N(f, z) = k_B T_{eq}(f, z), \quad (2.7)$$

where k_B is the Boltzmann constant (i.e., $k_B = 1.380658 \times 10^{-23} \text{ J/K}$).

Now, by assuming a transmission bandwidth equal to B , the noise power registered at the receiver side, i.e., $P_n(f, z)$, is evaluated as:

$$P_n(f, z) = \int_B N(f, z) df = k_B \int_B T_{eq}(f, z) df \quad (2.8)$$

It is evident how the molecular noise increases with communication frequency and transmission distance. This also suggests that it is highly frequency-selective, therefore non-white.

As depicted in Figure 2.5, the molecular noise temperature changes with communication frequency and transmission distance. Indeed, the internal vibrations of the medium molecules absorb the propagating electromagnetic field and convert the carried energy to kinetic energy (first) and heat (then). In this context, the emissivity of the channel could be expressed as a function of the absorption path loss and could be set equal to $1 - \mathbf{S}(f, z) / \mathbf{S}(f, z_0)$.

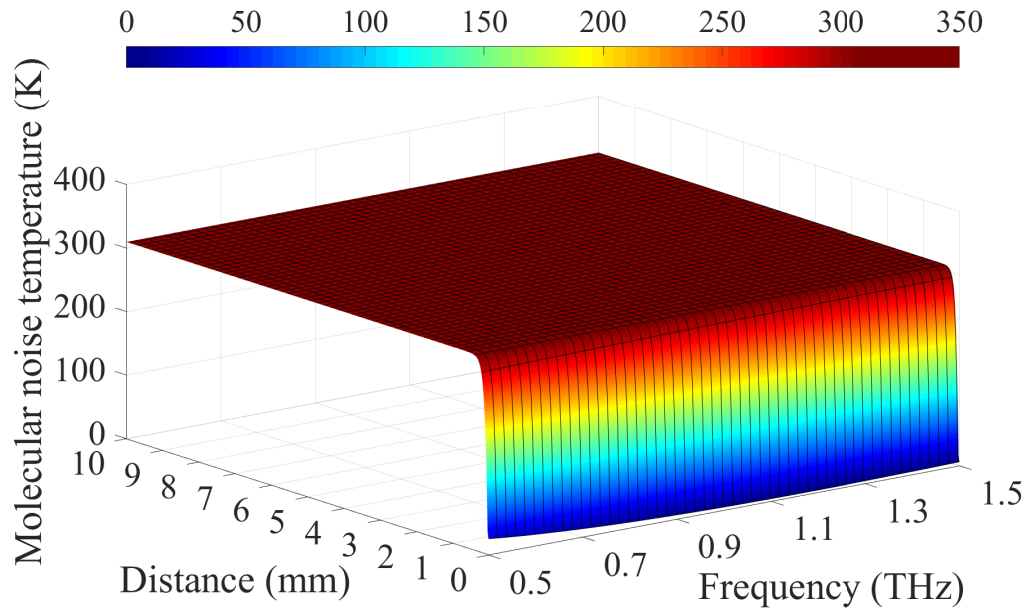
To provide further insight, both top-down and bottom-up configurations are taken into account. As already observed, the inner tissue layers register lower attenuation levels. Consequently, the molecular noise temperature increases slower when the bottom-up configuration is considered. On the other hand, in both configurations it is important to note that, at the level of millimeters, the equivalent molecular noise temperature is not very high, reaching maximum values approximately equal to 310 K (see Figure 2.5). The bounded level of the equivalent noise temperature suggests that a communication link, with a tolerable signal to noise ratio, can be established among transmitter and receiver located inside and outside the human tissues at the Terahertz band.

2.1.3 The Considered Transmission Techniques

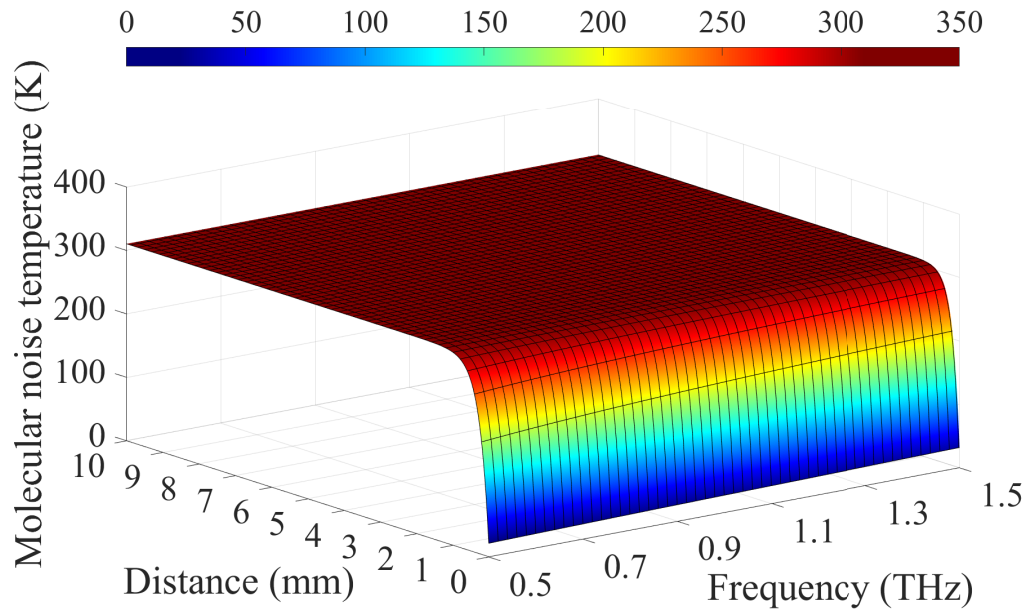
At the nanoscale, the communication capacity is strictly influenced by the transmission strategy and the adopted configuration (i.e., top-down and bottom-up configurations). Regarding the transmission strategies, this Chapter considers three approaches that differently distribute the transmitted power in the frequency domain. They are: flat, pulse-based, and optimal transmission schemes.

Thanks to the strong selectivity of the nanoscale communication channel, the SNR and the resulting upper bound of the channel capacity can only be evaluated by dividing the total bandwidth B into many narrow sub-bands lasting Δf , where the channel is non-selective in the frequency domain. Let $S(f_i, z)$ be the transmitted signal power spectral density of the generic transmission in the i -th sub-band centered at the frequency f_i at a distance z from the transmitter. The SNR for the i -th sub-band at a distance d , i.e., $SNR(f, z)$, can be computed as:

$$SNR(f_i, z) = \frac{S(f_i, z)}{A(f_i, z)N(f_i, z)}, \quad (2.9)$$



(A) Top-down configuration.



(B) Bottom-up configuration.

FIGURE 2.5: Molecular absorption noise temperature as a function of frequency and transmission range.

where $A(f_i, z)$ is the total channel path loss and $N(f_i, z)$ is the noise power spectral density.

According to the Shannon theorem, the upper bound of the resulting channel capacity can be evaluated by considering the summation of the sub-band contributions where the noise is supposed to be white. The resulting upper bound of the channel capacity is equal to:

$$C(z) = \sum_i \Delta f \log_2 [1 + \text{SNR}(f_i, z)] = \sum_i \Delta f \log_2 \left[1 + \frac{S(f_i, z)}{A(f_i, z)N(f_i, z)} \right]. \quad (2.10)$$

As demonstrated before, the total path loss $A(f_i, z)$ and the noise power spectral density $N(f_i, z)$ are influenced by the communication frequency and the distance between transmitter and receiver. On the contrary, the signal power spectral density $S(f_i, z)$ is influenced by the adopted transmission strategy. As a result, the channel capacity is strictly influenced by the adopted transmission strategy as well.

The Transmission Strategies

In what follows, let $B = f_M - f_m$ be the total available bandwidth, where f_m and f_M are the lower and the higher operative frequencies, respectively. When a pulse is transmitted the power P_{tx} is distributed in the frequency domain according to the flat, optimal, pulse-based communication scheme.

- *Flat Communication Strategy.* In the flat communication, the transmitted power spectral density is equal to:

$$S_{flat}(f, z) = \begin{cases} S_0 = \frac{P_{tx}}{B} & f_m \leq f \leq f_M \\ 0 & \text{otherwise} \end{cases} \quad (2.11)$$

- *Optimal Communication Strategy.* In the optimal communication scheme, instead, the signal power spectral density is computed by solving the optimization problem:

$$\text{maximize} \left\{ \sum_i \Delta f \log_2 \left[1 + \frac{S_{opt}(f_i, z)}{A(f_i, z)N(f_i, z)} \right] \right\} \quad (2.12)$$

by jointly taking into account the following three constraints:

1. The total transmission power, expressed as the sum of the signal power spectral density for each sub-bands multiplied by the sub-channel width Δf , cannot exceed the maximum available power over the entire bandwidth P_{tx} :

$$\sum_{i \in \Omega} S_{opt}(f_i, z) \Delta f \leq P_{tx}; \quad (2.13)$$

2. The power in a single sub-band should be a fraction, γ , of the total transmission power:

$$S_{opt}(f_i, z)\Delta f \leq \gamma P_{tx} \quad \forall i \in \Omega, \gamma \in]0, 1]; \quad (2.14)$$

3. The chosen transmission sub-channels must be adjacent:

$$\Omega = \{i | i_{min_\Omega} \leq i \leq i_{max_\Omega}\}. \quad (2.15)$$

The optimization problem formulated in Eq. (2.12) can be solved by using the method of Lagrange multipliers and verifying the three aforementioned constraints. First of all, by considering the first constraint, the optimization problem can be expressed as:

$$\max \left\{ \sum_i \Delta f \left(\log_2 \left[1 + \frac{S_{opt}(f_i, z)}{A(f_i, z)N(f_i, z)} \right] + \lambda S_{opt}(f_i, z) \right) - P_{tx} \right\} \quad (2.16)$$

where λ is the Lagrange multiplier. To find the maximum value, the derivative of the argument of Eq. (2.16) with respect to $S_{opt}(f_i, z)$ is put equal to zero, thus obtaining:

$$\ln(2)[S_{opt}(f_i, z) + A(f_i, z)N(f_i, z)] = \lambda^{-1} \quad \forall i \quad (2.17)$$

As a consequence, the overall channel capacity is maximized when:

$$S_{opt}(f_i, z) = \beta - A(f_i, z)N(f_i, z), \quad (2.18)$$

where β is a constant value which can be computed by means of an iterative procedure, following the water-filling principle. In particular, at the n -th step, β is equal to:

$$\beta(n) = \frac{1}{L(n)} \left[\frac{P_{tx}}{\Delta f} + \sum_i A(f_i, z)N(f_i, z) \right], \quad (2.19)$$

where $L(n)$ is the number of sub-bands at the n -th step. In details, to evaluate $L(n)$ value, the signal power spectral density $S_{opt}(f_i, z)$ is computed by considering Eq. (2.18): if $S_{opt}(f_i, z) \leq 0$, the corresponding value is set to 0 and the considered sub-band is excluded for the following iterative cycles. The procedure can be stopped when there are no other sub-bands with a negative $S_{opt}(f_i, z)$ value. At the end, the total signal power appears optimally distributed in the sub-bands which experience better channel conditions.

It is important to remark that, due to the monotonic behavior of the total path loss, as demonstrated in the previous Section, the selected sub-bands are already adjacent and, consequently, the third constraint is intrinsically respected.

- *Pulse-Based Communication Strategy.* Flat and optimal transmission schemes, in

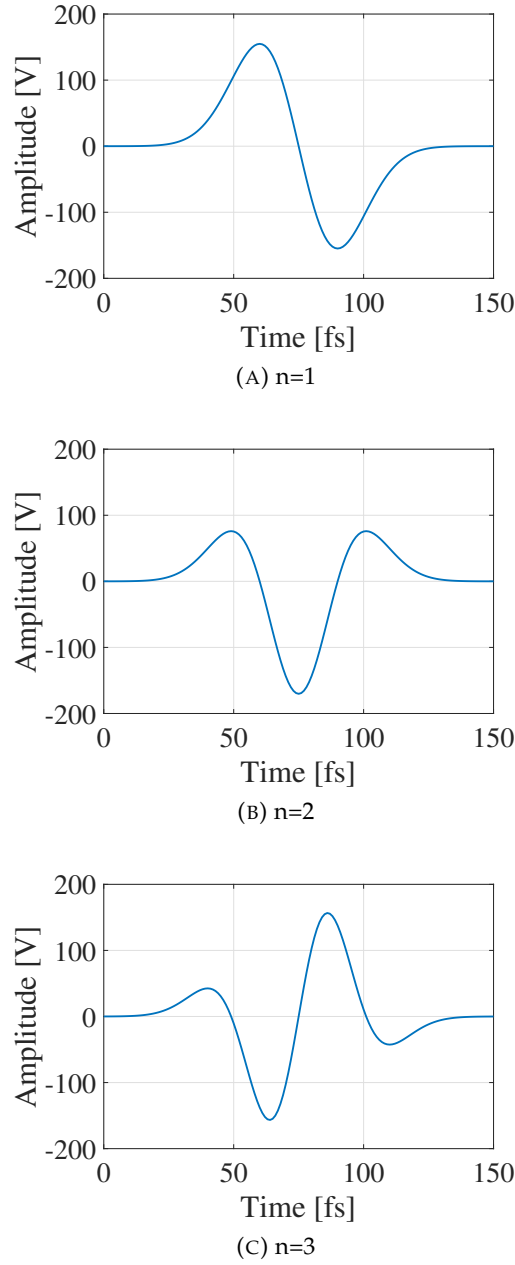


FIGURE 2.6: Examples of pulses generated with the pulse-based communication scheme.

fact, are ideal approaches. Nanotechnology (and in particular graphene-based nano-antennas), instead, allows the transmission of pulses having Gaussian shapes in the time domain. Let $p(t) = \frac{1}{s\sqrt{2\pi}}e^{-(t-\mu)^2/(2s^2)}$ be a Gaussian-based pulse, where μ is its mean value and s is the related standard deviation. The pulse-based communication approach models the transmitted pulse through the n -th derivative of $p(t)$, whose representation in the frequency domain is:

$$\phi^{(n)}(f, z) = (2\pi f)^{2n} e^{(-2\pi s f)^2} \quad (2.20)$$

Thus, the signal power spectral density of the n -th time derivative is still Gaussian-shaped and could be described as:

$$S_{pulse}^{(n)}(f, z) = a_0^2 \phi^{(n)}(f, z) = a_0^2 (2\pi f)^{2n} e^{(-2\pi s f)^2}, \quad (2.21)$$

where a_0 is a normalizing constant to adjust the pulse total energy, which is obtained as $a_0^2 = P_{tx} / \int_{f_m}^{f_M} \phi(f, z) df$.

Figure 2.6 shows examples of Gaussian-based pulses, obtained by setting n in the range from 1 to 3. Note that, while the pulse duration remains constant (i.e., equal to $100fs$), the number of oscillations grows up with the derivative order n .

2.1.4 Analysis of Physical Transmission Rates and Communication Ranges

In what follows, it is considered the TS-OOK as modulation scheme. Accordingly, the bit 1 is encoded with a femto-second long pulse and the bit 0 is encoded with the silence. In line with [1], [94], [116], [141], [179], [180], the performance of a nanoscale communication system are evaluated by assuming that the pulse energy and the pulse duration are equal to $500pJ$ and $100fs$, respectively. Thus, the resulting amount of power for each transmitted pulse is set to $P_{tx} = 500pJ / 100fs = 5kW$. Furthermore, when the pulse-based communication strategy is evaluated, the derivative order n of the Gaussian pulse is chosen in the range from 1 to 3 (as already shown before). Whereas, its standard deviation s is set to 0.15. Note that the aforementioned parameters are used only to test the behavior of the proposed channel model without considering any energy constraints.

The Computed SNR

Figures 2.7, 2.8, and 2.9 show the SNR estimated for top-down configuration with flat, pulse-based, and optimal transmission schemes, respectively. Similarly, Figures 2.10, 2.11, and 2.12 depict the SNR estimated with different transmission schemes for bottom-up configuration. First of all, it is possible to observe that these configurations show a common behavior. In both cases, accordingly to the total path loss trend, the SNR grows up when the communication frequency and the distance between source and destination node decrease. On the other hand, given the distance from the source node, the bottom-up configuration registers higher values of SNR than the top-down approach. This is again justified through the total path loss behavior: the inner layers of the stratified medium introduce lower path loss than the outer ones. This anticipates that the direction of the communication in human tissues influences the resulting link capacity.

Furthermore, by taking into account different communication schemes, the behavior of flat and pulse-based transmission strategies is not completely the same,

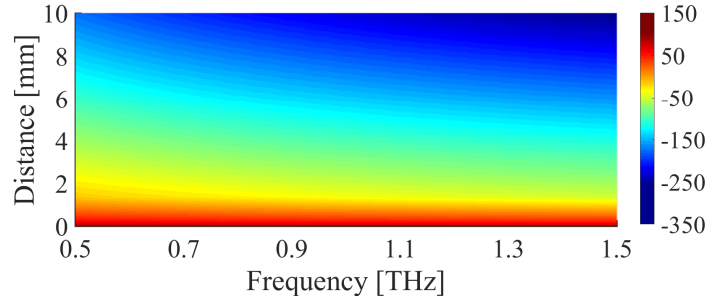


FIGURE 2.7: SNR obtained for the top-down configuration with flat transmission.

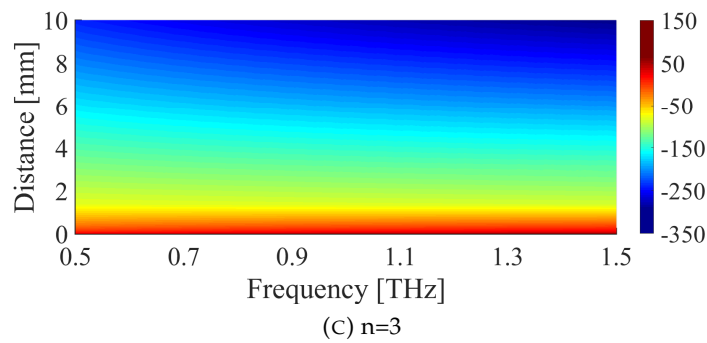
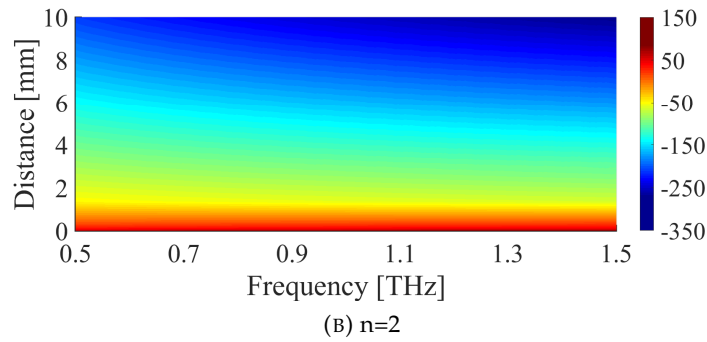
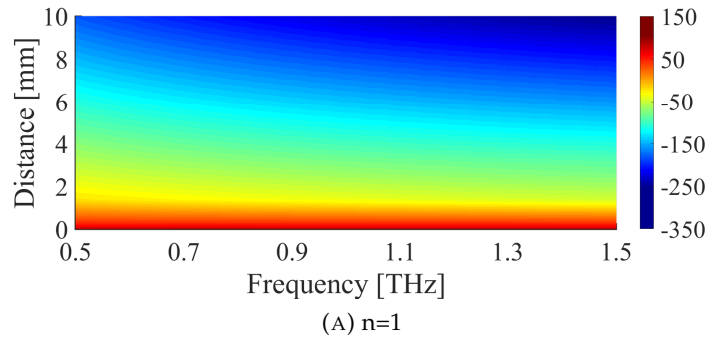


FIGURE 2.8: SNR obtained for the top-down configuration with pulse-based transmission.

and this will bring to different values of the communication capacity (as illustrated later). Moreover, the study of the optimal transmission scheme brings to two important considerations. First, it is possible to note that the SNR can be evaluated only for a limited portion of the bandwidth, based on the power profile solution of the optimization problem. Second, the adoption of the optimal power profile brings to

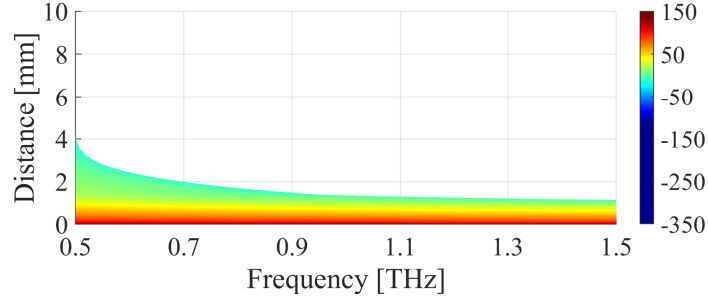


FIGURE 2.9: SNR obtained for the top-down configuration with optimal transmission.

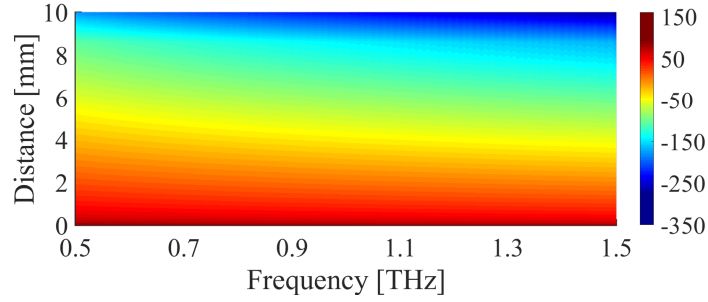


FIGURE 2.10: SNR obtained for the bottom-up configuration with flat transmission.

SNR values that slightly reduces with the distance between communicating nodes, while maintaining similar values in the frequency domain.

The Obtained Channel Capacity

The upper bound of the channel capacity, obtained according to Eq. (2.10), is depicted in Figure 2.13 and Figure 2.14. Also in this case, several differences can be observed between top-down and bottom-up configurations. As already envisioned, given the distance from the source node, the bottom-up direction ensures higher channel capacity. On the other hand, in any case, the channel capacity decreases with the transmission range. This clearly highlights the destroying effect of the path loss, which is even more evident when the distance between transmitter and receiver increases.

As expected, the optimal transmission scheme reaches optimal performance. At the same time, the more realistic approach, based on the transmission of Gaussian-based pulses, generally achieves the lowest performance, which in turn get worse when the derivative order n of the Gaussian-based pulse increases. In summary, it is possible to conclude that a channel capacity in the order of Tbps can be only reached for transmission ranges less than 2 mm and 4 mm when the top-down and the bottom-up configuration are considered, respectively. Furthermore, when the distance between the source node and the destination device exceeds 9 mm (top-down) and 9.5 mm (bottom-up), communication capabilities are extremely injured (i.e., the channel capacity becomes lower than 1 bps).

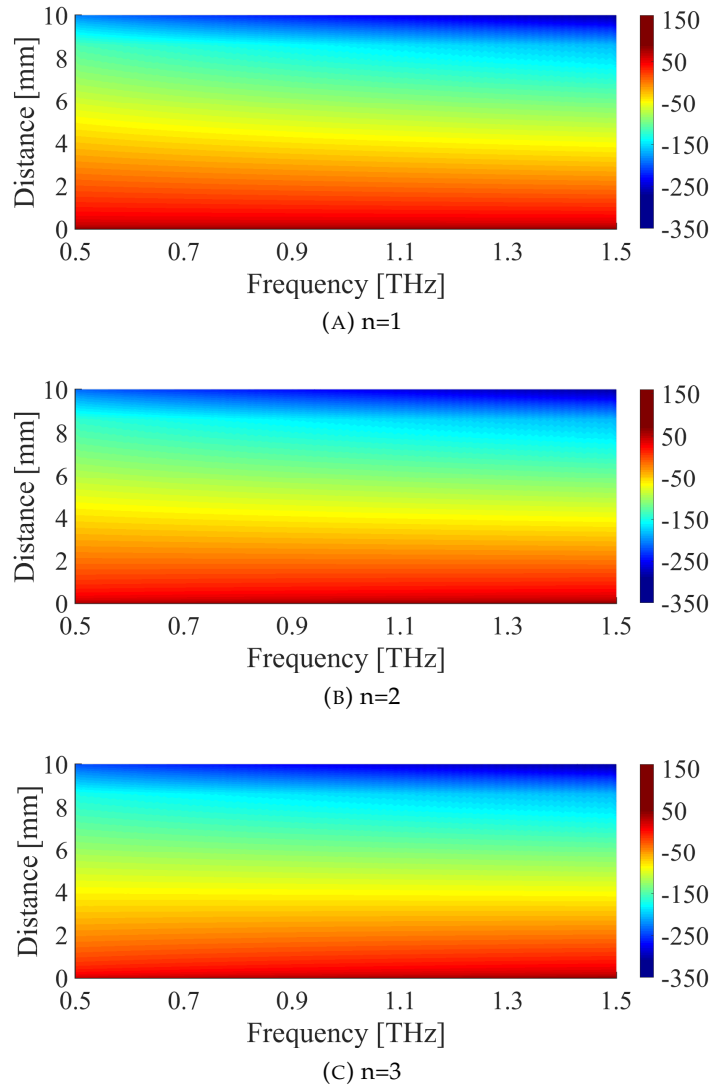


FIGURE 2.11: SNR obtained for the bottom-up configuration with pulse-based transmission.

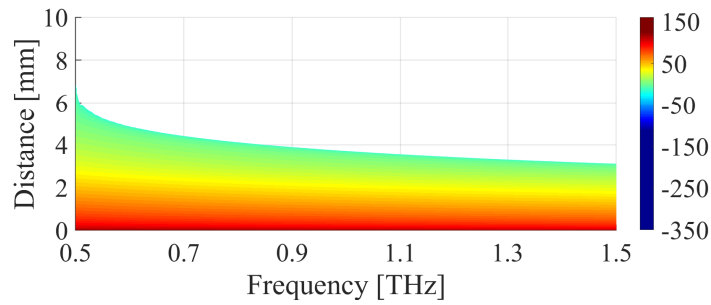


FIGURE 2.12: SNR obtained for the bottom-up configuration with optimal transmission.

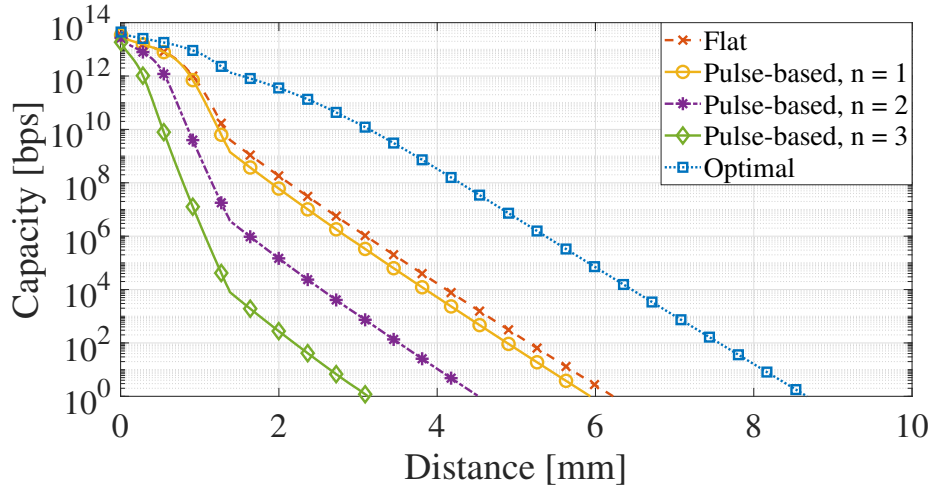


FIGURE 2.13: Channel capacity as a function of the transmission range, evaluated for the top-down configuration.

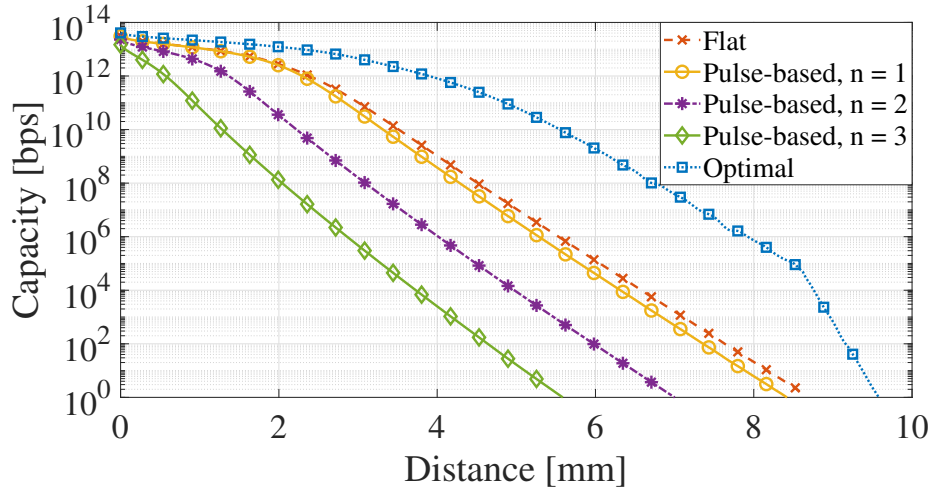


FIGURE 2.14: Channel capacity as a function of the transmission range, evaluated for the bottom-up configuration.

2.1.5 Final Considerations

This Section investigated physical transmission rates and communication ranges reachable in human skin. To this end, a sophisticated channel model taking into account the spatial dependence of the skin permittivity has been formulated. Indeed, electromagnetic field and the Poynting vector were calculated by using the FDTD technique, while path loss, noise power spectral density, and SNR were evaluated as a function of the communication frequency and the distance between transmitter and receiver. Starting from these models, physical transmission rates and communication ranges have been calculated by varying the transmission techniques and the positions of both transmitter and receiver. The obtained results demonstrate that a physical data rate in the order of Tbps can be only reached for transmission ranges

less than 2 mm. When the distance between transmitter and receiver exceeds 9 mm, communication capabilities are extremely impaired (i.e., the physical data rate tends to be lower than 1 bps). These important findings are extremely useful to drive future research activities devoted to the design of innovative networking methodologies, protocols, and algorithms for the nanoscale.

2.2 The Control System

Starting from the system model previously described, this Section considers a nano-device implanted in the human body and fed by a piezoelectric nanogenerator. It is able to collect biomedical information (e.g., the presence of sodium, glucose, other ions in blood, cholesterol, cancer biomarkers, and other infectious agents) and communicate them to a receiver positioned on the skin surface by means of electromagnetic waves in the terahertz band (i.e., bottom-up configuration). Then, the obtained information can be transmitted to a remote device through traditional communication paradigms. The reference scenario is depicted in Figure 2.15.

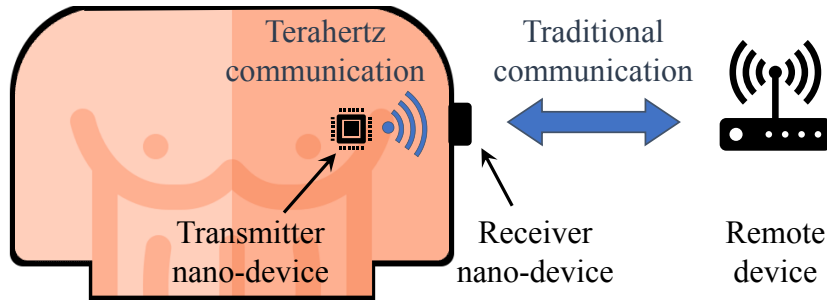


FIGURE 2.15: The reference scenario.

The main analytical symbols used in this Section are reported in Table 2.1.

2.2.1 Transmission Scheme and Resulting Channel Capacity

At the physical layer, the nano-device sends messages of M bits by using the TS-OOK modulation scheme. These messages are generated according to a Poisson distribution with parameter λ . The duty cycle of the signal to transmit represents the ratio between the total amount of time spent to transmit the bits 1 of a frame and the frame duration itself. Thus, considering a probability of bit 1 equal to ω , a pulse duration of T_p , and an average inter-arrival message time $1/\lambda$, the average duty cycle of the signal to transmit is equal to:

$$\bar{\eta} = \omega M T_p \lambda. \quad (2.22)$$

With TS-OOK, the bit 1 is encoded by means of a short pulse (i.e., $T_p = 100$ fs), and the bit 0 is represented by the silence. The pulse shape is modeled as a derivative of the Gaussian function with mean μ and standard deviation σ : $s(t) =$

TABLE 2.1: List of the main symbols used in this Section.

Symbol	Description
T_p, E_p	Time interval needed to transmit a pulse and resulting consumed energy
M	Number of bit per frame
λ	Average number of frames per second
σ, μ	Standard deviation and mean of the Gaussian pulse
d	Distance between transmitter and receiver nano-devices
f, f_m, f_M	Communication frequency, lower operative frequency, and higher operative frequency
$A_{abs}(f, d), A_{spread}(f, d), A(f, d)$	Absorption, spreading, and total path loss
$S(f), N(f, d)$	Signal power spectral density and noise power spectral density
$\mathcal{C}(d)$	Upper bound of the channel capacity
$\eta(t), \bar{\eta}$	Duty cycle of the signal to transmit and its average value
ω	Occurrence probability of bit 1
$v_n, i_n(t), R_n$	Generator voltage, generator current, and resistance of the circuit modeling the harvesting process
h_n	Amount of harvested energy per cycle
t_n	Time duration of the harvesting cycle
C_n	Capacitance of the ultra-nanocapacitor
$i_c(t)$	Current through the ultra-nanocapacitor
$i_l(t)$	Load current modeling the discharging process
g	Proportional gain of the controller
$V_c(t), \dot{V}_c(t)$	Voltage across the ultra-nanocapacitor and its variation
E_0	Set point of the closed-loop control scheme
E	Available energy budget at the ultra-nanocapacitor
E_{min}	Minimum amount of energy required to transmit bit 1
E_c	Amount of energy consumed per frame at the equilibrium
V_∞	Equilibrium point of the closed-loop control scheme

$(\sigma\sqrt{2\pi})^{-1}e^{-(t-\mu)^2/(2\sigma^2)}$ [1]. Considering the first derivative of that Gaussian function, the signal power spectral density of the pulse-based signal is:

$$S(f) = \left(\frac{E_p T_p}{\int_{f_m}^{f_M} (2\pi f)^2 e^{(-2\pi\sigma f)^2} df} \right) (2\pi f)^2 e^{(-2\pi\sigma f)^2} \quad (2.23)$$

where E_p , f_m , and f_M are the energy associated with a transmitted pulse, the lower operative frequency and the higher operative frequency, respectively.

According to the Shannon theorem described in Section 2.1.3 and considering (2.23), the upper bound of the channel capacity is affected by the pulse energy, E_p :

$$\begin{aligned} \mathcal{C}(d) &= \sum_i \Delta f \log_2 [1 + \text{SNR}(f_i, d)] = \\ &= \sum_i \Delta f \log_2 \left[1 + \frac{\left(\frac{E_p T_p}{\int_{f_m}^{f_M} (2\pi f)^2 e^{(-2\pi\sigma f)^2} df} \right) (2\pi f_i)^2 e^{(-2\pi\sigma f_i)^2}}{A(f_i, d) N(f_i, d)} \right]. \end{aligned} \quad (2.24)$$

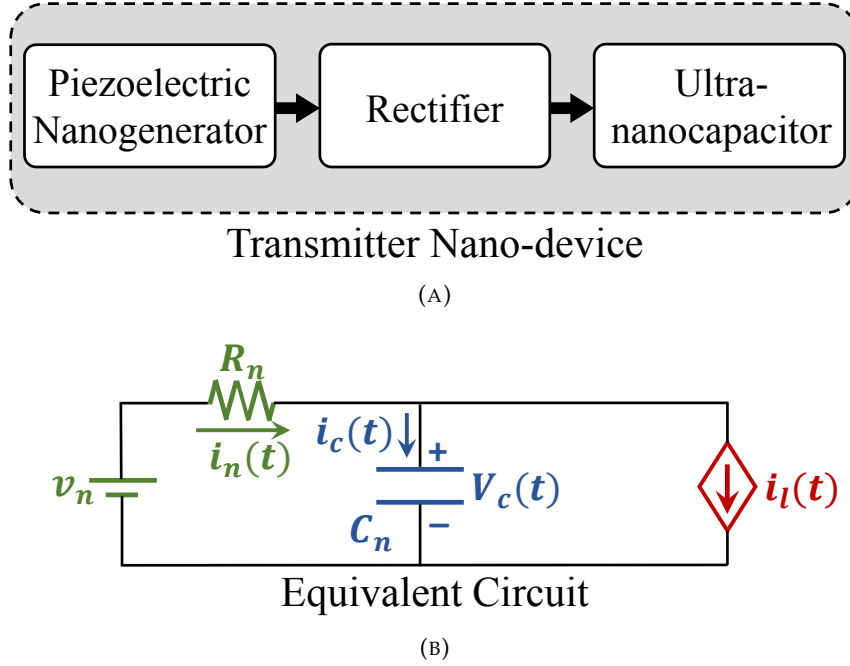


FIGURE 2.16: (a) Harvesting mechanism and (b) equivalent circuit modeling harvesting and discharging processes.

2.2.2 The Conceived Control Law

As depicted in Figure 2.16 (a), the nano-device retrieves energy from the vibrations in the surrounding environments by means of a piezoelectric nanogenerator composed by an array of ZnO nanowires [85], converts the alternating current in a direct one with a rectifier element, and stores the energy within an ultra-nanocapacitor. The retrieved energy is used to feed the communication processes.

The amount of energy available within the ultra-nanocapacitor is computed by jointly considering the harvesting and the discharging processes. According to [94], [177], the harvesting process is modeled through an ideal voltage source, v_n , in series with a resistor, R_n , and the ultra-nanocapacitor, C_n . This source generates an amount of charge per cycle, h_n , every t_n seconds. Let $i_n(t)$, $i_c(t)$ and $V_c(t)$ be the generator current, the current passing through the ultra-nanocapacitor and the voltage across the ultra-nanocapacitor, respectively. The discharging process, instead, is modeled as a current source in parallel with the ultra-nanocapacitor with a load current $i_l(t)$. The resulting equivalent circuit describing the harvesting and discharging processes is shown in Figure 2.16 (b).

The methodology investigated herein allows a nano-device to dynamically tune the energy consumed for the transmission of a M -bits long frame starting from the amount of available energy with a feedback control scheme. Accordingly, the load current $i_l(t)$ is dynamically tuned with a proportional controller. The control law is designed with the aim of obtaining a positive value of $i_l(t)$, causing a positive energy consumption during the transmission of information messages. Accordingly, the proportional gain can only be greater than 0 (i.e., $g > 0$) and the energy budget

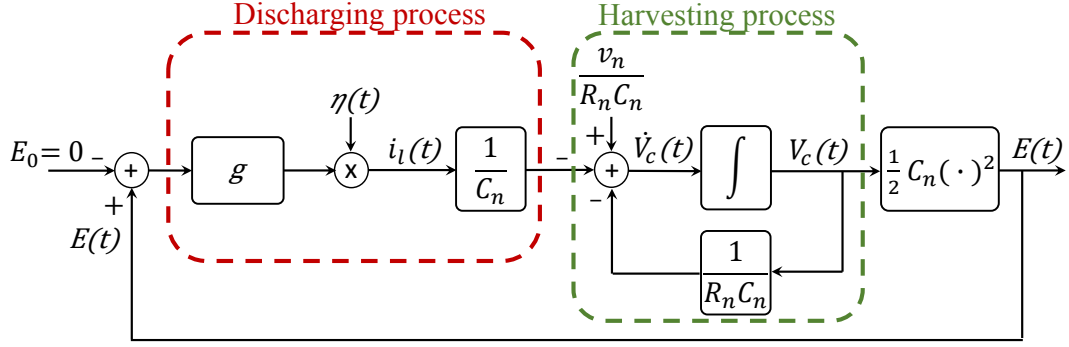


FIGURE 2.17: The investigated closed-loop control scheme.

available at the ultra-nanocapacitor, E , is used as feedback variable. Furthermore, a null set point is considered (i.e., $E_0 = 0$), so that the load current, $i_l(t)$, is proportional to the available energy budget. The resulting feedback control system, depicted in Figure 2.17, is analytically modeled by considering the voltage across the ultra-nanocapacitor, $V_c(t)$, as the state variable. The time variation of the voltage across the ultra-nanocapacitor, $\dot{V}_c(t)$, caused by the aforementioned harvesting and discharging processes is modeled by the following state equation:

$$\dot{V}_c(t) = \frac{v_n}{R_n C_n} - \frac{V_c(t)}{R_n C_n} - \frac{g\eta(t)V_c(t)^2}{2}. \quad (2.25)$$

Since $E = C_n V_c(t)^2 / 2$, the resulting closed-loop control scheme is nonlinear.

Equilibrium Point

After a transitory time, the system usually reaches one of the equilibrium points where it will remain for all future time. Analytically, for a continuous-time dynamical system, the equilibrium points are found by assuming a constant input (i.e., the average duty cycle of the signal to transmit, $\bar{\eta}$) and by imposing $\dot{V}_c(t) = 0$. Note that the equilibrium point should be a positive value. A negative equilibrium point, in fact, implies an inversion of the polarization of the voltage across the ultra-nanocapacitor, meaning that the load drains more current than the one generated by the harvesting process. Indeed, the only acceptable equilibrium point for the considered system is:

$$V_\infty = \frac{-1 + \sqrt{1 + 2\bar{\eta}v_n g R_n C_n}}{\bar{\eta} g R_n C_n}. \quad (2.26)$$

Acceptable Value for the Proportional Gain

Besides the initial assumption on the proportional gain (i.e., $g > 0$), other technological constraints should be considered in order to evaluate the range of its acceptable values.

First, the equilibrium point in (2.26) must assume real values. Thus, the squared root and the denominator are set greater and different from zero, respectively:

$$1 + 2\bar{\eta}v_n g R_n C_n \geq 0 \text{ and } \bar{\eta} g R_n C_n \neq 0. \quad (2.27)$$

The analytical result of (2.27) states that $g \geq -1/2\bar{\eta}v_n R_n C_n$ and $g \neq 0$. Therefore, considering the initial assumption on the proportional gain (i.e., $g > 0$), this first condition is always verified.

Second, as highlighted in the derivation of the equilibrium point, it cannot be a negative value (i.e., $V_\infty > 0$). This condition is always verified when $g > 0$.

Third, the equilibrium point cannot exceed the source voltage, v_n , that is $V_\infty \leq v_n$. Accordingly:

$$V_\infty = \frac{-1 + \sqrt{1 + 2\bar{\eta}v_n g R_n C_n}}{\bar{\eta} g R_n C_n} \leq v_n. \quad (2.28)$$

Also in this case, this condition is always satisfied when $g > 0$.

Finally, the fourth constraint states that the load current $i_l(t)$ and, in turns, the amount of consumed energy at the equilibrium, E_c , computed by the closed-loop control scheme should ensure the transmission of one packet entirely composed by 1-bits guaranteeing the target Shannon capacity level: $E_c = i_l(t)V_c(t)\lambda^{-1}|_{V_\infty, \bar{\eta}} \geq E_{min}$, where $E_{min} = ME_p$. Indeed, given that $i_l(t) = gC_n\eta(t)V_c(t)^2/2$, it comes that:

$$E_c = \frac{C_n \bar{\eta} g V_\infty^3}{2\lambda} \geq E_{min}. \quad (2.29)$$

Analytically, (2.29) is verified if $-\frac{\sqrt{(v_n \lambda^{-1}(3E_{min}R_n - v_n^2 \lambda^{-1}))^2 - 4E_{min}^3 \lambda^{-1} R_n^3}}{E_{min}^2 \bar{\eta} C_n R_n^3} - \frac{v_n \lambda^{-1}(3E_{min}R_n - v_n^2 \lambda^{-1})}{E_{min}^2 \bar{\eta} C_n R_n^3} \leq g \leq \frac{\sqrt{(v_n \lambda^{-1}(3E_{min}R_n - v_n^2 \lambda^{-1}))^2 - 4E_{min}^3 \lambda^{-1} R_n^3}}{E_{min}^2 \bar{\eta} C_n R_n^3} - \frac{v_n \lambda^{-1}(3E_{min}R_n - v_n^2 \lambda^{-1})}{E_{min}^2 \bar{\eta} C_n R_n^3}$.

To sum up, among all the studied conditions, the fourth constraint determines both the upper and the lower bounds to the acceptable range of values of g .

Stability Analysis

The state equation in (2.25) can be linearized around the equilibrium point, V_∞ , by using the Taylor series: $\dot{V}_c(t) = f(V_c(t), \eta(t)) \approx f(V_\infty, \bar{\eta}) + \nabla f(V_\infty, \bar{\eta}) \cdot [\mathcal{V}_c(t) \quad \mathcal{D}(t)]^T$, where $f(V_\infty, \bar{\eta}) = 0$ by definition, $\mathcal{V}_c(t) = V_c(t) - V_\infty$ and $\mathcal{D}(t) = \eta(t) - \bar{\eta}$. Considering $\mathcal{V}_c(t)$ as the new state variable, the linearized state equation can be written as:

$$\begin{aligned} \dot{\mathcal{V}}_c(t) &= \left. \frac{\partial f(V_c(t), \eta(t))}{\partial V_c(t)} \right|_{V_\infty, \bar{\eta}} \mathcal{V}_c(t) + \left. \frac{\partial f(V_c(t), \eta(t))}{\partial \eta(t)} \right|_{V_\infty, \bar{\eta}} \mathcal{D}(t) = \\ &= \left(-\frac{1}{R_n C_n} - \bar{\eta} V_\infty g \right) \mathcal{V}_c(t) - \frac{g V_\infty^2}{2} \mathcal{D}(t). \end{aligned} \quad (2.30)$$

TABLE 2.2: Summary of simulation parameters.

Parameters	Values	References
T_p	100 fs	[94]
v_n	0.42 V	[85], [94]
C_n	9 nF	[94], [96], [114]
h_n	6 pC	[94], [96], [114]
t_n	1 s	[85], [94]
σ	0.15	[178]
f	[0.5 THz - 1.5 THz]	[178]
M	40 bit - 100 bit	[94], [96]
λ	10^{-2} frames/s - 10^{-3} frames/s - 10^{-4} frames/s	
d	3 mm - 4 mm - 5 mm	[94], [178]
\mathcal{C}	1 Mbps	[117]

The asymptotic stability around the equilibrium point of the linearized system in (2.30) is studied by posing the coefficient of $\mathcal{V}_c(t)$ less than 0 [181], that is: $-1/(R_n C_n) - \bar{\eta} V_\infty g < 0$. By substituting (2.26) in this inequality, it comes $-\sqrt{1 + 2\bar{\eta} v_n g R_n C_n} / R_n C_n < 0$ which is always verified. Therefore, considering the initial assumption on the proportional gain (i.e., $g > 0$), it comes that the system having the state equation defined in (2.25) is asymptotically stable around V_∞ for any $g > 0$.

2.2.3 Numerical Results

The following numerical analysis aims at evaluating the behavior of the investigated feedback control scheme in conceivable biomedical scenarios, while considering different communication distances, frame sizes, and message generation statistics. The results are obtained through Matlab scripts, modeling the system described in Section 2.2.1 and 2.2.2.

Regarding the harvesting process, the proposed study considers the human heartbeat as energy source. According to [85], [94], the time duration of the harvesting cycle and the generator voltage are equal to 1 s and 0.42 V, respectively. Given that the size of both piezoelectric nanogenerator and ultra-nanocapacitor strongly affect the capacitance of the ultra-nanocapacitor, C_n , and the amount of harvested energy per cycle, h_n , [94], [96], [114], when these sizes are equal to $1000 \mu\text{m}^2$, reasonable values for C_n and h_n are 9 nF and 6 pC, respectively. The source resistor is set to $R_n = \frac{v_n t_n}{h_n}$ [94]. Starting from the propagation model presented in [178], the standard deviation of the pulse is set to $\sigma = 0.15$ and the communication frequency spans from 0.5 THz to 1.5 THz. To evaluate the impact of application settings on the system performance, the proposed analysis considers two frame sizes, that are $M = 40$ bit [96] and $M = 100$ bit [94], and an average number of frames per second, spanning from 10^{-2} frames/s to 10^{-4} frames/s. The values of system parameters used throughout the numerical evaluation are summarized in Table 2.2.

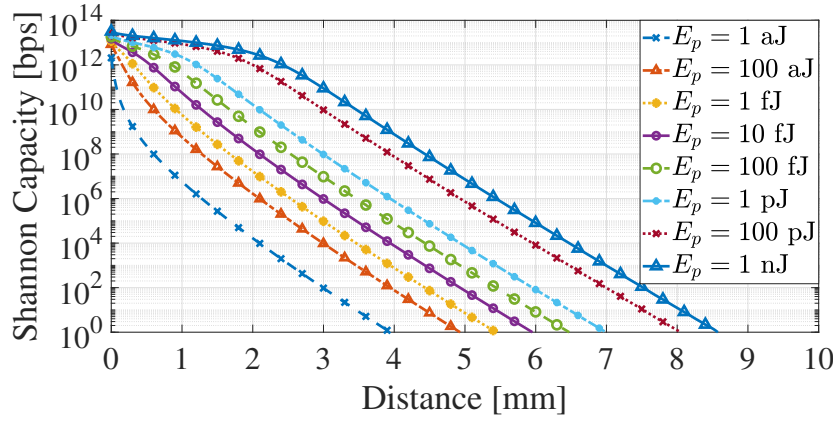


FIGURE 2.18: Upper bound of the channel capacity.

TABLE 2.3: List of the minimum and maximum acceptable proportional gain values.

		$d = 3 \text{ mm}$		$d = 4 \text{ mm}$		$d = 5 \text{ mm}$	
		$M = 40$ bit	$M = 100$ bit	$M = 40$ bit	$M = 100$ bit	$M = 40$ bit	$M = 100$ bit
$\lambda = 10^{-2}$ frames/s	$g_{min} [\text{V}^{-1}\text{s}^{-1}]$	6.03×10^8	6.07×10^8	1.16×10^{11}	unfeasible	unfeasible	unfeasible
	$g_{max} [\text{V}^{-1}\text{s}^{-1}]$	1.5×10^{17}	9.48×10^{15}	7.74×10^{12}	unfeasible	unfeasible	unfeasible
$\lambda = 10^{-3}$ frames/s	$g_{min} [\text{V}^{-1}\text{s}^{-1}]$	6×10^8	6×10^8	6.3×10^{10}	6.8×10^{10}	unfeasible	unfeasible
	$g_{max} [\text{V}^{-1}\text{s}^{-1}]$	1.5×10^{20}	9.6×10^{18}	1.43×10^{16}	8.46×10^{14}	unfeasible	unfeasible
$\lambda = 10^{-4}$ frames/s	$g_{min} [\text{V}^{-1}\text{s}^{-1}]$	5.94×10^8	5.99×10^8	6.03×10^{10}	6.07×10^{10}	1.16×10^{13}	unfeasible
	$g_{max} [\text{V}^{-1}\text{s}^{-1}]$	1.5×10^{23}	9.6×10^{21}	1.5×10^{19}	9.5×10^{17}	7.74×10^{14}	unfeasible

Figure 2.18 shows the upper bound of the channel capacity obtained according to (2.24) as a function of the communication distance and the pulse energy. Considering the target Shannon capacity equal to 1 Mbps, different communication distances equal to $d = 3 \text{ mm}$, $d = 4 \text{ mm}$, and $d = 5 \text{ mm}$ can be reached by setting the minimum required energy per pulse to $E_{min} = 10 \text{ fJ}$, $E_{min} = 1 \text{ pJ}$, and $E_{min} = 100 \text{ pJ}$, respectively. These quantities are in line with the current state of the art [94], [117], [182].

Given the constraints presented in Section 2.2.2, Table 2.3 reports the range of acceptable values for the proportional gain considering the aforementioned parameter settings. It is important to note that the range of acceptable g drastically reduces with the frame size, the communication distance, and the average number of frames per second. Moreover, the configuration with communication distance equal to 4 mm, 100 bit per frame, and $\lambda = 10^{-2}$ frames/s has not acceptable proportional gain values and it is unfeasible. As well, increasing of the communication distance to 5 mm makes unfeasible all the configurations, except the one for $M = 40$ bit and $\lambda = 10^{-2}$ frames/s. For the following analysis, only the communication distances equal to 3 mm and 4 mm are taken as example and a common intermediate value of g (i.e., $g_{int} = 7.74 \times 10^{11} \text{ V}^{-1}\text{s}^{-1}$) is chosen starting from the resulting acceptable ranges.

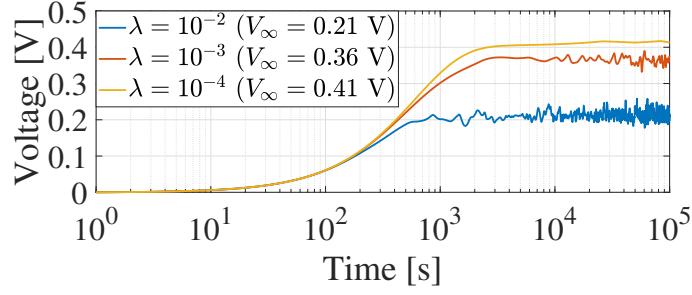
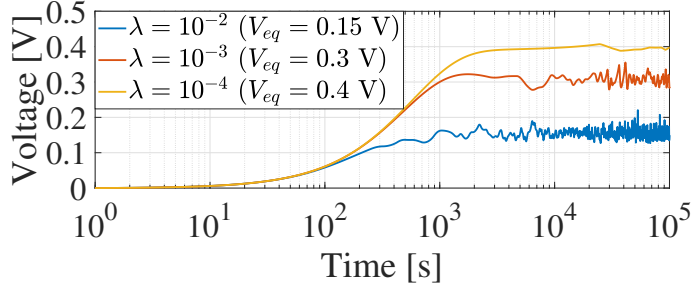
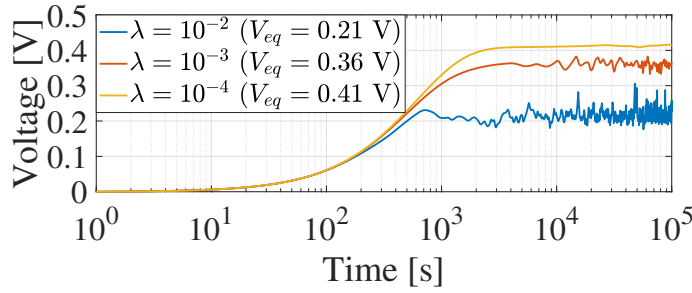
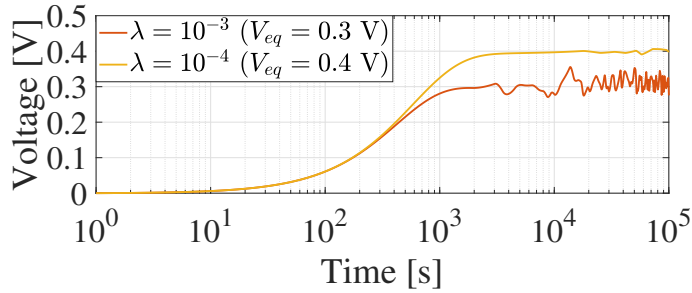
(A) $M = 40$ bit, $d = 3$ mm(B) $M = 100$ bit, $d = 3$ mm(C) $M = 40$ bit, $d = 4$ mm(D) $M = 100$ bit, $d = 4$ mmFIGURE 2.19: Variation of the state variable, $V_c(t)$, in the time domain.

Figure 2.19 depicts the variation of voltage across the ultra-nanocapacitor, $V_c(t)$, in the time domain as a function of the communication distance, d , the frame size, M , and the average number of frames per second, λ . Globally, the equilibrium point, V_∞ , decreases when λ increases. In fact, given the frame size M and the distance between transmitter and receiver d , a higher λ implies a lower time interval between consecutive message generations. This way, the system has less time to retrieve energy, leading to a lower energy budget and a lower equilibrium point. At the same

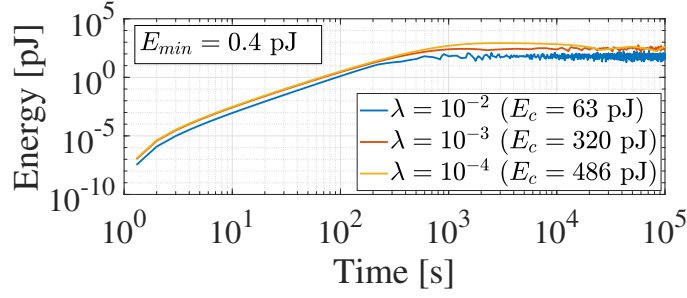
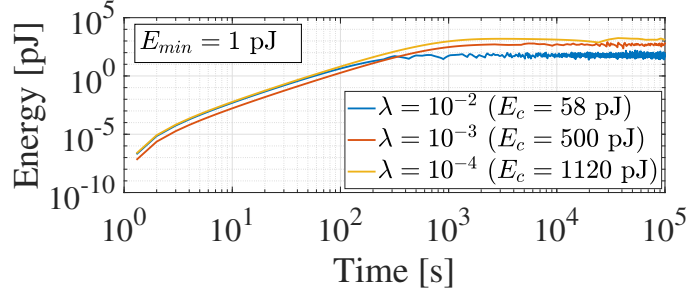
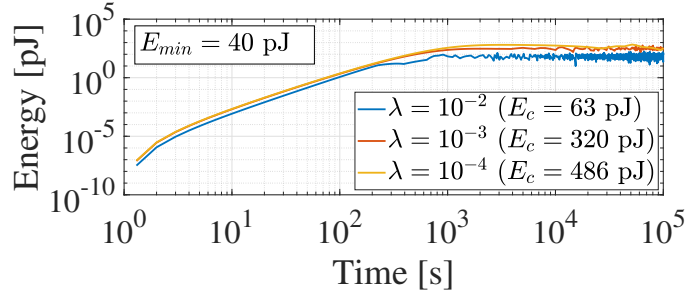
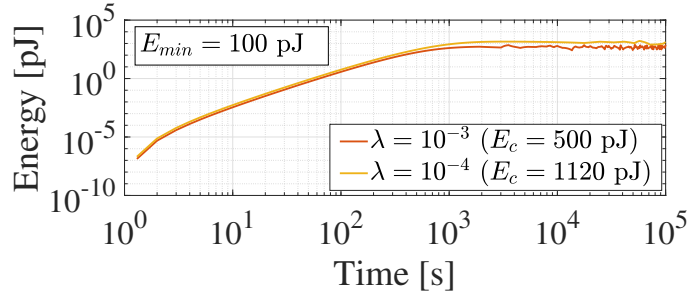
(A) $M = 40$ bit, $d = 3$ mm(B) $M = 100$ bit, $d = 3$ mm(C) $M = 40$ bit, $d = 4$ mm(D) $M = 100$ bit, $d = 4$ mm

FIGURE 2.20: Variation of the consumed energy in the time domain.

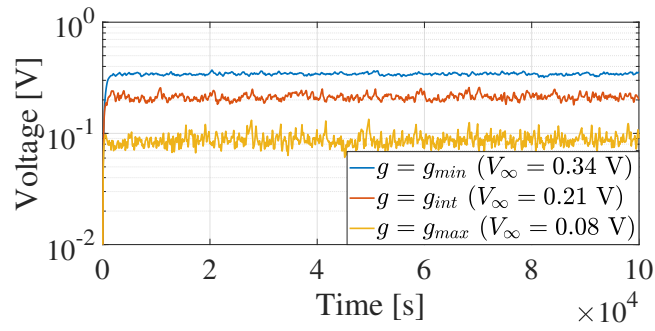
time, when the transmitter has to transmit a higher number of bit per frame, M , the energy budget decreases, thus reducing the value of the equilibrium point. It is worthwhile to note that, given the value of g , the communication distance does not affect the value of the equilibrium point. Moreover, the oscillations of the voltage value around the equilibrium point are more evident with lower value of λ due to relationship between the amount of consumed energy and the voltage at the equilibrium.

The effect of λ , d , and M on the variation of the consumed energy in the time domain is shown in Figure 2.20. First of all, the energy consumed at the equilibrium, E_c , is usually higher when M increases. Moreover, the decreasing of the average number of frames per second, λ , implies the increment of E_c . In fact, as demonstrated for the equilibrium point, higher values of λ correspond to lower energy budget. Thus, given the proportional gain g , the amount of energy consumed for the communication process is lower. Also in this case, when the g is fixed, the communication distance does not affect the value of the energy consumed at the equilibrium. On the other hand, the minimum amount of energy required to transmit a message entirely composed by 1-bits, E_{min} , obviously increases when the number of bit per frame and the communication distance increase. In any case, the amount of energy consumed at the equilibrium is higher than E_{min} .

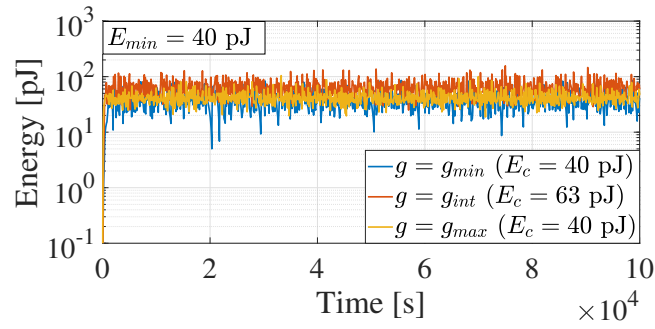
As shown in Figure 2.21 (a), the voltage across the ultra-nanocapacitor and the amount of energy consumed for the packet transmission is also affected by the proportional gain, g . Given the average number of frames per second, the number of bit per frame and the communication distance, the equilibrium point increases when g decreases. In fact, lower values of g imply a decrement of the percentage of energy consumed for transmission purposes, allowing the system to reach higher equilibrium point. Combining the voltage across the ultra-nanocapacitor at the equilibrium and the value of the proportional gain, indeed, the maximum amount of energy is consumed when an intermediate value of g is used (see Figure 2.21 (b)).

2.2.4 Final Considerations

This Section investigated a power control scheme for a nano-device fed by a piezoelectric nanogenerator and willing to communicate in human tissues through wireless communication in the terahertz band. After deriving the state equation of the resulting nonlinear system, the study of technological constraints and asymptotic stability provided the suitable range of values for the proportional gain. Finally, numerical examples showed the behavior of the proposed control approach in biomedical conceivable scenarios. This study demonstrated that the equilibrium point decreases when the inter-arrival message time decreases and the frame size increases, the resulting energy consumed at the equilibrium usually increases when the number of bit per frame and the inter-arrival message time increase, the increasing of the proportional gain implies the decreasing of the equilibrium point, and the maximum energy consumption is obtained when intermediate values of the proportional gain are used.



(A)



(B)

FIGURE 2.21: Variation of (a) the state variable and (b) the consumed energy in the time domain during the transmission of a sequence of packets by considering three different acceptable values of g , $\lambda = 10^{-2}$ frames/s, $M = 40$ bit, and $d = 4$ mm.

Chapter 3

Feedback Control Approaches in Diffusion-Based Molecular Communications

Differently from terahertz band communications, the DMC paradigm promises to enable data exchange among bio-inspired nanodevices by encoding information messages with bursts of biochemical particles, which diffuse into the medium without requiring any biological infrastructure [3], [16], [183]. Also in this context, nano-devices can leverage nano-batteries of limited capacity, while consuming non-negligible energy for the generation, the release, and the reception of molecules [39], [79]. The introduction of energy harvesting mechanisms, hence, is fundamental for achieving long-lasting communications also in DMC scenarios [16]. As deeply discussed in Chapter 1, the molecule harvesting technique [101]–[105] and energy harvesting mechanisms at the nanoscale exploiting mechanical and chemical sources [110], [112] emerged as possible approaches to solve this issue.

Nevertheless, the joint integration of energy-harvesting mechanisms that leverage piezoelectric nanogenerators and energy-aware transmission scheme for DMCs still remains an unexplored research topic. To bridge this gap, this Chapter will propose a feedback control approach for dynamically adapting the transmission power (i.e., the number of emitted molecules) in a DMC system. Specifically: 1) by inheriting from the work in [94], the harvesting process is modeled as an ideal voltage source in series with a resistor and a ultra-nanocapacitor; 2) the discharging process is modeled through a current generator in parallel with the aforementioned ultra-nanocapacitor; 3) the load current is dynamically tuned through a proportional controller in a closed-loop control scheme by simultaneously considering harvesting and discharging processes. First, the considered system model, including transmission, propagation, reception, harvesting, and discharging processes is discussed. Then, the resulting control system is described by considering, first, a continuous time nonlinear state equation and, then, a discrete time nonlinear state equation. The behavior of both control systems is finally evaluated in conceivable scenarios by considering different configuration parameters.

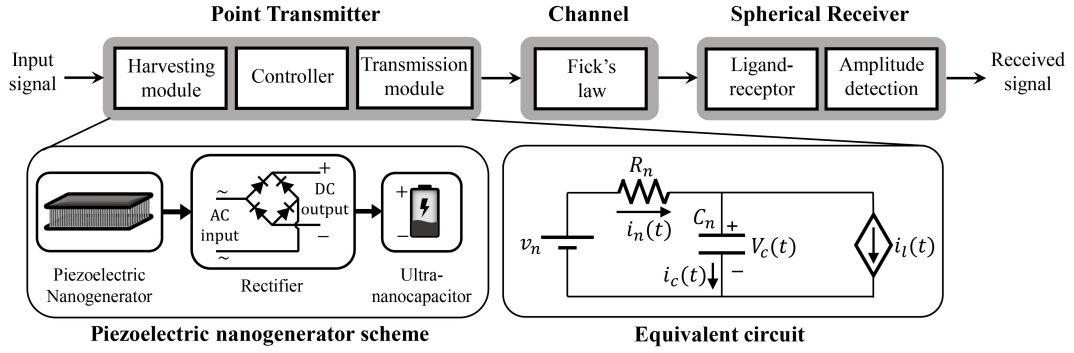


FIGURE 3.1: The considered system model for transmission, propagation, and reception processes.

3.1 The System Model

The molecular communication system considered herein includes a point transmitter fed by a piezoelectric nanogenerator, an aqueous propagation medium where molecules freely diffuse, and a spherical receiver equipped with homogeneously distributed receptors (see Figure 3.1). Transmitter and receiver are supposed to be synchronized, according to one of the mechanisms already proposed in the literature [184], [185]. Under these assumptions, this Section aims at properly modeling the transmission, the propagation, and the reception processes, along with the harvesting and discharging processes. Table 3.1 reports the main analytical symbols.

3.1.1 Transmission Process

The transmitter emits N bits long frames by using the OOK modulation. Each bit lasts T_s . As shown in Figure 3.2, instead, the time interval T_b required to release a burst of molecules is much smaller than the symbol duration: $T_b \ll T_s$. By assuming a constant bit rate source, the time interval between the generation of two consecutive frames is defined as $T_f = NT_s + T_i$, where T_i is the idle time between the end of a frame transmission and the beginning of the next frame. Let t_k be the time instant at the beginning of the k -th frame, that is $T_f = t_{k+1} - t_k$. During the k -th frame, a total amount of M_k molecules is released. The duty cycle of the signal to transmit during the k -th frame, $\eta(k)$, it represents the ratio between the amount of time spent to release the bursts of molecules encoding the set of bits 1 in the frame and the total frame duration. Given the occurrence probability of bit 1, ω , its average value, $\bar{\eta}$, and variance, $\sigma_{\bar{\eta}}^2$, are equal to:

$$\bar{\eta} = \frac{\omega NT_b}{NT_s + T_i}, \quad (3.1)$$

$$\sigma_{\bar{\eta}}^2 = \frac{\omega^2 NT_b^2}{(NT_s + T_i)^2}. \quad (3.2)$$

TABLE 3.1: List of the main analytical symbols.

Symbols	Descriptions
T_f	Time interval between the generation of two consecutive frames
N	Frame size
d	Communication distance
ω	Occurrence probability of bit 1
v_n	Generator voltage
R_n	Resistance of circuit modeling the harvesting process
C_n	Capacitance of the ultra-nanocapacitor
$i_n(t)$	Generator current
$i_c(t)$	Current through the ultra-nanocapacitor
$i_l(t)$	Load current
h_n	Harvested energy per cycle
t_n	Duration of the harvesting cycle
η	Transmission signal duty cycle
$\bar{\eta}$	Average transmission signal duty cycle
q	Quantization noise
\bar{q}	Average quantization noise
L	Number of quantization levels
Δ_q	Quantization step size
V_c	Voltage across the ultra-nanocapacitor
E	Available energy within the ultra-nanocapacitor
p	Transmission power per frame
g	Proportional gain of the controller
V_∞	Equilibrium point
ξ	Discharging conversion rate
ϕ_{min}	Minimum frame transmission energy
ϕ_{max}	Maximum frame transmission energy
e	Energy consumed for the communication process
$\sigma_{V_c}^2$	Variance of the voltage across the ultra-nanocapacitor
σ_q^2	Variance of the quantization noise
σ_η^2	Variance of the transmission signal duty cycle
τ	Time constant of the linearized system

3.1.2 Propagation Process

The considered propagation channel follows a typical DMC system, where the emitted molecules freely diffuse in a fluid medium and create differences in particle concentration detected at the receiver side. Since the concentration of emitted particles typically is much lower than the medium particle concentration, the molecules displacement is modeled by a Brownian motion, according to which information particles diffuse independently from each other and their motion is affected by the diffusion coefficient D . Under these assumption, considering a burst of m released molecules, the molecules concentration at distance d and time t is derived by the Fick's law of diffusion [183], that is:

$$c(d, t) = \frac{m}{(4\pi Dt)^{\frac{3}{2}}} e^{-\frac{d^2}{4Dt}} \quad (3.3)$$

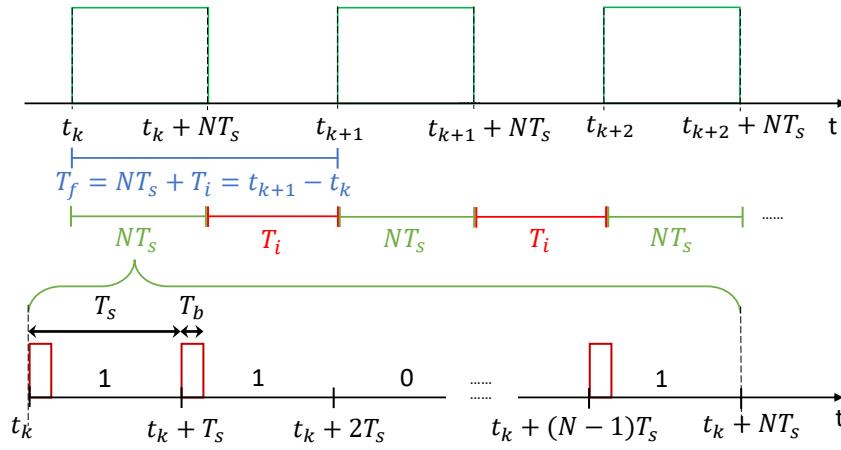


FIGURE 3.2: The considered transmission scheme.

The concentration of molecules reaching the receiver is affected by the diffusion noise and inter-symbol interference [68]. The former, $n_d(d, t)$, is due to collisions of information molecules with each other and with the fluid particles in the propagation medium. It can be modeled as an additive white Gaussian noise with zero mean and variance depending on the measured signal [186]. The latter, $n_I(d, t)$, instead, considers the molecular concentration related to the previously transmitted symbols. Indeed, the actual concentration of molecules reaching the receiver side at distance d and time t is equal to:

$$c_r(d, t) = c(d, t) + n_d(d, t) + n_I(d, t). \quad (3.4)$$

3.1.3 Reception Process

According to the ligand-receptor reaction [68], the variation of the number of molecules really captured by the receiver, $z_r(d, t)$, is given by:

$$\frac{dz_r(d, t)}{dt} = k_f r c_r(d, t) - k_f c_r(d, t) z_r(d, t) - k_r z_r(d, t), \quad (3.5)$$

where r is the number of receptors, k_f is the forward reaction rate (with a unit of measurement of m^3/s), k_r is the reverse reaction rate (with a unit of measurement of s^{-1}). The signal is sampled in order to detect the maximum number of molecules received in each time slot and it is compared with a given threshold, Θ . If the measured signal is higher than the aforementioned threshold, the receiver assumes that the received bit is equal to 1, otherwise the symbol is decoded as 0.

3.1.4 Harvesting and Discharging Processes

The transmitter hosts a piezoelectric nanogenerator, harvesting energy through an array of ZnO nanowires excited by vibrations of the surrounding environment (e.g.,

the human heartbeat in in-vivo applications) [85], [86], [88]–[91]. The generated alternating current signal is converted into a direct current source by means of a rectifier element. The available energy is finally stored in an ultra-nanocapacitor and consumed during the transmission process [94], [96], [99], [100]. The equivalent circuit in Figure 3.1 models the harvesting and the discharging processes. The harvesting process is modeled through an ideal voltage source, v_n , which generates a current, $i_n(t)$, in series with a resistor, R_n [94]. The voltage generator reproduces the harvesting source providing an amount of electric charge h_n every cycle time of t_n seconds. The value of h_n considers the loss due to the conversion between mechanical and electrical energy [94]. The amount of energy harvested by the surrounding environment is stored in an ultra-nanocapacitor with a capacitance C_n . The voltage across the ultra-nanocapacitor and the current passing through it are denoted with $V_c(t)$ and $i_c(t)$, respectively. The discharging process is modeled with a current source with a load current $i_l(t)$ in parallel with the ultra-nanocapacitor. In this context, the electrical energy stored in the ultra-nanocapacitor is converted into chemical energy through an electrochemical process [10], [187]. Then, the obtained chemical energy is used to generate manage, and release information molecules [39], [79]. The conversion from electrical energy to molecules leads to a further energy loss described by a conversion rate ξ [10], [187]. Considering basic eukaryotic cells as perfect models for bio-inspired nanodevices [39], the amount of energy required to generate and release a burst of molecules is assumed to be comparable with respect to the one consumed by pure biological systems using DMC [79].

The distance between transmitter and receiver and the number of emitted molecules influence the system performance [37]. Specifically, high communication distances can be reached by increasing the number of emitted molecules. Thus, it is necessary to define a lower bound of the number of releasable molecules per bit, m_{min} , that ensures the communication between transmitter and receiver. At the same time, however, a high number of molecules emitted by the transmitter may intensify the impact of inter-symbol interference and diffusion noise, thus impairing the overall communication. Accordingly, an upper bound of the number of releasable molecules per bit, $m_{max} > m_{min}$, is introduced to solve this issue. Given m_{min} , m_{max} , and the frame size, it is possible to define the minimum (i.e., ϕ_{min}) and the maximum (i.e., ϕ_{max}) amount of energy required to transmit a frame.

3.2 The Conceived Continuous Time Control System

First, it is considered a transmitter nano-device which delivers long sequence of bits according to the OOK modulation scheme [37]. Specifically, it is supposed to dynamically tune the instantaneous transmission power (i.e., the number of emitted molecules) for every bit, that is $N = 1$, by simultaneously considering harvesting and discharging processes. The resulting duty cycle of the transmission signal, η , represents the ratio between the amount of time spent to release a burst of molecules

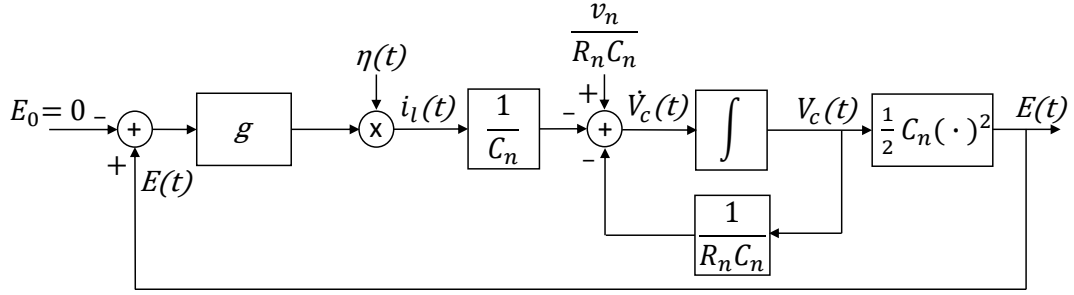


FIGURE 3.3: The conceived continuous closed-loop control scheme.

and the symbol duration. Assuming a probability of occurrence of bit 1 equal to ω and posing $T_i = 0$ in (3.1), the average duty cycle is equal to $\bar{\eta} = \omega T_b / T_s$. Considering the harvesting and discharging processes described in 3.1.4, the power transmission (i.e., the number of molecules releasable in a time unit) can be simply derived by considering the load current, $i_l(t)$, the voltage across the ultra-nanocapacitor, $V_c(t)$, and the conversion rate ξ :

$$p = \xi i_l(t) V_c(t). \quad (3.6)$$

Specifically, the methodology formulated in this Section supposes to tune the instantaneous load current $i_l(t)$ with a proportional controller in a closed-loop control scheme. The system is analytically modeled by considering the voltage across the ultra-nanocapacitor, $V_c(t)$, as the state variable. The resulting feedback control approach is depicted in Figure 3.3. With the aim of ensuring a positive energy consumption during the transmission process, the control law is designed in order to obtain a positive value of $i_l(t)$. To this end, two important assumptions are introduced: the proportional gain of the controller, g , can only assume positive values (i.e., $g > 0$) and the energy budget available at the ultra-nanocapacitor, E , is considered as the feedback variable. At the same time, in order to obtain an instantaneous load current $i_l(t)$ proportionally to the available energy budget, a null set point, i.e., $E_0 = 0$, is considered. Since $E = \frac{1}{2} C_n V_c(t)^2$, the resulting closed-loop control scheme is nonlinear.

To sum up, harvesting and discharging processes lead to a variation of the state variable in the time domain, $\dot{V}_c(t)$, described through a state equation.

Theorem 1. *The state equation describing the variation of the voltage across the ultra-nanocapacitor of the considered system is:*

$$\dot{V}_c(t) = \frac{v_n}{R_n C_n} - \frac{V_c(t)}{R_n C_n} - \frac{g \eta(t) V_c(t)^2}{2}. \quad (3.7)$$

Proof. With reference to the equivalent circuit depicted in Figure 3.1, the Kirchhoff laws state that:

$$v_n = R_n i_n(t) + V_c(t) = R_n i_c(t) + R_n i_l(t) + V_c(t). \quad (3.8)$$

As well known, the variation of the voltage across the ultra-nanocapacitor depends on the current through the capacitor $i_c(t)$ and its capacitance C_n , that is $\dot{V}_c(t) = i_c(t)/C_n$. Therefore, $i_c(t)$ can be written as:

$$i_c(t) = \dot{V}_c(t)C_n. \quad (3.9)$$

Due to the devised control approach, the load current $i_l(t)$ is proportional to the amount of available energy, E , and the duty cycle of the signal to transmit, $\eta(t)$:

$$i_l(t) = gE\eta(t) = \frac{gC_n\eta(t)V_c(t)^2}{2}. \quad (3.10)$$

Now, substituting (3.9) and (3.10) in (3.8), it holds:

$$v_n = R_nC_n\dot{V}_c(t) + R_n\frac{gC_n\eta(t)V_c(t)^2}{2} + V_c(t). \quad (3.11)$$

After a bit of algebra, it is possible to finalize the proof. \square

3.2.1 Stability Analysis

The stability of the considered continuous-time nonlinear system is now evaluated around the equilibrium point.

Theorem 2. *Given the continuous-time nonlinear system modeled in Section 3.2, a valid equilibrium point for the considered system is:*

$$V_\infty = \frac{-1 + \sqrt{1 + 2\bar{\eta}v_n g R_n C_n}}{\bar{\eta} g R_n C_n}. \quad (3.12)$$

Proof. For a continuous-time system, the equilibrium points can be found by assuming a constant input and by imposing $\dot{V}_c(t) = 0$. The constant input is set to the average duty cycle of the signal to transmit, i.e., $\bar{\eta}$. Therefore, by posing $V_c(t) = V_\infty$ and $\eta(t) = \bar{\eta}$ in (3.7), equilibrium points can be found by solving the following second-order equation:

$$\frac{g\bar{\eta}}{2}V_\infty^2 + \frac{1}{R_n C_n}V_\infty - \frac{v_n}{R_n C_n} = 0. \quad (3.13)$$

This equation has two roots. The first one is equal to:

$$V_{\infty 1} = \frac{-1 - \sqrt{1 + 2\bar{\eta}v_n g R_n C_n}}{\bar{\eta} g R_n C_n}. \quad (3.14)$$

Since $g > 0$, $V_{\infty 1}$ is always negative. By inverting the polarization of the voltage across the ultra-nanocapacitor, the Kirchhoff first law applied to the circuit in Figure 3.1 stands that $i_n(t) = -i_c(t) + i_l(t)$. In other words, $i_l(t) = i_c(t) + i_n(t) > i_n(t)$. This means that, at the equilibrium, the load drains more current than the one generated

by the harvesting process. Therefore, $V_{\infty 1}$ is not an admissible equilibrium point. Conversely, the second root, that is:

$$V_{\infty 2} = \frac{-1 + \sqrt{1 + 2\bar{\eta}v_n g R_n C_n}}{\bar{\eta}g R_n C_n}, \quad (3.15)$$

provides an acceptable equilibrium point. This concludes the proof. \square

As initially anticipated, the control law has been designed by imposing $g > 0$. Nevertheless, other considerations should be done for obtaining the suitable range of values of the proportional gain g .

Theorem 3. *The acceptable range of values of the proportional control gain g is:*

$$\frac{-A - \sqrt{A^2 - B}}{D} \leq g \leq \frac{-A + \sqrt{A^2 - B}}{D} \quad (3.16)$$

where $A = v_n \zeta T_s (3\phi_{\min} R_n - v_n^2 \zeta T_s)$, $B = 4\phi_{\min}^3 \zeta T_s R_n^3$, and $D = \phi_{\min}^2 \bar{\eta} C_n R_n^3$.

Proof. The proof is achieved by considering four conditions.

First, the equilibrium point obtained by Theorem 2 must be defined in the real domain. Accordingly, the squared root and the denominator cannot assume negative and zero values, respectively, that is:

$$1 + 2\bar{\eta}v_n g R_n C_n \geq 0 \text{ and } \bar{\eta}g R_n C_n \neq 0. \quad (3.17)$$

Analytically, (3.17) is satisfied if $g \geq -\frac{1}{2\bar{\eta}v_n R_n C_n}$ and $g \neq 0$. Therefore, considering the initial assumption on the proportional gain (i.e., $g > 0$), this first condition is always verified.

Second, as highlighted in the proof of Theorem 2, the equilibrium point must assume positive values (i.e., $V_{\infty} > 0$). This condition is always verified when $g > 0$.

The third condition refers to the maximum voltage across the ultra-nanocapacitor. The equilibrium point cannot exceed the source voltage, v_n , that is $V_{\infty} \leq v_n$. Analytically:

$$V_{\infty} = \frac{-1 + \sqrt{1 + 2\bar{\eta}v_n g R_n C_n}}{\bar{\eta}g R_n C_n} \leq v_n. \quad (3.18)$$

The (3.18) is verified when $g > 0$. Also in this case, the initial assumption on the proportional gain of the controller (i.e., $g > 0$) ensures that this second condition is always satisfied.

Finally, the load current $i_l(t)$ at the equilibrium provided by the closed-loop control scheme should ensure the transmission of the minimum number of molecules that guarantees the desired level of performance: $pT_s|_{V_{\infty}, \bar{\eta}} \geq \phi_{\min}$. Indeed, given (3.6) and (3.10), it holds:

$$pT_s|_{V_{\infty}, \bar{\eta}} = \frac{1}{2} \zeta C_n \bar{\eta} T_s g V_{\infty}^3 \geq \phi_{\min}. \quad (3.19)$$

Analytically, (3.19) is verified if $\frac{-A-\sqrt{A^2-B}}{D} \leq g \leq \frac{-A+\sqrt{A^2-B}}{D}$.

To sum up, considering all the analyzed conditions, the fourth constraint determines the upper and the lower bounds to the acceptable range of values of g , concluding the proof. \square

Theorem 4. *The system having a state equation described in (3.7) is asymptotically stable around V_∞ for any $g > 0$.*

Proof. The state equation in (3.7), also reported in what follows as $\dot{V}_c(t) = f(V_c(t), \eta(t))$, refers to a nonlinear system. Nevertheless, in a small neighborhood of the equilibrium point, V_∞ , the aforementioned system can be assumed to be linear. Hence, it is possible to introduce a linearization around the equilibrium point, V_∞ , by using the Taylor series:

$$\dot{V}_c(t) = f(V_c(t), \eta(t)) \approx f(V_\infty, \bar{\eta}) + \nabla f(V_\infty, \bar{\eta}) \cdot \begin{bmatrix} \Delta V_c(t) \\ \Delta \eta(t) \end{bmatrix}, \quad (3.20)$$

where $f(V_\infty, \bar{\eta}) = 0$ by definition, $\Delta V_c(t) = V_c(t) - V_\infty$ and $\Delta \eta(t) = \eta(t) - \bar{\eta}$. By considering the variable $\Delta \dot{V}_c(t)$, the linearized state equation is:

$$\begin{aligned} \Delta \dot{V}_c(t) &= \left. \frac{\partial f(V_c(t), \eta(t))}{\partial V_c(t)} \right|_{V_\infty, \bar{\eta}} \Delta V_c(t) + \left. \frac{\partial f(V_c(t), \eta(t))}{\partial \eta(t)} \right|_{V_\infty, \bar{\eta}} \Delta \eta(t) = \\ &= \left(-\frac{1}{R_n C_n} - \bar{\eta} V_\infty g \right) \Delta V_c(t) - \frac{g V_\infty^2}{2} \Delta \eta(t) = \\ &= X \Delta V_c(t) + Y \Delta \eta(t). \end{aligned} \quad (3.21)$$

Now, given the linearized state equation around the equilibrium point, the considered system is asymptotically stable if the coefficient that multiplies $\Delta V_c(t)$ in (3.21) is less than 0 [181], that is:

$$X = \left(-\frac{1}{R_n C_n} - \bar{\eta} V_\infty g \right) < 0. \quad (3.22)$$

By substituting (3.12) in (3.22), it brings to the following inequality $-\frac{\sqrt{1+2\bar{\eta}v_n g R_n C_n}}{R_n C_n} < 0$, which is always verified. Therefore, considering the initial assumption on the proportional gain (i.e., $g > 0$), the modeled system is asymptotically stable around V_∞ . \square

Theorem 4 highlights that the stability analysis around the equilibrium point does not further restrict the study presented by Theorem 3. Therefore, it is possible to conclude that the acceptable range of values of the proportional gain g given by (3.16) makes the system asymptotically stable around V_∞ .

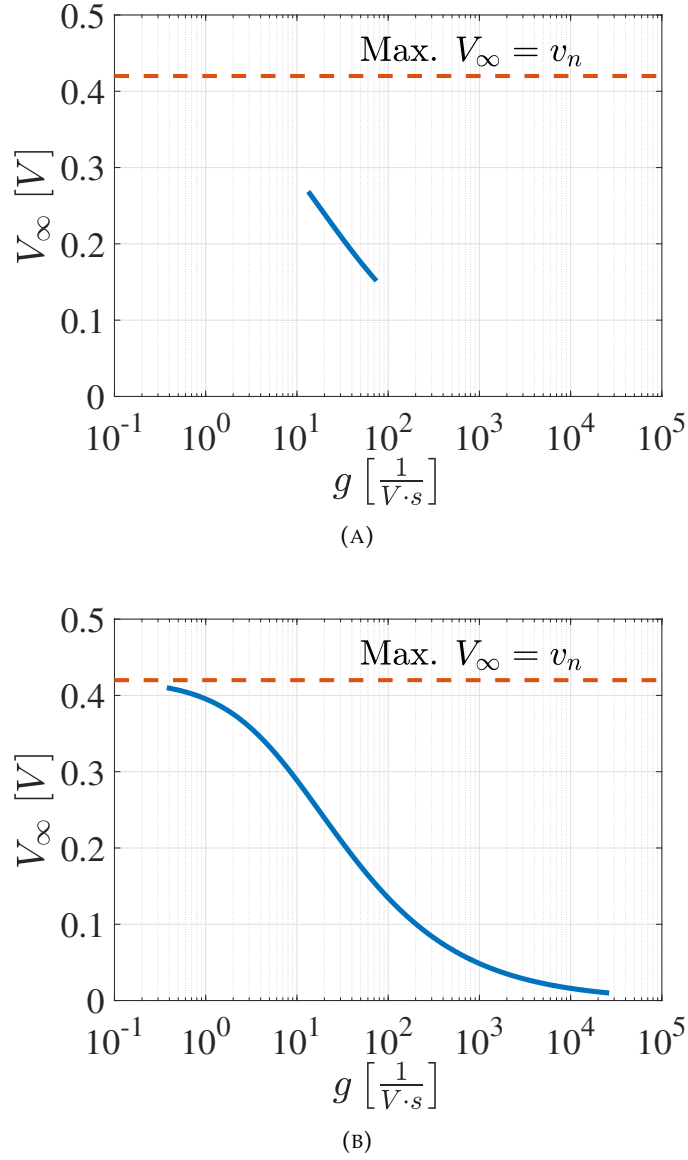


FIGURE 3.4: Equilibrium point, V_∞ , as a function of the proportional gain, g , when (a) $C_n = 0.9$ nF and $h_n = 0.6$ pC, and (b) $C_n = 9$ nF and $h_n = 6$ pC.

3.2.2 Numerical Investigations

The following numerical example intends to show the behavior of the proposed approach in conceivable scenarios. The proposed study considers a physical symbol duration $T_s = 1$ s [37]. Accordingly, T_b is set to 1 ms. Assuming a probability of occurrence of bit 1, ω , equal to 0.5, the average duty cycle is set to $\bar{\eta} = \omega \frac{T_b}{T_s} = 5 \cdot 10^{-4}$. The time duration of the harvesting cycle is set to $t_n = 1$ s. Regarding the energy harvesting mechanism, a conceivable value for the generator voltage is 0.42 V, as highlighted in [85], [94]. Furthermore, the amount of harvested charge per cycle, h_n , and the capacitance of the ultra-nanocapacitor, C_n , are directly affected by the technology used to fabricate the ultra-nanocapacitor and the size of both piezoelectric nanogenerator and ultra-nanocapacitor [94], [97], [114]. This Section considers a

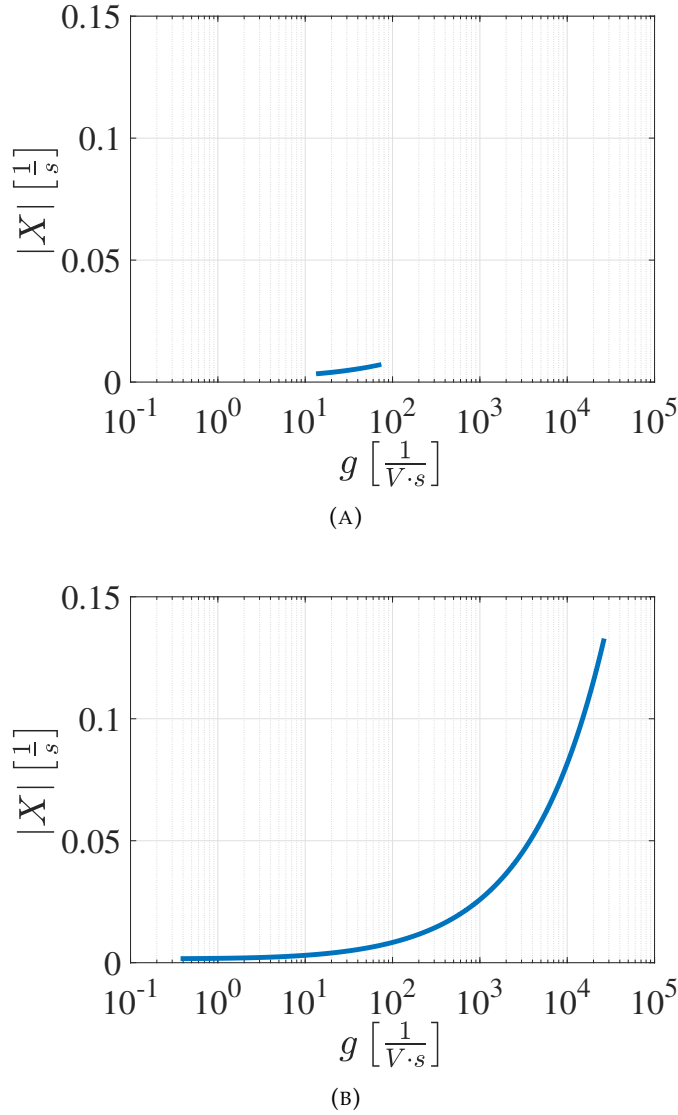


FIGURE 3.5: Modulus of the pole of the closed-loop control scheme, $|X|$, as a function of the proportional gain, g , when (a) $C_n = 0.9 \text{ nF}$ and $h_n = 0.6 \text{ pC}$, and (b) $C_n = 9 \text{ nF}$ and $h_n = 6 \text{ pC}$.

ultra-nanocapacitor based on onion-like carbon electrodes [94], [114] and a reasonable size for both piezoelectric nanogenerator and ultra-nanocapacitor ranging from $100 \mu\text{m}^2$ to $1000 \mu\text{m}^2$ [94], [97]. In the first case, $h_n = 0.6 \text{ pC}$ and $C_n = 0.9 \text{ nF}$. In the second case, $h_n = 6 \text{ pC}$ and $C_n = 9 \text{ nF}$. The source resistor is set to $R_n = \frac{v_n t_n}{h_n}$ [94]. The electrical energy stored within the ultra-nanocapacitor is supposed to be converted to chemical energy through the water electrolysis process, which presents a conversion rate equal to $\xi = 40\%$ [187]. The chemical energy is used to generate insulin molecules through the polymerization of amino acids. According to [79], the process requires the presence of raw materials (i.e., amino acids) within the nano-device and an amount of chemical energy to bind amino acids. Thus, considering $m_{\min} = 10^3$ and the model presented in [79], the minimum amount of energy required to transmit a burst of molecules encoding the bit 1 is set to $\phi_{\min} = 0.023 \text{ pJ}$.

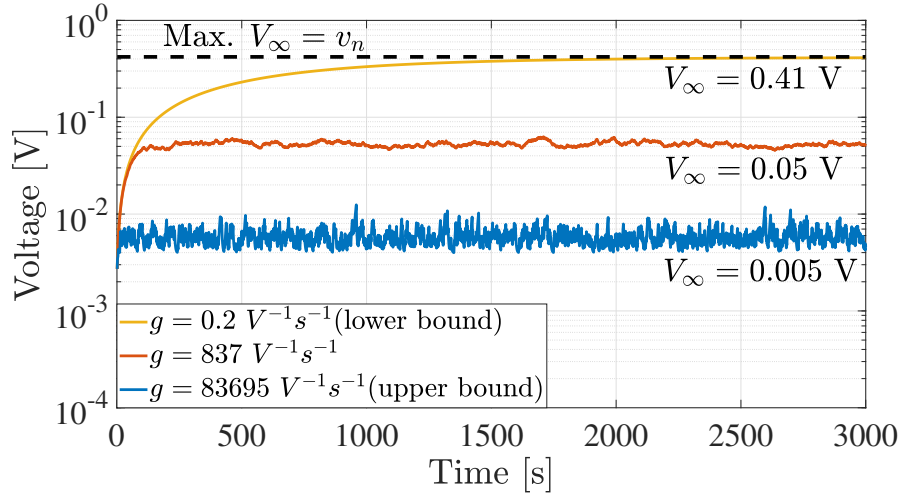


FIGURE 3.6: Variation of the state variable, $V_c(t)$, in the time domain during the transmission of a long sequence of bits, by considering three different acceptable values of g , $C_n = 9$ nF, $h_n = 6$ pC, and $v_n = 0.42$ V.

Figure 3.4 shows that the equilibrium point decreases with g . A higher value of g leads to an increment of the percentage of energy budget consumed for transmitting a single burst of molecules, while reaching lower values of the voltage across the ultra-nanocapacitor at the equilibrium point. Proposed results also demonstrate that the range of acceptable values of g is drastically limited by the dimension of both piezoelectric nanogenerator and ultra-nanocapacitor.

Figure 3.5 illustrates the effect of g on the absolute value of X , as defined in (3.22). Specifically, X corresponds to the pole of the examined closed-loop control scheme. According to the control theory, the time response of the system decreases when $|X|$ increases. Thus, a high value of g is preferable to obtain a system which rapidly returns at the equilibrium state after a perturbation of the duty cycle $\eta(t)$ of the signal to transmit. This means that the dimension of both piezoelectric nanogenerator and ultra-nanocapacitor directly affect the minimum time response of the formulated control system.

Figure 3.6 depicts the variation of the state variable, $V_c(t)$, in the time domain during the transmission of a long sequence of bits, by considering three different acceptable values of g , $C_n = 9$ nF, $h_n = 6$ pC, and $v_n = 0.42$ V. The analysis starts assuming an initial energy budget equal to ϕ_{min} . It confirms that the developed system is asymptotically stable around the equilibrium point, V_∞ . A higher value of g corresponds to a lower equilibrium point and the time required to reach the equilibrium point increases when g decreases.

3.2.3 Final Considerations

This Section proposed a feedback control approach for an energy-harvesting and diffusion-based molecular communication system, that dynamically tunes the instantaneous load current drained by the transmitter interface through a proportional

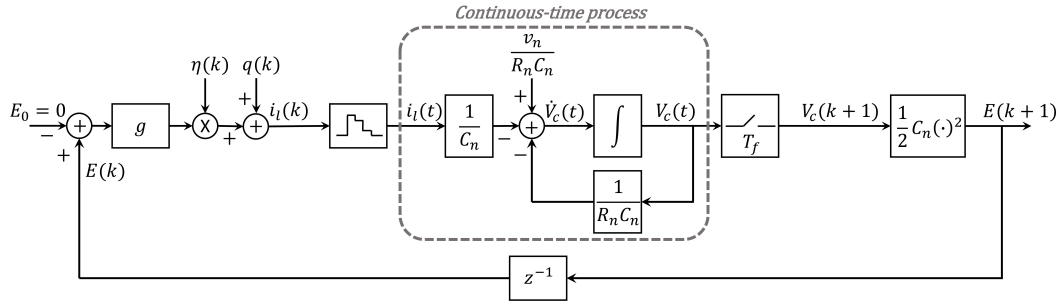


FIGURE 3.7: The conceived closed-loop control scheme.

controller. After deriving the state equation of the nonlinear system, the analysis of its stability and technological constraints provided the acceptable range of values for the proportional gain. The numerical example illustrated the behavior of the formulated approach in conceivable scenarios.

3.3 The Conceived Discrete Time Control System

The continuous-time model described in the previous Section discusses a very preliminary control scheme, where it is assumed to dynamically tune the number of molecules to transmit for every bit of information. Furthermore, it analyzes asymptotic stability only, without evaluating the impact of the proposed solution on communication performance. Starting from these premises, this Section intends to provide an important step forward in the design of a power control mechanism for DMC systems fed by piezoelectric nanogenerators. Specifically, by assuming the voltage at the ultra-nanocapacitor as the state variable of the system and the resulting energy budget as the feedback variable, the load current (thus, the transmission power) is dynamically tuned through a proportional controller in a closed-loop control scheme and on a per-frame basis.

The devised approach starts considering the equivalent circuit depicted in Figure 3.1, analytically described by the Kirchhoff's laws of current and voltage:

$$v_n = R_n i_n(t) + V_c(t) = R_n i_c(t) + R_n i_l(t) + V_c(t). \quad (3.23)$$

Since the current passing through the ultra-nanocapacitor is derived by the well-known relationship between the voltage across the ultra-nanocapacitor and its current and capacitance, that is $i_c(t) = \dot{V}_c(t)C_n$, the continuous-time process is revised as a linear first-order differential equation:

$$\dot{V}_c(t) = \frac{v_n}{R_n C_n} - \frac{V_c(t)}{R_n C_n} - \frac{i_l(t)}{C_n}. \quad (3.24)$$

The conceived feedback control scheme intends to raise or decrease the transmission power on a per-frame basis, while keeping it constant during T_f . Under these conditions, a discrete-time model for the control strategy is the natural choice,

albeit the controlled plant (i.e., the ultra-nanocapacitor) exhibits a continuous-time dynamic for the discharging and harvesting processes. Accordingly, the control system shown in Figure 3.7 embraces an inner continuous-time model (describing the instantaneous discharging process and the harvesting process) and an outer discrete-time model (outlining the per-frame based power control mechanism), while considering the voltage across the ultra-nanocapacitor as the state variable. Let $V_c(k)$ and $i_l(k)$ be the discrete value of both voltage across the ultra-nanocapacitor and load current, respectively, evaluated at the beginning of the k -th frame (i.e., when $t = t_k$). $V_c(k)$ is obtained by sampling the voltage across the ultra-nanocapacitor every T_f . A zero-order hold block is used to convert the discrete value of the load current to its continuous-time representation taken into account by the aforementioned discharging model.

The load current assumes a limited number of levels. Assuming a quantization step size Δ_q , the quantization noise, $q(k)$, can be modeled as a stochastic process with uniform distribution, zero mean, and variance equal to $\Delta_q^2/12$. Note that the quantization noise and the duty cycle of the signal to transmit are considered as external inputs to the closed-loop control scheme and are assumed as independent.

The power used to transmit the k -th frame, $p(k)$, is computed by considering the conversion rate ξ , the voltage across the ultra-nanocapacitor at the beginning of the k -th frame, $V_c(k)$, and the resulting load current, $i_l(k)$, while neglecting the amount of energy required to calculate the available energy budget:

$$p(k) = \xi V_c(k) i_l(k). \quad (3.25)$$

With the aim of ensuring a positive energy consumption during the transmission process, the control law is designed in order to obtain a positive value of $i_l(k)$. To this aim, the proportional gain of the controller, g , can only assume positive values (i.e., $g > 0$); the energy budget available at the ultra-nanocapacitor at the beginning of the k -th frame, $E(k)$, is considered as the feedback variable; and the target point is set to 0 (i.e., $E_0 = 0$). Since $E(k) = C_n V_c^2(k)/2$, the resulting closed-loop control scheme is nonlinear.

3.3.1 State Equation and Equilibrium Points

The harvesting and discharging processes cause a variation of the amount of energy available in the ultra-nanocapacitor, that can be described through a discrete-time state equation. In fact, the load current is assumed to be constant during the k -th frame, i.e., $i_l(t) = i_l(k)$ in $t_k \leq t \leq t_{k+1}$. Considering an initial condition equal to $V_c(k)$, the solution of eq. (3.24) is:

$$V_c(t) = \left(V_c(k) - v_n + i_l(k) R_n \right) e^{-\frac{1}{R_n C_n} (t - t_k)} + v_n - i_l(k) R_n. \quad (3.26)$$

Now, by considering $t = t_{k+1}$, after a bit of algebra, the value of the state variable at the beginning of the next frame is:

$$V_c(k+1) = \left(e^{-\frac{t_{k+1}-t_k}{R_n C_n}} - 1 \right) (i_l(k) R_n - v_n) + e^{-\frac{t_{k+1}-t_k}{R_n C_n}} V_c(k). \quad (3.27)$$

The load current $i_l(k)$ is given by the sum of two contributions. The former is proportional to the amount of available energy, $E(k)$, and the duty cycle of the signal to transmit, $\eta(k)$. The latter is the quantization noise $q(k)$. Therefore:

$$i_l(k) = gE(k)\eta(k) + q(k) = \frac{gC_n\eta(k)V_c^2(k)}{2} + q(k). \quad (3.28)$$

By substituting eq. (3.28) in (3.27), it is possible to obtain the state equation of the power control system in Figure 3.7:

$$V_c(k+1) = \left(e^{-\frac{T_f}{R_n C_n}} - 1 \right) \left[\left(\frac{gC_n\eta(k)V_c^2(k)}{2} + q(k) \right) R_n - v_n \right] + e^{-\frac{T_f}{R_n C_n}} V_c(k). \quad (3.29)$$

The state equation captures the behavior of the system over the time. According to the non-linear control theory [181], however, the properties of the resulting non-linear discrete-time dynamical system, including its stability, can be investigated around its equilibrium point (i.e., the value assumed by the state variable when the system is in a steady-state).

Theorem 5. Due to the nonlinear system modeled in eq. (3.29), a valid equilibrium point is:

$$V_\infty = \frac{-1 + \sqrt{1 + 4\psi v_n g}}{2\psi g} \quad (3.30)$$

where $\psi = \bar{\eta} R_n C_n / 2$ and $\bar{\eta}$, as defined above, is the average value of the duty cycle, $\eta(k)$.

Proof. The equilibrium points of a discrete-time dynamical system are derived by posing $V_c(k+1) = V_c(k) = V_\infty$ and by assuming constant inputs, that is, the average duty cycle of the signal to transmit, $\eta(k) = \bar{\eta}$, and the mean value of the quantization noise, $q(k) = \bar{q}$. Substituting these values in eq. (3.29) and considering that the quantization noise is modeled as an uniform noise with zero mean (i.e., $\bar{q} = 0$), the equilibrium points are found by solving a simple second order equation:

$$\begin{aligned} V_\infty &= \psi g \left(e^{-\Lambda} - 1 \right) V_\infty^2 + e^{-\Lambda} V_\infty + \left(1 - e^{-\Lambda} \right) (v_n - R_n \bar{q}) \Rightarrow \\ &\Rightarrow g\psi V_\infty^2 + V_\infty - v_n = 0. \end{aligned} \quad (3.31)$$

where $\psi = \bar{\eta} R_n C_n / 2$ and $\Lambda = T_f / R_n C_n$ has been introduced to simplify notation.

Now, $V_{\infty 1} = (-1 - \sqrt{1 + 4\psi v_n g}) / (2\psi g)$ and $V_{\infty 2} = (-1 + \sqrt{1 + 4\psi v_n g}) / (2\psi g)$ are the two roots of Eq. (3.31). Since the initial assumption on load current requires a positive value of the proportional gain (i.e., $g > 0$), $V_{\infty 1}$ is always negative and it

cannot be considered an acceptable equilibrium point. In fact, supposing a negative load current at the equilibrium, the polarization of the voltage across the ultranancapacitor should be inverted and the Kirchhoff's law of the current applied to the equivalent circuit in Figure 3.1 implies $i_n(t) = -i_c(t) + i_l(t)$. This means that the load drains more current than the generated one at the equilibrium (i.e., $i_l(t) = i_c(t) + i_n(t) > i_n(t)$), leading to an absurd result. Instead, the second root, $V_{\infty 2}$ provides an acceptable equilibrium point for some values of g , concluding the proof. \square

3.3.2 Analysis of the Bounds of the Proportional Gain

Besides the initial assumption on g to guarantee a positive load current (i.e., $g > 0$), other considerations on technological constraints should be done in order to obtain the acceptable range of values of the proportional gain. In fact, it is possible to demonstrate the following result.

Theorem 6. *The acceptable range of values of the proportional gain depends on the values of systems parameters as in what follows:*

$$\left\{ \begin{array}{ll} \gamma_1 \leq g \leq \gamma_4 & \text{if } (\Psi_b^2 - Y_b) < 0 \\ \gamma_1 \leq g \leq \gamma_2 \vee \gamma_3 \leq g \leq \gamma_4 & \text{if } (\Psi_b^2 - Y_b) \geq 0 \quad \text{and} \quad \gamma_1 \leq \gamma_2 \wedge \gamma_3 \leq \gamma_4 \\ \gamma_1 \leq g \leq \gamma_2 & \text{if } (\Psi_b^2 - Y_b) \geq 0 \quad \text{and} \quad \gamma_1 \leq \gamma_2 \wedge \gamma_3 > \gamma_4 \\ \gamma_3 \leq g \leq \gamma_4 & \text{if } (\Psi_b^2 - Y_b) \geq 0 \quad \text{and} \quad \gamma_1 > \gamma_2 \wedge \gamma_3 \leq \gamma_4 \\ \nexists g \in \mathbb{R} & \text{if } (\Psi_b^2 - Y_b) \geq 0 \quad \text{and} \quad \gamma_1 > \gamma_2 \wedge \gamma_3 > \gamma_4 \\ \nexists g \in \mathbb{R} & \text{if } (\Psi_a^2 - Y_a) < 0 \end{array} \right. \quad (3.32)$$

where

$$\gamma_1 = \frac{-\Psi_a - \sqrt{\Psi_a^2 - Y_a}}{\phi_{\min}^2 \chi}; \quad \gamma_2 = \frac{-\Psi_b - \sqrt{\Psi_b^2 - Y_b}}{\phi_{\max}^2 \chi}; \quad \gamma_3 = \frac{-\Psi_b + \sqrt{\Psi_b^2 - Y_b}}{\phi_{\max}^2 \chi} \quad (3.33)$$

$$\gamma_4 = \min \left(\frac{-\Psi_a + \sqrt{\Psi_a^2 - Y_a}}{\phi_{\min}^2 \chi}, \frac{C_n R_n + 2T_f}{8\bar{\eta} v_n T_f^2}, \frac{4LT_s}{R_n C_n v_n T_b (1 - e^{-\Lambda}) (2L + 1)} \right) \quad (3.34)$$

$$\Psi_a = v_n \zeta T_f (3\phi_{\min} R_n - v_n^2 \zeta T_f); \quad Y_a = 4\phi_{\min}^3 \zeta T_f R_n^3; \quad \chi = \bar{\eta} C_n R_n^3 \quad (3.35)$$

$$\Psi_b = v_n \zeta T_f (3\phi_{\max} R_n - v_n^2 \zeta T_f); \quad Y_b = 4\phi_{\max}^3 \zeta T_f R_n^3. \quad (3.36)$$

Proof. The proof is derived taking into account that the acceptable values' range for the proportional gain g of the controller jointly requires six conditions: 1) the equilibrium point must be defined in the real domain, 2) the equilibrium point cannot be higher than the source voltage v_n , 3) the amount of energy consumed for communication process at the equilibrium must be higher than the minimum energy consumption level ϕ_{min} , 4) the amount of energy consumed for communication process at the equilibrium must be lower than the maximum energy consumption level ϕ_{max} , 5) the amount of available energy at the equilibrium must be higher than the one required to transmit a frame with N consecutive bits equal to 1, and 6) the voltage across the ultra-nanocapacitor must always be a positive value. These six conditions are deeply investigated in what follows.

The first condition refers to the study of the domain of the equilibrium point function in eq. (3.31), according to which the argument of the squared root must be positive and the denominator cannot assume zeros values:

$$1 + 4\psi v_n g \geq 0 \quad \text{and} \quad 2\psi g \neq 0. \quad (3.37)$$

Analytically, this condition is verified if $g \geq -1/4\psi v_n$ and $g \neq 0$, respectively. Therefore, considering the initial assumption on the proportional gain of the controller (i.e., $g > 0$), this first condition is always satisfied.

The second condition deals with the upper bound of the voltage across the ultra-nanocapacitor, equal to the voltage provides by the generator, v_n . The voltage at the equilibrium cannot exceed the source voltage, v_n , that is $V_\infty \leq v_n$. Analytically, by considering (3.30), this condition becomes:

$$V_\infty = \frac{-1 + \sqrt{1 + 4\psi v_n g}}{2\psi g} \leq v_n \quad (3.38)$$

which is only verified for $g > 0$. Also in this case, considering the initial assumption on the proportional gain, this condition is always satisfied.

The third condition focuses on the value of the load current $i_l(k)$ provided by the closed-loop control scheme at the equilibrium. As already argued in Section 3.1.4, the amount of energy consumed for communication process at the equilibrium, $e(k)|_{V_\infty, \bar{\eta}, \bar{q}}$, should ensure the transmission of the minimum number of molecules that guarantees the desired level of performance:

$$e(k)|_{V_\infty, \bar{\eta}, \bar{q}} = p(k)T_f|_{V_\infty, \bar{\eta}, \bar{q}} \geq \phi_{min}. \quad (3.39)$$

Indeed, given (3.25) and (3.28), the third condition can be expressed as:

$$e(k)|_{V_\infty, \bar{\eta}, \bar{q}} = \frac{\xi C_n \bar{\eta} T_f g V_\infty^3}{2} \geq \phi_{min}. \quad (3.40)$$

Analytically, it is verified if $\gamma_1 \leq g \leq (-\Psi_a + \sqrt{\Psi_a^2 - Y_a})/(\phi_{min}^2 \chi)$, where parameters have been defined in (3.33)-(3.36). This inequality influences the value of γ_4

in the Theorem and the maximum considerable value for the minimum energy per frame, ϕ_{min} , by posing the argument of the squared root as $\Psi_a^2 - Y_a \geq 0$. This constraint is verified if $\phi_{min} \leq v_n^2 \xi T_f / 4R_n$. Otherwise the entire system is unfeasible.

The fourth condition considers that an excessive number of transmitted molecules drastically impairs the communication performance, as highlighted in Section 3.1. Thus, the energy consumption associated with the closed-loop control scheme should not be higher than the one needed to transmit the maximum number of molecules guaranteeing the target performance:

$$e(k)|_{V_\infty, \bar{\eta}, \bar{q}} = p(k) T_f |_{V_\infty, \bar{\eta}, \bar{q}} \leq \phi_{max}. \quad (3.41)$$

Starting from (3.25) and (3.28), the fourth condition states that:

$$e(k)|_{V_\infty, \bar{\eta}, \bar{q}} = \frac{\xi C_n \bar{\eta} T_f g V_\infty^3}{2} \leq \phi_{max}. \quad (3.42)$$

This condition is always verified if $\Psi_b^2 - Y_b < 0$. Otherwise, it is satisfied only if $g \leq \gamma_2$ or $g \geq \gamma_3$. Considering the initial assumption on the proportional gain (i.e., $g > 0$), the solution of the fourth condition is $0 \leq g \leq \gamma_2$ or $g \geq \gamma_3$.

The fifth condition assumes that the system should have, at the equilibrium, an amount of energy greater than the one needed to transmit a frame with N consecutive bits equal to 1, that is:

$$\frac{C_n V_\infty^2}{2} \geq g C_n T_f \bar{\eta} V_\infty^3. \quad (3.43)$$

Analytically, it is satisfied if $g \leq (C_n R_n + 2T_f) / 8\bar{\eta} v_n T_f^2$ and $g \neq 0$. Considering the initial assumption on the proportional gain of the controller (i.e., $g > 0$), the fifth condition is verified if $0 < g \leq (C_n R_n + 2T_f) / 8\bar{\eta} v_n T_f^2$. This constraint is useful for the calculation of γ_4 used in the Theorem.

The sixth condition states that the voltage across the ultra-nanocapacitor must always be a positive value to avoid changing of polarization: $V_c(k) \geq 0$ for all $k \in \mathbb{N}$. This is verified by means of the principle of induction. Starting from $V_c(0) = V_0 \geq 0$ and supposing that $V_c(k) \geq 0$ is true, it is possible to compute the values of g respecting the sixth condition by imposing $V_c(k+1) \geq 0$. Considering the state equation (3.29), the following inequality is introduced:

$$g \leq \frac{2e^{-\Lambda} V_c(k) + 2(1 - e^{-\Lambda})(v_n - q(k)R_n)}{C_n R_n \eta(k)(1 - e^{-\Lambda}) V_c^2(k)} = f(V_c(k), \eta(k), q(k)). \quad (3.44)$$

It is possible to evaluate the behavior of g as a function of each variable, $V_c(k)$, $\eta(k)$, and $q(k)$. Let's now consider the partial derivatives in (3.45):

$$\begin{aligned}\frac{\partial f(V_c(k), \eta(k), q(k))}{\partial \eta(k)} &= -\frac{2e^{-\Lambda}V_c(k) + 2(1 - e^{-\Lambda})(v_n - q(k)R_n)}{C_n R_n (1 - e^{-\Lambda}) V_c^2(k) \eta^2(k)} < 0, \\ \frac{\partial f(V_c(k), \eta(k), q(k))}{\partial q(k)} &= -\frac{2}{C_n \eta(k) V_c^2(k)} < 0, \\ \frac{\partial f(V_c(k), \eta(k), q(k))}{\partial V_c(k)} &= -\frac{2e^{-\Lambda}V_c(k) + 4(1 - e^{-\Lambda})(v_n - q(k)R_n)}{\eta(k) C_n R_n (1 - e^{-\Lambda}) V_c^3(k)} < 0.\end{aligned}\quad (3.45)$$

Given that $|q(k)R_n| < v_n$, the sign of the three partial derivatives demonstrates that g decreases when $V_c(k)$, $\eta(k)$, and $q(k)$ increase. As a consequence, the values of g can be evaluated by considering the worst case, corresponding to the highest values of the duty cycle and the quantization noise of the signal to transmit, and the voltage across the ultra-nanocapacitor, i.e., $\eta(k) = T_b/T_s$, $q(k) = \Delta_q/2$, and $V_c(k) = v_n$. The inequality to study is now:

$$g \leq \frac{2v_n T_s - (1 - e^{-\Lambda}) \Delta_q T_s R_n}{C_n R_n T_b (1 - e^{-\Lambda}) v_n^2}. \quad (3.46)$$

Given that the minimum acceptable value of the load current is equal to 0 (i.e., the transmission of a frame entirely composed by 0-bits), and its maximum value is $i_{lmax} = g C_n v_n^2 T_b / 2 T_s$ (i.e., the transmission of a frame composed by only 1-bits when the voltage across the ultra-nanocapacitor is the maximum one), the quantization step size is computed as:

$$\Delta_q = \frac{i_{lmax}}{L} = \frac{g C_n v_n^2 T_b}{2 L T_s}, \quad (3.47)$$

where L is the number of quantization levels. The explicit value of Δ_q can be used to solve the aforementioned inequality. The corresponding solution provides a further upper bound for the proportional gain g , that is $g \leq \frac{4 L T_s}{R_n C_n v_n T_b (1 - e^{-\Lambda}) (2L + 1)}$. Furthermore, by considering the initial assumption on the proportional gain g (i.e., $g > 0$), it comes that the sixth condition is satisfied when:

$$0 < g \leq \frac{4 L T_s}{R_n C_n v_n T_b (1 - e^{-\Lambda}) (2L + 1)}. \quad (3.48)$$

This constraint is used for the calculation of γ_4 in the Theorem.

Finally, the six analyzed conditions must be jointly satisfied. Thus, it is possible to obtain the lower and upper bounds of the proportional gain g , concluding the proof of Theorem 6. \square

3.3.3 Stability Analysis

The stability of the proposed discrete-time nonlinear dynamical system is now investigated.

Theorem 7. *The equilibrium point in (3.30), derived in Theorem 5, is globally asymptotically stable for any $g > 0$.*

Proof. The global asymptotic stability of the equilibrium point of the discrete-time nonlinear dynamical system described in (3.29) is evaluated through the Lyapunov's direct method [181]. To this end, a change of variables is introduced to shift the equilibrium point, V_∞ , to the origin: $v(k) = V_c(k) - V_\infty$. Given that $0 \leq V_c(k) \leq v_n$, it comes that $-V_\infty \leq v(k) \leq v_n - V_\infty$. The state equation (3.29) obtained with the constant inputs $\bar{\eta}$ and \bar{q} becomes:

$$\begin{aligned} v(k+1) &= f(v(k), \bar{\eta}, \bar{q}) = g\psi\left(e^{-\Lambda} - 1\right)(v(k) + V_\infty)^2 + \\ &\quad + e^{-\Lambda}(v(k) + V_\infty) + (1 - e^{-\Lambda})v_n - V_\infty. \end{aligned} \quad (3.49)$$

The proposed study considers as Lyapunov function $\mathcal{L}(v(k)) = v^2(k)$, and verifies the following three well-known conditions [181]. First, the Lyapunov function must be positive-definite (i.e., $\mathcal{L}(0) = 0 \wedge \mathcal{L}(v(k)) > 0, \forall v(k) \neq 0$). This condition is always true because the function is defined as the square of $v(k)$. Second, the Lyapunov function must be radially unbounded (i.e., $|v(k)| \rightarrow \infty \Rightarrow \mathcal{L}(v(k)) \rightarrow \infty$). Also in this case, it is always satisfied and the related proof is trivial. Third, the derivative of the Lyapunov function, calculated with respect to the variable $v(k)$, must be negative-definite (i.e., $\dot{\mathcal{L}}(0) = 0 \wedge \dot{\mathcal{L}}(v(k)) < 0, \forall v(k) \neq 0$). In particular, $\dot{\mathcal{L}}(v(k))$ can be computed as: $\dot{\mathcal{L}}(v(k)) = \mathcal{L}(v(k+1)) - \mathcal{L}(v(k))$. Thus, considering eq. (3.49):

$$\begin{aligned} \dot{\mathcal{L}}(v(k)) &= \mathcal{L}(v(k+1)) - \mathcal{L}(v(k)) = \mathcal{L}(f(v(k), \bar{\eta}, \bar{q})) - \mathcal{L}(v(k)) = \\ &= \left[g\psi(e^{-\Lambda} - 1)(v(k) + V_\infty)^2 + e^{-\Lambda}(v(k) + V_\infty) + \right. \\ &\quad \left. + (1 - e^{-\Lambda})v_n - V_\infty \right]^2 - v^2(k). \end{aligned} \quad (3.50)$$

Numerically, it is possible to note that the (3.50) is equal to zero only when $v(k) = 0$, otherwise it always assumes negative values. Thus, this third condition is satisfied for any value of g . \square

It is possible to conclude that the acceptable values' range of the proportional gain g given by Theorem 6 always makes the equilibrium point V_∞ globally asymptotically stable. Accordingly, the dynamical system modeled in (3.29) will converge to the equilibrium point for any initial condition (i.e., for any $V_c(0) \in [0, v_n]$) as the time index k is large enough.

3.3.4 Impact of the Proportional Gain on Both Output Variance and Time Constant

The variation of the voltage across the ultra-nanocapacitor is surely influenced by the dynamics of system inputs. However, the choice of the proportional gain has a clear impact on the variance of the output. Defining $\tilde{V}_c(k) = V_c(k) - V_\infty$, $\tilde{V}_c(k+1) = V_c(k+1) - V_\infty$, $\tilde{\eta}(k) = \eta(k) - \bar{\eta}$, and $\tilde{q}(k) = q(k) - \bar{q}$, the following result states.

Theorem 8. *Considering the linearized system around the equilibrium point, the variance of the duty cycle, $\sigma_{\tilde{\eta}}^2$, and the variance of the quantization noise, $\sigma_{\tilde{q}}^2$, the variance of the output, $\sigma_{\tilde{V}_c}^2$, is equal to:*

$$\sigma_{\tilde{V}_c}^2 = \frac{\alpha_2^2 \sigma_{\tilde{\eta}}^2 + \alpha_3^2 \sigma_{\tilde{q}}^2}{1 - \alpha_1^2}. \quad (3.51)$$

where

$$\begin{aligned} \alpha_1 &= 2g\psi \left(e^{-\Lambda} - 1 \right) V_\infty + e^{-\Lambda}; \\ \alpha_2 &= \frac{g\psi}{\bar{\eta}} V_\infty^2 \left(e^{-\Lambda} - 1 \right); \\ \alpha_3 &= R_n \left(e^{-\Lambda} - 1 \right). \end{aligned} \quad (3.52)$$

Proof. The discrete-time nonlinear dynamical system in eq. (3.29) and reported in what follows as $V_c(k+1) = f(V_c(k), \eta(k), q(k))$, can be approximated with its linearization around the equilibrium point by means of the Taylor series when the time index k is large enough:

$$V_c(k+1) = f(V_c(k), \eta(k), q(k)) \approx f(V_\infty, \bar{\eta}, \bar{q}) + \nabla f(V_\infty, \bar{\eta}, \bar{q}) \cdot \begin{bmatrix} \tilde{V}_c(k) & \tilde{\eta}(k) & \tilde{q}(k) \end{bmatrix}^T. \quad (3.53)$$

By definition, $f(V_\infty, \bar{\eta}, \bar{q}) = V_\infty$. Considering the variable $\tilde{V}_c(k+1)$, the linearized state equation becomes:

$$\begin{aligned} \tilde{V}_c(k+1) &= \left. \frac{\partial f(V_c(k), \eta(k), q(k))}{\partial V_c(k)} \right|_{V_\infty, \bar{\eta}, \bar{q}} \tilde{V}_c(k) + \left. \frac{\partial f(V_c(k), \eta(k), q(k))}{\partial \eta(k)} \right|_{V_\infty, \bar{\eta}, \bar{q}} \tilde{\eta}(k) + \\ &+ \left. \frac{\partial f(V_c(k), \eta(k), q(k))}{\partial q(k)} \right|_{V_\infty, \bar{\eta}, \bar{q}} \tilde{q}(k) = \\ &= \left(2g\psi \left(e^{-\Lambda} - 1 \right) V_\infty + e^{-\Lambda} \right) \tilde{V}_c(k) + \left(\frac{g\psi}{\bar{\eta}} V_\infty^2 \left(e^{-\Lambda} - 1 \right) \right) \tilde{\eta}(k) + \\ &+ \left(R_n \left(e^{-\Lambda} - 1 \right) \right) \tilde{q}(k) = \\ &= \alpha_1 \tilde{V}_c(k) + \alpha_2 \tilde{\eta}(k) + \alpha_3 \tilde{q}(k). \end{aligned} \quad (3.54)$$

Starting from eq. (3.54) and remembering that the external inputs are independent, it is possible to evaluate the variance of the state variable, $\sigma_{\tilde{V}_c}^2$, as a function of

the variance of input variables, $\sigma_{\tilde{\eta}}^2$ and $\sigma_{\tilde{q}}^2$, that is:

$$\sigma_{\tilde{V}_c}^2 = \alpha_1^2 \sigma_{\tilde{V}_c}^2 + \alpha_2^2 \sigma_{\tilde{\eta}}^2 + \alpha_3^2 \sigma_{\tilde{q}}^2 \Rightarrow \sigma_{\tilde{V}_c}^2 = \frac{\alpha_2^2 \sigma_{\tilde{\eta}}^2 + \alpha_3^2 \sigma_{\tilde{q}}^2}{1 - \alpha_1^2}. \quad (3.55)$$

□

Now, it is possible to evaluate the time constant of the linearized system around the equilibrium point, τ , to understand how fast the system returns at the equilibrium after a perturbation of the external inputs. In particular, the following result holds.

Theorem 9. *The time constant of the linearized system around the equilibrium point is:*

$$\tau = -\frac{T_f}{\ln(1 - (1 - e^{-\Lambda}) \sqrt{1 + 4\psi v_n g})}. \quad (3.56)$$

Proof. Considering the linearized discrete-time dynamical system reported in (3.54), its z-transform is

$$z\mathcal{V}_c(z) = \alpha_1 \mathcal{V}_c(z) + \alpha_2 \mathcal{H}(z) + \alpha_3 \mathcal{Q}(z), \quad (3.57)$$

where \mathcal{V}_c , \mathcal{H} and \mathcal{Q} are the z-transform of \tilde{V}_c , $\tilde{\eta}$ and \tilde{q} , respectively. Due to the linearity of the dynamical system, it is possible to analyze separately the two inputs by the superposition principle. Thus, the transfer function depending on the duty cycle of the signal to transmit is

$$\frac{\mathcal{V}_c(z)}{\mathcal{H}(z)} = \frac{\alpha_2}{z - \alpha_1}. \quad (3.58)$$

At the same time, the transfer function of the dynamical system depending only on the quantization noise is:

$$\frac{\mathcal{V}_c(z)}{\mathcal{Q}(z)} = \frac{\alpha_3}{z - \alpha_1}. \quad (3.59)$$

The pole of the transfer function is equal to α_1 in both cases. Thus, considering the relationship between the z-plane and the s-plane (i.e., $z = e^{sT_f}$) and the relationship between the pole and the time constant in continuous-time first order system (i.e., $s = -1/\tau$), the time constant of the linearized system around the equilibrium point is computed starting from the pole in the z-plane, that is: $z = \alpha_1 = e^{-\frac{T_f}{\tau}}$. Accordingly, given $\tau = -T_f / \ln(\alpha_1)$ and (3.54), the proof is concluded. □

The partial derivative of (3.56) with respect to the proportional gain g is equal to:

$$\frac{\partial \tau}{\partial g} = -\frac{2\psi v_n T_f (1 - e^{-\Lambda})}{\Omega (1 - (1 - e^{-\Lambda}) \Omega) \ln^2 [1 - (1 - e^{-\Lambda}) \Omega]} < 0. \quad (3.60)$$

where $\Omega = \sqrt{1 + 4\psi v_n g}$.

Since its sign is negative, it comes that a bigger value of proportional gain is preferred to obtain a smaller time constant of the linearized system and, in turn,

a faster response of the system at the equilibrium. On the other hand, Theorem 8 demonstrates that smaller values of the proportional gain g usually involve smaller variance of the output. Hence, the choice of the suitable g must be the result of a trade-off between these two conditions.

3.3.5 Discussion on Implementation and Computational Complexity

The scientific literature on nanotechnology remarks that the realization of computing, storing, and communication elements of a nanomachine is now feasible [16], bio-inspired machines communicating via molecular diffusion have been already realized in macroscale experimental testbeds [188], stand-up ZnO nanowires can be used to create ultra-nanocapacitor feeding nano-devices [113], [114], and proportional controller [13] and uniform quantizers [189] can be implemented at the nanoscale. Thus, the practical implementation of the presented power control mechanism in the near future requires a deep integration process, which fully reflects the interests of both research and industry working in this application domain.

The proposed scheme assumes that parameter settings (i.e., information related to the physical layer, application layer, and harvesting circuit) and deployment details (i.e., the distance between transmitter and receiver and the diffusion coefficient of the medium) are known a priori. Indeed, they can be used to properly set the value of the proportional gain of the controller, without requiring any further signaling overhead. The power transmission is calculated, for each frame, through four multiplications: $p(k) = (0.5\zeta C_n g) \cdot \eta(k) \cdot V_c(k) \cdot V_c(k) \cdot V_c(k)$. Since the computational complexity does not depend on system parameters and is the same for each frame, it can be considered as a constant, that is $O(1)$.

3.3.6 Performance Evaluation

The behavior of the proposed approach in conceivable scenarios and the goodness of the formulated theoretical analysis is evaluated through Matlab scripts, modeling the communication system described in Section 3.1 and the control law formulated in Section 3.3.1. Most of the system parameters are set according to the current scientific literature: the distance between transmitter and receiver is chosen in the range from $1 \mu\text{m}$ to $30 \mu\text{m}$ [37], the diffusion coefficient of the aqueous medium is set to $D = 10^{-9} \text{ m}^2/\text{s}$ [70], symbol duration and burst duration are set to $T_s = 1 \text{ s}$ and $T_b = 1 \text{ ms}$, respectively [37], the target BER is set to 5%. Considering an ultra-nanocapacitor based on onion-like carbon electrodes, conceivable values for the charge generated per unit area in each cycle time and the capacitance per unit area are $6 \text{ fC}/\mu\text{m}^2$ [89], [96] and $9 \text{ pF}/\mu\text{m}^2$ [96], [114], respectively. As $1000 \mu\text{m}^2$ is a conceivable size of both piezoelectric nanogenerator and ultra-nanocapacitor, the amount of charge per cycle, h_n , and the capacitance of the ultra-nanocapacitor, C_n ,

are set to 6 pC and 9 nF, respectively [96], [114]. A conceivable value for the generator voltage is 0.42 V [92], [94], [96]. The resulting source resistor is $R_n = v_n t_n / h_n$, where the time duration of the harvesting cycle is set to $t_n = 1$ s [94].

To validate analytical models discussed in Section 3.3, conducted tests consider the transmission of adjacent frames (i.e., the worst condition, where $T_i = 0$) for 2000 s. The frame size is set from 10 to 30 bits. Assuming equiprobable bits ($\omega = 0.5$) [37], the average duty cycle is: $\bar{\eta} = \omega T_b / T_s = 5 \cdot 10^{-4}$. The electrical energy stored within the ultra-nanocapacitor is supposed to be converted into chemical energy through the water electrolysis process, which has a conversion rate equal to 40% [187]. The resulting chemical energy is adopted to generate insulin molecules through the polymerization of amino acids and release them, as for pure biological systems [79]. The quantization is modeled by considering the number of quantization levels, L , equal to 2^8 . With reference to the reception process, the ligand-receptor reaction and the amplitude detection scheme are used to decode the transmitted signal. The number of receptors r , the forward reaction rate constant k_f , and the reverse reaction rate constant k_r are set to 500, $20 \mu m^3/s$, and $30 s^{-1}$, respectively [68][70]. Concerning the detection process, the threshold Θ is set to the half of the maximum number of molecules received during the symbol duration at the equilibrium. Finally, to reduce the effect of statistical fluctuations, results have been obtained by averaging 1000 independent simulations.

Transmission Requirements

Matlab scripts are used to model the communication system described in Section 3.1, while considering the transmission of several consecutive frames, different communication distances, and different number of molecules encoding the bit 1. The minimum amount of energy required to transmit a frame, ϕ_{min} , is computed by assuming to uniformly distribute the related number of molecules across $N/2$ bits equal to 1 (i.e., $\omega = 0.5$). For each communication distance, tests identified the minimum number of molecules released for the transmission of bit 1, m_{min} , and in turn the value of ϕ_{min} , that ensures an average BER lower than 5%. Similarly, the maximum amount of energy required to transmit a frame, ϕ_{max} , is computed by considering frames with only one bit per frame equal to 1 (the whole transmission power is used for emitting only one bit, thus generating the highest diffusion noise and inter-symbol interference). Results reported in Figure 3.8 show that ϕ_{min} increases with the frame size and the communication distance. In fact, given that ϕ_{min} is dimensioned for transmitting $N/2$ bits equal to 1, the higher the frame size, the higher the number of molecules released for each frame. Moreover, when the communication distance increases, the concentration of molecules that reaches the receiver sphere decreases. Thus, in order to guarantee a given target BER, higher communication distances require more emitted molecules. On the other hand, ϕ_{max} decreases when the communication distance increases. In fact, according to the Fick's law of diffusion, some of the molecules emitted for a given symbol remain around the receiver sphere also after the related

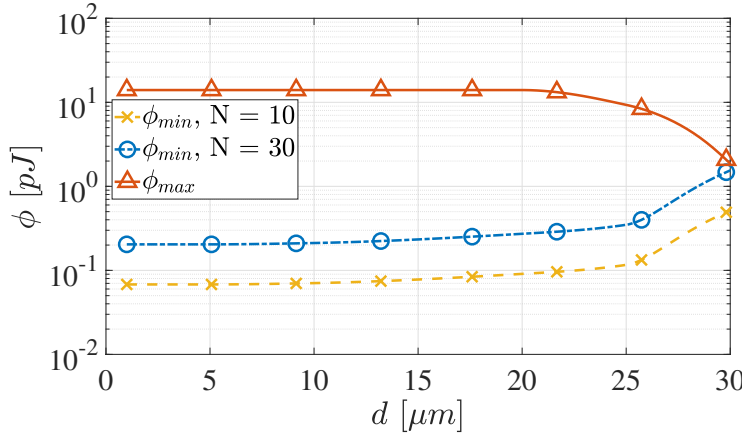


FIGURE 3.8: Minimum and maximum amount of energy required to transmit a frame.

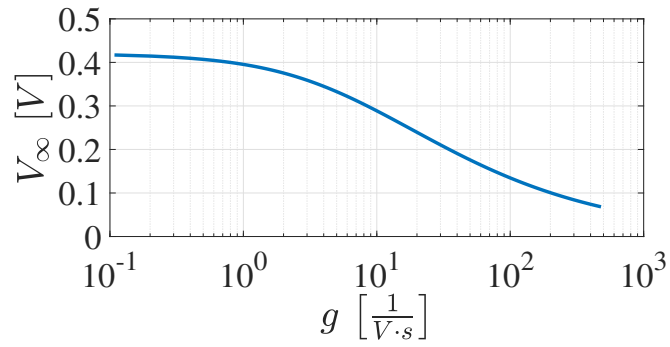
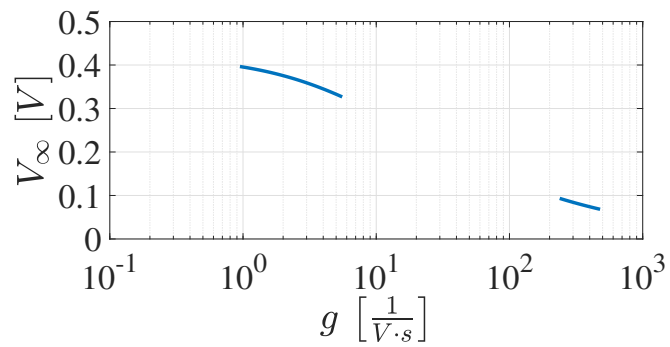
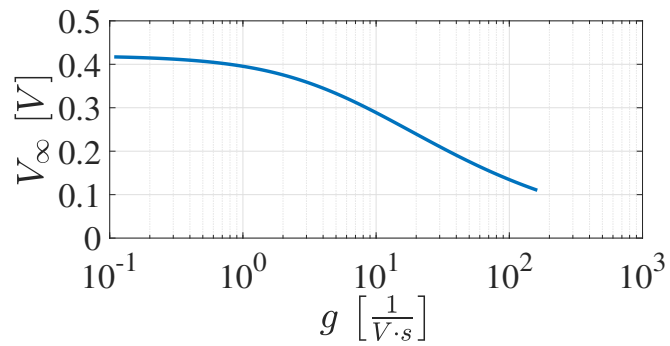
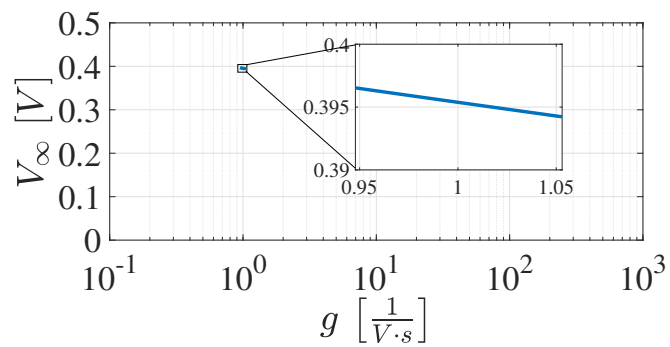
TABLE 3.2: List of Proportional Gain Values Used in the Performance Evaluation

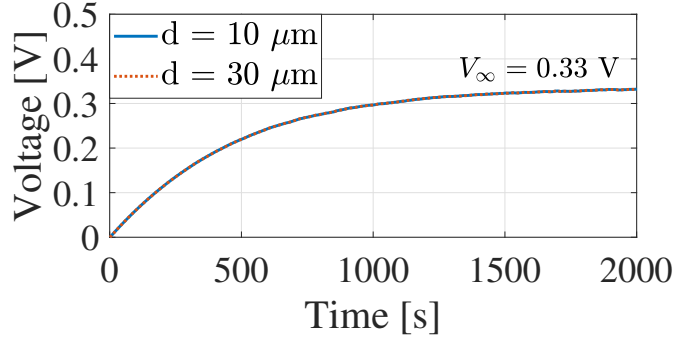
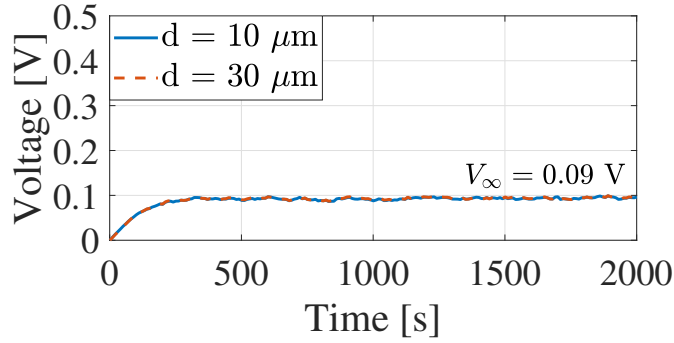
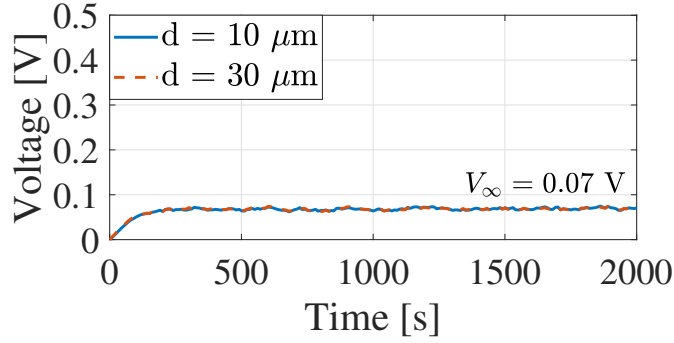
	$N = 10$		$N = 30$	
	$d = 10 \mu\text{m}$	$d = 30 \mu\text{m}$	$d = 10 \mu\text{m}$	$d = 30 \mu\text{m}$
γ_{low} (low proportional gain) [$\text{V}^{-1}\text{s}^{-1}$]	5	5	5	0.95
$\gamma_{intermediate}$ (intermediate proportional gain) [$\text{V}^{-1}\text{s}^{-1}$]	239.58	238.24	81.17	1
γ_{high} (high proportional gain) [$\text{V}^{-1}\text{s}^{-1}$]	479.04	479.04	162.22	1.05

symbol duration, thus generating diffusion noise and inter-symbol interference. The impact of these noise contributions is not negligible when the communication distance increases, affects the detection process and impairs the communication performance. This effect increases with the number of emitted molecules. Furthermore, when the communication distance is higher than $d = 30 \mu\text{m}$, the value of the minimum required energy ϕ_{min} becomes greater than the value of the maximum required energy ϕ_{max} for $N = 30$. Therefore, the constraints presented in Theorem 6 cannot be satisfied and the system is unfeasible. Note that the amount of required energy is always very low: considering a symbol duration T_s equal to 1s and frame composed by $N = 10$ bits or $N = 30$ bits, the required transmission power is few pW.

Equilibrium Point vs Acceptable Values of the Proportional Gain

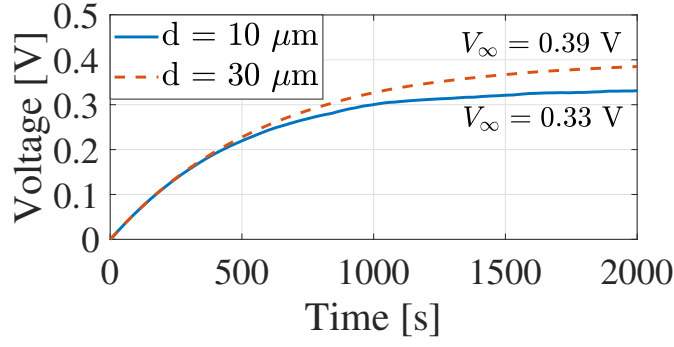
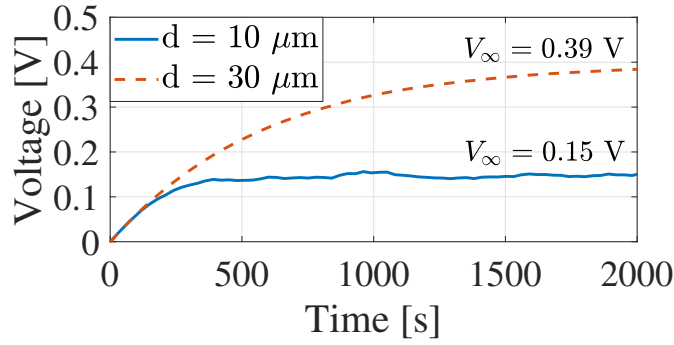
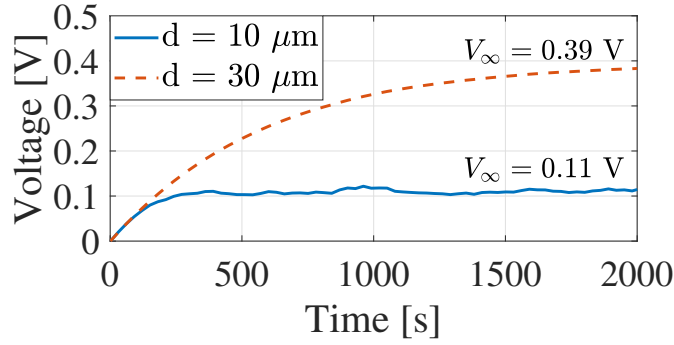
By considering Theorem 6, Figure 3.9 depicts the equilibrium point, V_∞ , as a function of the acceptable values of the proportional gain. Note that the acceptable values' range of g reduces with the frame size and the communication distance. The extreme case is registered when $N = 30$ and $d = 30 \mu\text{m}$. The value of the equilibrium point decreases when the proportional gain increases. In fact, higher values of g lead to an increment of the resulting energy budget consumed for the transmission. This, in turn, implies a reduction of the resulting energy budget at the equilibrium. The rest of this Section considers three different examples of the proportional gain, corresponding to a low, an intermediate, and a high value extracted from the acceptable range (see Table 3.2).

(A) $N = 10, d = 10 \mu\text{m}$ (B) $N = 10, d = 30 \mu\text{m}$ (C) $N = 30, d = 10 \mu\text{m}$ (D) $N = 30, d = 30 \mu\text{m}$ FIGURE 3.9: Equilibrium point, V_∞ , as a function of the proportional gain g .

(A) γ_{low} (B) $\gamma_{intermediate}$ (C) γ_{high} FIGURE 3.10: The state variable, $V_c(k)$, as a function of the time when $N = 10$.

Analysis of the State Variable at the Equilibrium

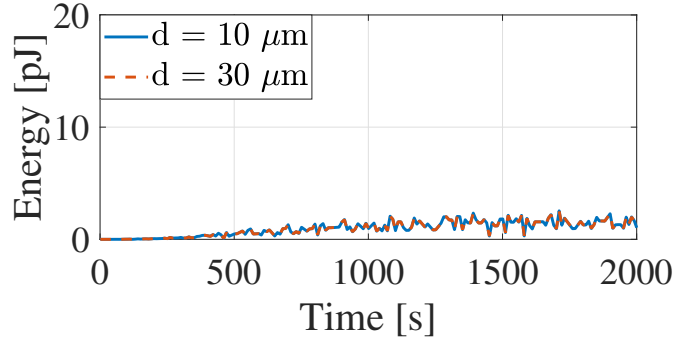
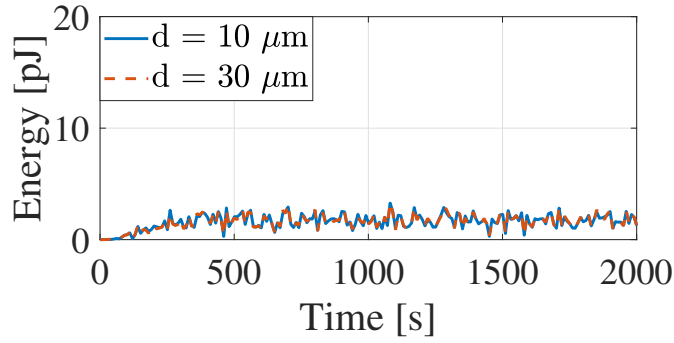
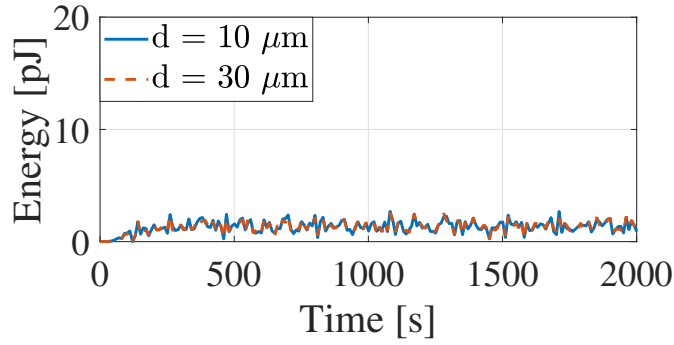
The time variation of the state variable is reported in Figure 3.10 and Figure 3.11. As already explained, a higher value of proportional gain g corresponds to a lower equilibrium point, reached after a lower amount of time. Nevertheless, given the global asymptotic stability of the equilibrium point, the expected theoretical value of V_∞ is always reached. When $N = 10$, the communication distance does not influence the results because the range of acceptable values of g (and, hence, those selected for the numerical study) is almost the same. A different behavior is registered when $N = 30$. In any case, it is important to note that the higher the communication distance, the higher the energy budget at the equilibrium. This result is not surprising: as discussed in the previous Section, a high communication distance only accepts a

(A) γ_{low} (B) $\gamma_{intermediate}$ (C) γ_{high} FIGURE 3.11: The state variable, $V_c(k)$, as a function of the time when $N = 30$.

limited set of lower values of g . Accordingly, the amount of energy consumed during the transmission process is limited, and the resulting energy budget stored into the ultra-nanocapacitor grows.

Energy Consumption

The amount of energy consumed during the time is reported in Figure 3.12 and Figure 3.13. The highest energy consumption is registered when the intermediate value of g is considered, while a smaller proportional gain corresponds to a lower energy consumption. When $N = 10$, the differences between the amount of energy consumed for different communication distances are negligible because the range of acceptable g is approximately the same. On the contrary, differences can be observed

(A) γ_{low} (B) $\gamma_{intermediate}$ (C) γ_{high} FIGURE 3.12: The consumed energy as a function of the time when $N = 10$.

when $N = 30$. Also in this case, a lower amount of energy is consumed when the communication distance increases because of the selected values of the proportional gain.

Achieved Performance

Figure 3.14 and Figure 3.15 depict the achieved communication performance. The behavior of the proposed approach is compared against traditional communication schemes encoding the symbol 1 through a burst of a constant number of molecules. Without loss of generality, the study considers static transmission scheme where $m = 100$ (a very little value suggested in [190]) and $m = 20000$ (a larger value proposed in [78]). The proposed power control mechanism registers an average

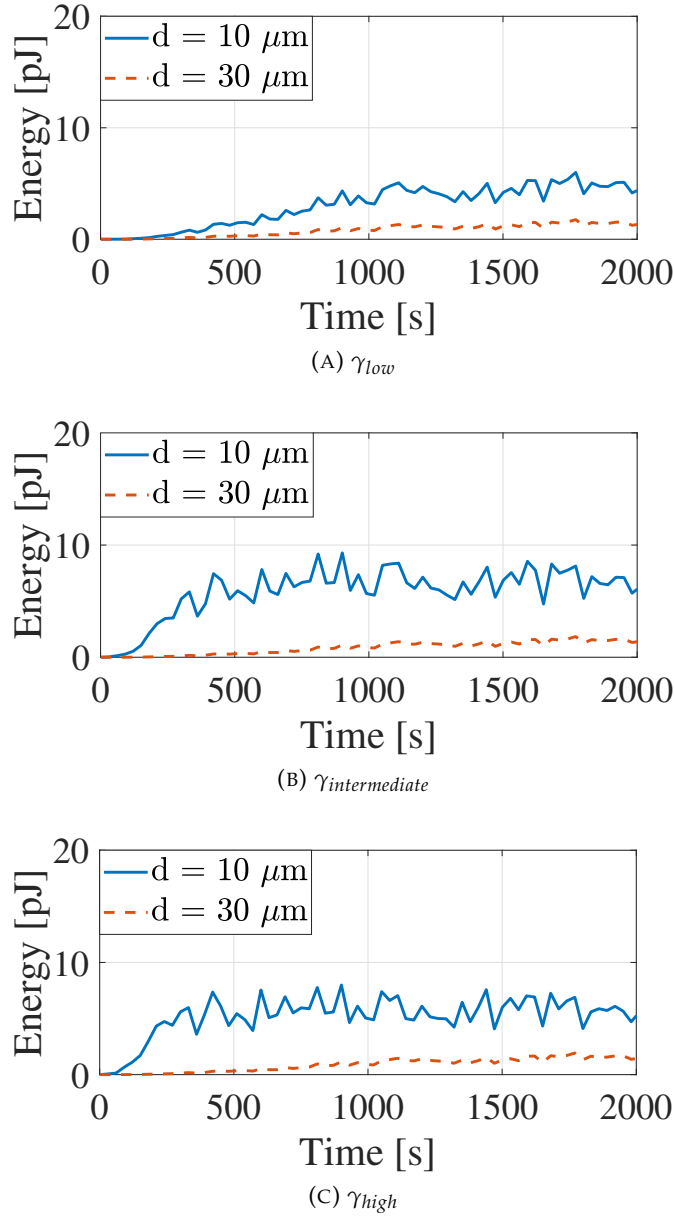


FIGURE 3.13: The consumed energy as a function of the time when $N = 30$.

BER very closed to 50% just at the beginning of the transmission process, because the ultra-nanocapacitor is empty and the state variable is very far from its equilibrium point. When the system approaches the equilibrium, the performance sharply improves and the measured BER goes below the target value. A higher communication distance generally implies a higher BER, because of the reduced number of molecules reaching the receiver and the high impact of both diffusion noise and inter-symbol interference. The amount of time needed by the system to reach the equilibrium point increases when the value of the proportional gain decreases. On the other hand, traditional transmission schemes are able to guarantee the target performance level only when the number of emitted molecules and the communication distance are very low (i.e., $m = 100$ and $d = 10 \mu\text{m}$). In the other cases, most of the

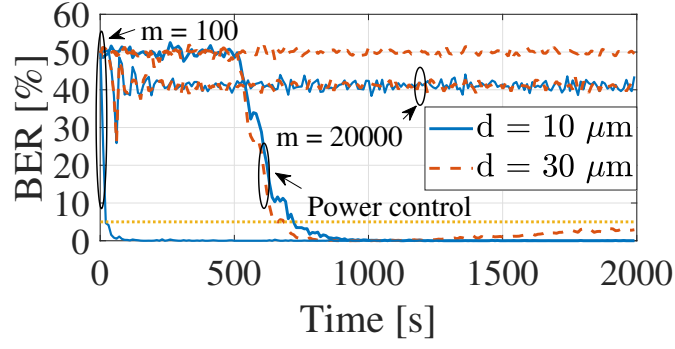
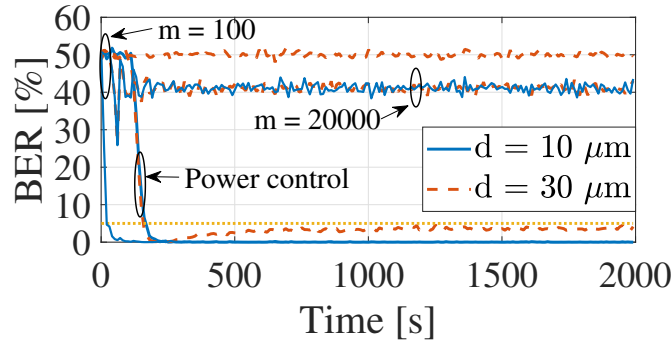
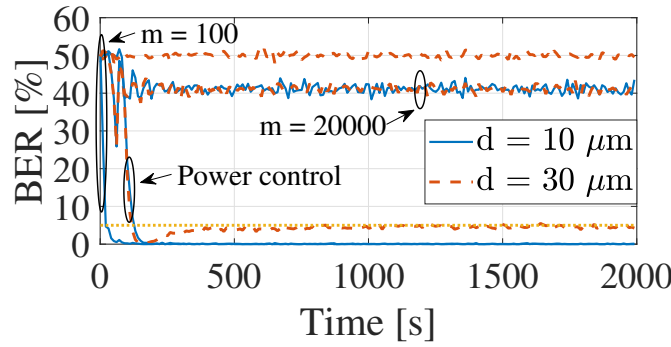
(A) γ_{low} (B) $\gamma_{intermediate}$ (C) γ_{high}

FIGURE 3.14: The average BER as a function of the time when $N = 10$. The dotted line represents the target BER of 5%.

time the transmission process fails (i.e., the receiver does not receive any molecules and decodes all the bits of the frame as 0-bits) because of the limited, or at most absent, energy budget. As a result, the comparison against state of the art transmission scheme clearly demonstrates the unique ability of the conceived approach to ensure, at the equilibrium, the expected target BER.

Impact of the Duty Cycle on Both Variance of the Output and Time Constant

To evaluate the variance of the state variable (that represents the output of the modeled system) as a function of the variance of the inputs, the duty cycle of the signal to transmit is changed by setting the idle time T_i from 0 s to 10 s (see Figure 3.16).

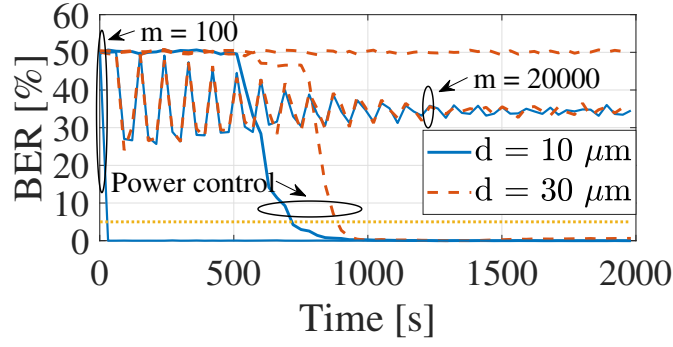
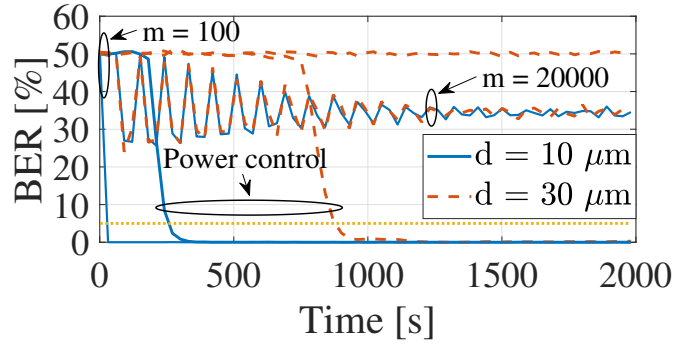
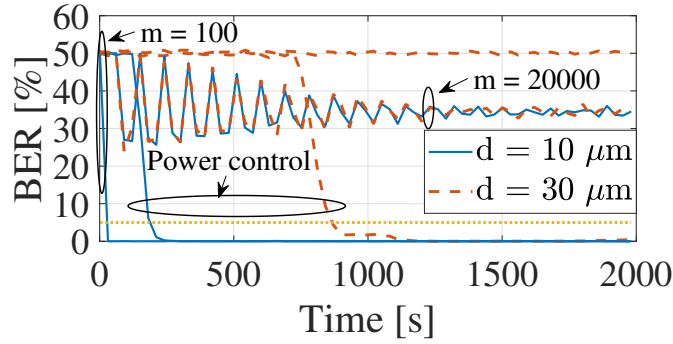
(A) γ_{low} (B) $\gamma_{intermediate}$ (C) γ_{high}

FIGURE 3.15: The average BER as a function of the time when $N = 30$. The dotted line represents the target BER of 5%.

First of all, computer simulations confirm the goodness of the formulated analytical model (specifically, Theorem 8). Moreover, it is possible to observe that when $d = 10 \mu\text{m}$, the higher the T_i (hence, the lower the duty cycle), the higher the variance of the output. In this case, the choice of a lower value of acceptable proportional gains also ensures a lower variability of the state variable. On the other hand, larger communication distances further decrease the variance of the output.

Finally, the time constant is investigated to evaluate the time required by the linearized system to return at the equilibrium after a perturbation of input parameters. Assuming that the system is at the equilibrium (i.e., the amount of energy available within the ultra-nanocapacitor is equal to the energy budget at the equilibrium), an input perturbation is modeled by considering that a certain number of

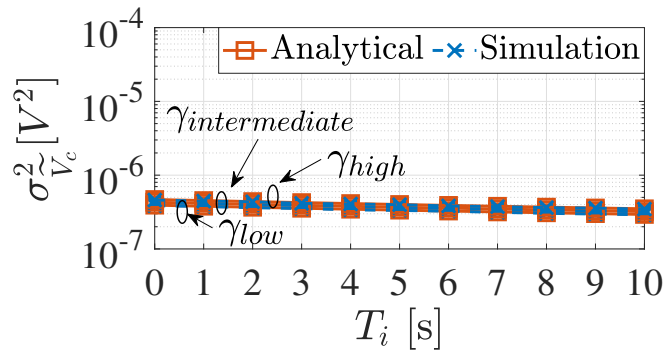
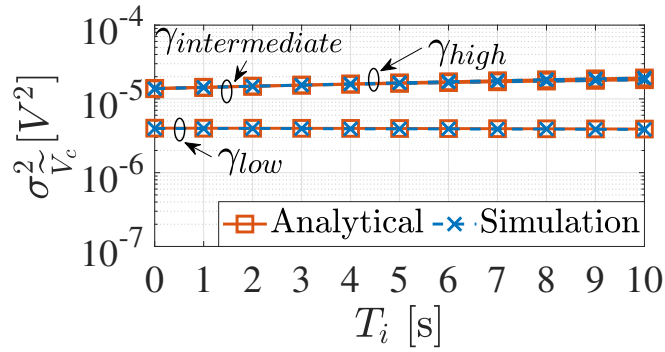
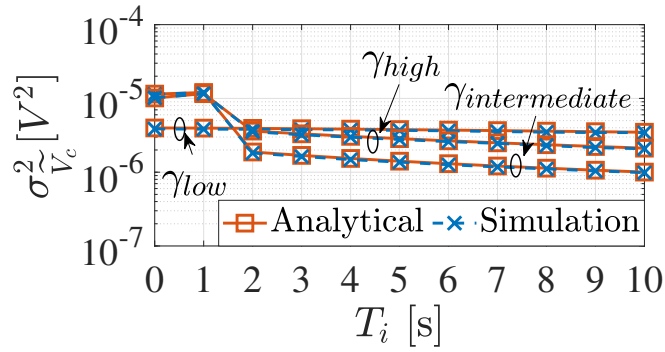
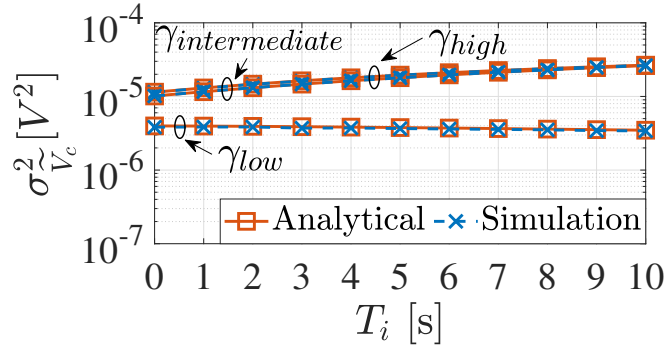


FIGURE 3.16: The variance of the output, $\sigma_{\tilde{V}_c}^2$, as a function of the idle time, T_i .

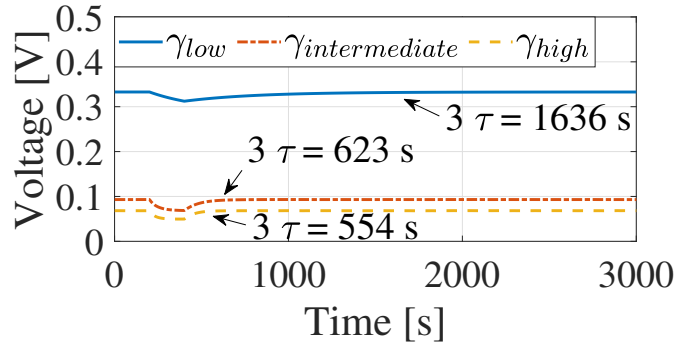
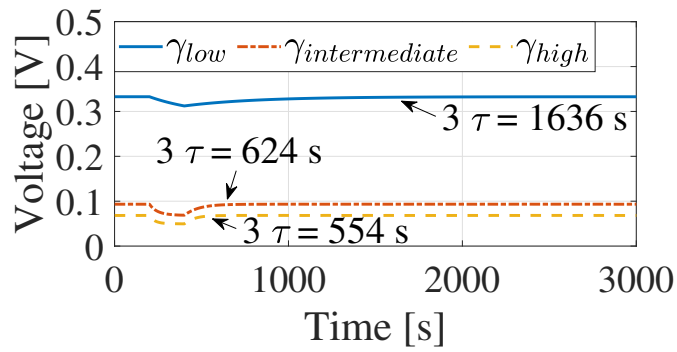
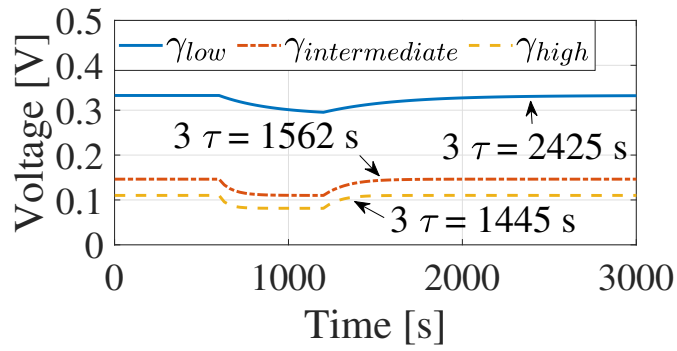
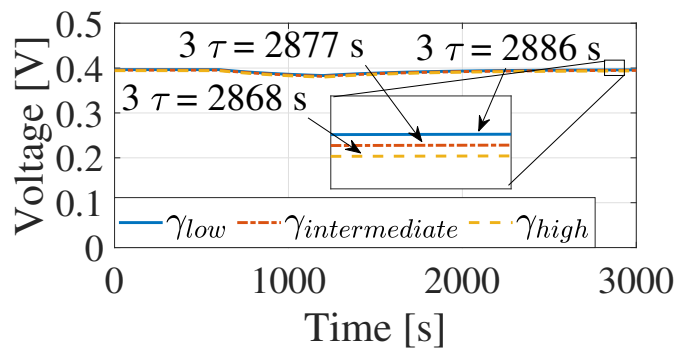
(A) $N = 10, d = 10 \mu\text{m}$ (B) $N = 10, d = 30 \mu\text{m}$ (C) $N = 30, d = 10 \mu\text{m}$ (D) $N = 30, d = 30 \mu\text{m}$

FIGURE 3.17: The average state variable as a function of the time when a perturbation of the inputs occurs.

frames entirely composed by 1-bits should be transmitted by the nano-device. This perturbation leads to a decrement of the available energy in the ultra-nanocapacitor, thus reducing the value of the state variable. Starting from Figure 3.17, it is possible to demonstrate that, when the duty cycle of the signal to transmit returns to its average value, the time required by the system to reach the 95% of its equilibrium point is equal to three-times the time constant computed for the linearized system in Theorem 9. At the same time, it is possible to note that a lower proportional gain determines a larger time constant of the linearized system around the equilibrium point. The frame size and the communication distance influence the time constant of the linearized system as well: the extreme case (i.e., $d = 30 \mu\text{m}$ and $N = 30$) corresponds to a restricted range of lower acceptable g and, in turn, implies a slower system.

To sum up, a higher value of the proportional gain corresponds to a higher variance of the output, while lower values implies a slower system response to perturbations. Therefore, the choice of the proportional gain should be done according to the parameter settings and considering the trade-off between the minimum variance of the output and the minimum time to return at the equilibrium after a perturbation.

3.3.7 Final Considerations

This Section presented a power control mechanism exploiting the feedback control theory, whose goal is to guarantee a long-lasting diffusion-based molecular communication between electrochemical nano-devices fed by a piezoelectric nanogenerator. The resulting system has been modeled with a discrete-time nonlinear state equation and deeply studied to evaluate acceptable settings guaranteeing technological constraints and global asymptotic stability. Computer simulations validated all the presented analytical models. Obtained results also demonstrated that higher values of the proportional gain bring to lower equilibrium points, the state variable always tends to the theoretical equilibrium point, the conceived communication system always ensures a BER lower than the target value when an acceptable value of the proportional gain is chosen, the variance of the output is strongly affected by the variance of the inputs and the proportional gain, and the time required by the system to return at the equilibrium after a perturbation of the inputs decreases with the increment of the proportional gain. The comparison against state of the art transmission scheme further demonstrated the unique ability of the conceived approach to ensure, at the equilibrium, the expected performance level.

Chapter 4

An Optimized Transmission Scheme for Diffusion-Based Molecular Communications

The previous chapter tackles the energy issue by adopting piezoelectric nanogenerators to feed nano-devices in DMC scenarios and managing the transmission power through feedback control mechanisms. However, the adoption of control approaches does not guarantee the simplicity of the involved nano-transmitter. On the other hand, the scientific literature has already used the optimization theory in DMCs to 1) jointly maximize the throughput and efficiency at the transmitter side based on feedback provided by the receiver [191], 2) maximize the channel capacity and the data rate [79], 3) maximize the signal to interference ratio by properly choosing the molecules release time [65], 4) find the optimal threshold or detection scheme to minimize the error probability [192]–[194], and 5) optimize the resource allocation in multi-user scenarios [195]–[197]. Among these works, only [79], [192], [195]–[197] consider some energy or molecule constraints at the transmitter. Nevertheless, none of the works in [79], [192], [195]–[197] investigates neither the adoption of energy harvesting mechanisms in the DMC context, nor the design of an optimization problem constrained by the actual amount of energy available at each time instant.

Starting from these premises, this Chapter presents a novel methodology that optimizes a DMC system composed of nano-devices fed by ZnO-based piezoelectric nanogenerators. Without loss of generality, the proposed study focuses on a telemedicine use case, where implanted nano-devices are configured to deliver (only during some periods of time and through a burst of M consecutive frames) sensed biological information. The formulation of the optimization problem requires an accurate modeling of the overall communication systems, which goes beyond the reference findings published in the current state of the art. For this reason, it is firstly derived the mean and the variance of the aggregated noise at the output of the receiver. Then, by modeling the transmission process with a current generator, this

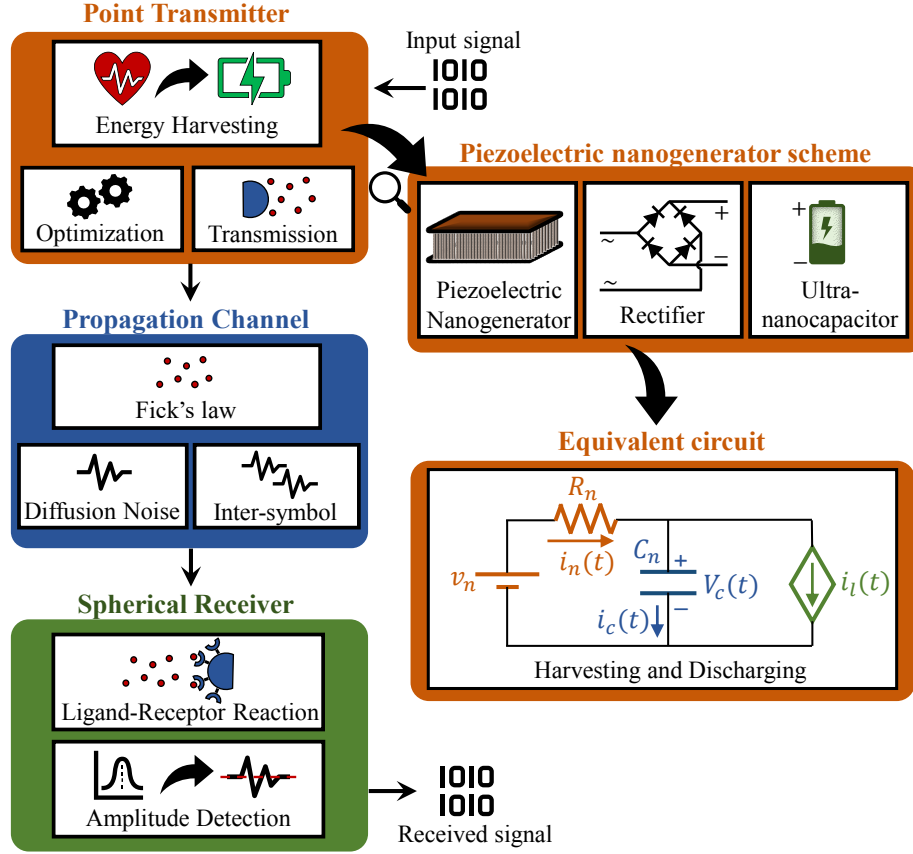


FIGURE 4.1: The considered system model for transmission, propagation, and reception processes.

Chapter presents a novel optimization problem to dynamically select the load current among a very limited subset of possible values on a per-frame basis, while satisfying energy constraints and target BER. Finally, computer simulations are used to validate the developed analytical models and illustrate the behavior of the proposed methodology in conceivable scenarios with different configuration parameters.

4.1 The Considered System Model

This Chapter focuses on a pioneering telemedicine use case, enabled by DMCs. Here, implanted nano-devices are able to deliver biological information on demand (i.e., when there is a significant variation in the measured value or when the doctor visits the patient). The considered molecular communication system includes a point transmitter fed by a piezoelectric nanogenerator, an aqueous propagation medium where molecules freely diffuse, and a spherical receiver equipped with homogeneously distributed receptors (see Figure 4.1). Transmitter and receiver are supposed to be synchronized according to one of the mechanisms already proposed in the literature [184], [185]. To model the bursty nature of the communication process, it is also assumed that the transmitter sends information molecules only during constant ON times, while staying silent for OFF time periods t_{OFF} . Without loss

TABLE 4.1: List of Main Symbols Used in This Chapter

Symbol	Description
M	Number of consecutive frames
N	Number of bits per frame
t_{ON}	On time duration
t_{OFF}	Off time duration
T_b	Time needed to release a burst of Q molecules
T_s	Symbol duration
T_f	Frame duration
m	Number of molecules released for bit 1
D	Diffusion coefficient
d	Distance between transmitter and receiver
k_f	Forward reaction rate
k_r	Reverse reaction rate constant
V_{rx}	Volume of the receiver sphere
r	Number of receptor on the receiver surface
Θ	Threshold of detection process
T	Sampling time instant at the receiver
α	Mean of the inter-symbol interference
β	Variance of the inter-symbol interference
μ_{out}	Mean of the noise at the output of the receiver
σ_{out}^2	Variance of the noise at the output of the receiver
n_d	Diffusion
n_I	Inter-symbol interference
n_{out}	Noise at the output of the receiver
v_n	Generator voltage
R_n	Resistance of the harvesting process model
C_n	Capacitance of the ultra-nanocapacitor
$i(t)$	Load
h_n	Harvested energy per cycle
t_n	Duration of the harvesting cycle
$p(t)$	Transmission power
$E_c(t)$	Consumed
ξ	Discharging conversion rate
P_e	Error probability
$V_c(t)$	Voltage across the ultra-nanocapacitor
$q(t)$	Number of enqueued
η_I	Rate of incoming packets

discrete-time state equation of the harvesting and discharging system is:

$$V_c(t_{j+1}) = V_c(t_j)e^{-\frac{T_f}{R_n C_n}} + \left(e^{-\frac{T_f}{R_n C_n}} - 1\right) \left(i(t_j)R_n - v_n\right), \quad (4.1)$$

where T_f corresponds to the frame duration and t_j is the initial time instant of the j -th frame, that is $t_j = t_k + (j - 1)T_f$ with $j \in [1, M]$. The transmission power spent during the j -th frame, $p(t_j)$, is computed by considering the conversion rate

ξ of the electrochemical process used to recover chemical energy from the electrical energy stored in the ultra-nanocapacitor [10], [187], the voltage across the ultra-nanocapacitor at the beginning of the j -th frame, $V_c(t_j)$, and the chosen load current, $i(t_j)$, that is:

$$p(t_j) = \xi V_c(t_j) i(t_j). \quad (4.2)$$

The resulting consumed energy, that is $E_c(t_j) = p(t_j)T_f$, is used to generate the information molecules related to the j -th frame. The amount of energy required to generate and release a burst of molecules is assumed to be comparable with respect to the one consumed by pure biological systems using DMCs [39], [79].

The emitted molecules freely diffuse in a fluid medium by following a Brownian motion. Accordingly, considering a burst of m released molecules, the molecules concentration at distance d and time t is derived by the Fick's law of diffusion [183]: $c(t) = m(4\pi Dt)^{-3/2}e^{-d^2/(4Dt)}$.

The concentration of molecules reaching the receiver is affected by the diffusion noise and inter-symbol interference [186]. The diffusion noise, $n_d(t)$, due to collisions of information molecules with each other and with the fluid particles in the propagation medium, is modeled as an additive Gaussian noise with zero mean and variance depending on the measured signal: $n_d(t) \sim \mathcal{N}(0, \sigma_D^2(t))$. According to [186], the variance of the diffusion noise is computed as $\sigma_D^2(t) = c(t)/V_{rx}$, where $c(t)$ is derived by the Fick's law of diffusion and V_{rx} is the receiver volume. The inter-symbol interference, $n_I(t)$, instead, generated by the molecular concentration related to the previously transmitted symbols, is modeled as a Gaussian random variable, i.e., $n_I(t) \sim \mathcal{N}(\alpha, \beta)$, where the mean α and the variance β depend on the communication distance, the number of emitted molecules, the propagation medium properties, and the adopted transmitter and receiver [198]. Indeed, the actual concentration of molecules reaching the receiver side at distance d and time t is equal to $c_r(t) = c(t) + n_d(t) + n_I(t)$.

The molecules concentration reaching the receiver sphere interact with the receptor placed on the receiver surface, according to the ligand-receptor reaction [68]. Without loss of generality, this work focuses on the reactive receiver model proposed in the recent and highly-cited work in [16], which represents a widely accepted model based on the ligand-receptor reaction. However, with few adjustments, the results of this work may be extended to other reactive receiver models as well. According to [16], the variation of the number of molecules really captured by the receiver, $z_r(t)$, is given by the following non-linear receiver model $dz_r(t)/dt = k_f r c_r(t) - k_f c_r(t) z_r(t) - k_r z_r(t)$, where r is the number of receptors, k_f is the forward reaction rate, k_r is the reverse reaction rate. However, assuming $k_f \ll k_r$, the non-linear term $k_f c_r(t) z_r(t)$ can be neglected and the receiver model becomes linear, that is $dz_r(t)/dt = k_f r c_r(t) - k_r z_r(t)$. Considering its Fourier transform, the receiver can be modeled as a low-pass filter with transfer function $H(f)$ and pulse response $h(t)$

described in (4.3):

$$H(f) = \frac{k_f r}{k_r + j2\pi f}; \quad h(t) = k_f r e^{-k_r t} u(t). \quad (4.3)$$

where $u(t)$ is the Heaviside's unit step function.

Finally, the received signal is sampled to detect the maximum number of molecules received in each time slot and it is compared with a given threshold, Θ . If the measured signal is higher than Θ , the receiver assumes that the received bit is equal to 1, otherwise the symbol is decoded as 0. To evaluate the optimal sampling time, it is considered the closed-form solution of the linear ligand-receptor reaction when the received concentration of molecules is only related to the emitted signal (i.e., $c_r(t) = c(t)$) without noise contributions, that is:

$$\begin{cases} \frac{dz_r(t)}{dt} = k_f r c(t) - k_r z_r(t) \\ c(t=0) = 0 \\ z_r(t=0) = 0 \end{cases} \implies z_r(t) = e^{-k_r t} k_f r \int_0^t c(\tau) e^{k_r \tau} d\tau \quad (4.4)$$

where $c(t)$ is the result of the Fick's law of diffusion. The optimal sampling time T , corresponding to the maximum received signal without noise C_{max} , is obtained by evaluating the time instant $t = T$ in which the first time derivative of (4.4), that is $dz_r(t)/dt = k_f r c(t) - k_r z_r(t)$, is equal to 0:

$$\begin{aligned} \frac{dz_r(t)}{dt} &= k_f r c(t) - k_r e^{-k_r t} k_f r \int_0^t c(\tau) e^{k_r \tau} d\tau = \\ &= k_f r \frac{m}{(4\pi D)^{3/2}} \left(\frac{e^{-\frac{d^2}{4Dt}}}{t^{3/2}} - k_r e^{-k_r t} \int_0^t \frac{e^{-\frac{d^2}{4D\tau}}}{\tau^{3/2}} e^{k_r \tau} d\tau \right) = \\ &= \frac{e^{-\frac{d^2}{4Dt}}}{t^{3/2}} - k_r e^{-k_r t} \int_0^t \frac{e^{-\frac{d^2}{4D\tau}}}{\tau^{3/2}} e^{k_r \tau} d\tau = 0, \end{aligned} \quad (4.5)$$

which can be numerically solved.

4.1.2 Developed Noise Model

The performance of the considered system is evaluated in terms of error probability. To properly evaluate the average BER, it is necessary to quantify the mean and the variance of the aggregated noise at the output of the receiver. The noise at the input of the receiver, n_{in} , is composed by the sum of two independent Gaussian random variables (i.e., the diffusion noise, n_d , and the inter-symbol interference, n_I). Hence, the aggregated noise at the output of the receiver, n_{out} , is obtained by filtering n_{in} with the low-pass filter described in (4.3).

Theorem 10. Let α , k_f , k_r , and r be the mean of the inter-symbol noise at the input of the receiver, the forward reaction rate, the reverse reaction rate, and the number of receptors

around the receiver sphere, respectively. Then, the mean of the noise at the output of the receiver is:

$$\mu_{out} = \alpha \frac{k_f r}{k_r}. \quad (4.6)$$

Proof. The sum of two independent Gaussian random variable (i.e., n_d and n_l) is still a Gaussian random variable with mean equal to the sum of the two means and variance equal to the sum of the two variances, that is $n_{in}(t) \sim \mathcal{N}(\alpha, \beta + \sigma_D^2(t))$ [199]. Thus, given the pulse response $h(t)$ derived in (4.3), the mean at the output of the receiver can be evaluated as follows:

$$\mu_{out} = \alpha * h(t) = \alpha H(0) = \alpha \frac{k_f r}{k_r}, \quad (4.7)$$

□

Theorem 11. Let k_f , k_r , r , β , D , m , V_{rx} , d , T , and b be the forward reaction rate, the reverse reaction rate, the number of receptors, the variance of the inter-symbol interference at the input of the receiver, the diffusion coefficient of the propagation medium, the number of emitted molecules for 1-bits, the volume of the receiver, the communication distance, the sampling time, and the transmitted bit, respectively. Then, the variance of the noise at the output of the receiver is:

$$\sigma_{out}^2 = \begin{cases} \frac{\beta k_f^2 r^2}{k_r^2}, & \text{if } b = 0 \\ \frac{k_f^2 r^2}{k_r} \left[\frac{\beta}{k_r} + \frac{m}{V_{rx} (4\pi D)^{\frac{3}{2}}} e^{-k_r T} \int_0^T \frac{e^{-d^2/(4Dv)}}{v^{\frac{3}{2}}} e^{k_r v} dv \right], & \text{if } b = 1 \end{cases} \quad (4.8)$$

Proof. Let $w(t)$ be a standard Gaussian random variable (i.e., $w(t) \sim \mathcal{N}(0,1)$). Considering the relationship between a Gaussian random variable and a standard Gaussian random variable, the noise at the input of the receiver can be written as $n_{in}(t) = \alpha + \sqrt{\beta + \sigma_D^2(t)} w(t)$. The autocorrelation of the noise at the input of the receiver is computed by considering two time instant, t_1 and t_2 , with $t_2 \geq t_1$:

$$\begin{aligned} R_{n_{in}}(t_1, t_2) &= E[n_{in}(t_1) \cdot n_{in}(t_2)] = \\ &= E \left[\left(\alpha + \sqrt{\beta + \sigma_D^2(t_1)} w(t_1) \right) \left(\alpha + \sqrt{\beta + \sigma_D^2(t_2)} w(t_2) \right) \right] = \\ &= \alpha^2 + \left(\beta + \sqrt{\sigma_D^2(t_1) \sigma_D^2(t_2)} \right) \delta(t_2 - t_1) \end{aligned} \quad (4.9)$$

Since the autocorrelation in (4.9) depends on the considered time instant, t_1 and t_2 , the noise process is not wide-sense stationary. Therefore, the autocorrelation at the output of the receiver is computed as follows:

$$R_{n_{out}}(t_1, t_2) = h(t_1) * h(t_2) * R_{n_{in}}(t_1, t_2). \quad (4.10)$$

where $h(t_1)$ and $h(t_2)$ are the pulse response of the receiver, evaluated in t_1 and t_2 , respectively. Considering that the term multiplied by the delta function in (4.9) is different from zero only if $t_1 = t_2$, it is possible to derive the autocorrelation of the noise at the output of the receiver:

$$\begin{aligned}
 R_{n_{out}}(t_1, t_2) &= (\alpha^2 + \beta)H(0) \int_{-\infty}^{+\infty} h(t_1 - \nu) d\nu + H(0) \int_{-\infty}^{+\infty} \sigma_D^2(\nu) h(t_1 - \nu) d\nu = \\
 &= \frac{k_f^2 r^2}{k_r} \left[(\alpha^2 + \beta) \int_{-\infty}^{+\infty} e^{-k_r(t_1 - \nu)} u(t_1 - \nu) d\nu + \right. \\
 &\quad \left. + \int_{-\infty}^{+\infty} \frac{m}{(4\pi D\nu)^{3/2} V_{rx}} e^{-\frac{d^2}{4D\nu}} u(\nu) e^{-k_r(t_1 - \nu)} u(t_1 - \nu) d\nu \right] = \\
 &= \frac{k_f^2 r^2}{k_r} \left[(\alpha^2 + \beta) e^{-k_r t_1} \int_{-\infty}^{t_1} e^{k_r \nu} d\nu + \right. \\
 &\quad \left. + \frac{m}{(4\pi D)^{3/2} V_{rx}} e^{-k_r t_1} \int_0^{t_1} \frac{e^{-\frac{d^2}{4D\nu}}}{\nu^{3/2}} e^{k_r \nu} d\nu \right] = \\
 &= \alpha^2 \frac{k_f^2 r^2}{k_r^2} + \beta \frac{k_f^2 r^2}{k_r^2} + \frac{m}{(4\pi D)^{3/2} V_{rx}} \frac{k_f^2 r^2}{k_r} e^{-k_r t_1} \int_0^{t_1} \frac{e^{-\frac{d^2}{4D\nu}}}{\nu^{3/2}} e^{k_r \nu} d\nu.
 \end{aligned} \tag{4.11}$$

Now, the power of the noise at the output of the receiver, $P_{n_{out}}$, can be computed by evaluating the autocorrelation at the output when $t_1 = t_2 = T$, that is:

$$P_{n_{out}} = R_{n_{out}}(T, T) = E[n_{out}(T)n_{out}(T)] = E[n_{out}^2(T)]. \tag{4.12}$$

where T is the sampling time instant. Indeed, starting from (4.11) and (4.12) evaluated for $t_1 = t_2 = T$ and remembering that $\sigma_D^2(t) = c(t)/V_{rx} = m(4\pi Dt)^{-3/2} e^{-d^2/(4Dt)}/V_{rx} u(t)$ (see Section 4.1.1), the power of the noise at the output of the receiver can be written as:

$$P_{n_{out}} = \frac{k_f^2 r^2}{k_r} \left[\frac{\alpha^2}{k_r} + \frac{\beta}{k_r} + \frac{m}{(4\pi D)^{3/2} V_{rx}} e^{-k_r T} \int_0^T \frac{e^{-d^2/(4D\nu)}}{\nu^{3/2}} e^{k_r \nu} d\nu \right], \tag{4.13}$$

Then, the variance of the noise at the output of the receiver is equal to:

$$\sigma_{out}^2 = P_{n_{out}} - \mu_{out}^2, \tag{4.14}$$

where the autocorrelation of the noise at the output of the receiver and the resulting variance strongly depend on the transmitted bit b . Finally, the proof can be easily concluded by substituting (4.6) and (4.13) in (4.14). \square

To sum up, the aggregated noise at the output of the receiver is obtained by filtering the noise at the input with the ligand-receptor process and it is modeled

as a Gaussian random variable with mean μ_{out} and variance σ_{out}^2 , that is $n_{out} \sim \mathcal{N}(\mu_{out}, \sigma_{out}^2)$.

Finally, in line with [200], the average BER is computed as:

$$P_e = \frac{1}{4} \left[\operatorname{erfc} \left(\frac{\Theta - \mu_{out}}{\sqrt{2\sigma_{out}^2|_{b=0}}} \right) + \operatorname{erfc} \left(\frac{\mu_{out} + C_{max}^{b=1} - \Theta}{\sqrt{2\sigma_{out}^2|_{b=1}}} \right) \right], \quad (4.15)$$

where the transmitted bits b are independent and equally distributed, Θ is the detection threshold, and $C_{max}^{b=1} = e^{-k_r T} k_f r \int_0^T c(\tau) e^{k_r \tau} d\tau$ is the maximum number of received molecules without the noise contribution when a 1-bit is emitted.

4.2 The Conceived Optimization Problem

The aim of this Chapter is to dynamically select the transmission power (i.e., the number of emitted molecules) on a per-frame basis. Hence, considering the relationship between the transmission power and the load current reported in (4.2), it is formulated an optimization problem that chooses the sequence of load currents $i(t_j)$ for $j = 1, M$ frame-by-frame, starting from a very limited subset of possible values (i.e., $i(t_j) \in \{0, i_l, i_h\}$) in order to preserve the simplicity of the transmitter. This sequence of load current values is selected in order to simultaneously minimize the number of enqueued packets and the probability that the voltage in the ultra-nanocapacitor is lower than a value ϵ at the beginning of the successive ON time, while also fulfilling energy constraints and target BER. In each ON time period, the first frame is used by the transmitter to communicate information about the selected load currents for the successive frames. This way the receiver can calculate the transmission power in each frame for 1) eliminating the bias generated by the inter-symbol interference that produces non-zero average noise and 2) optimizing the threshold value frame-by-frame. The optimization problem can be initially stated as follows:

$$\min_{i(t_j), \forall j \in [1, M]} \gamma \Pr(V_c(t_{k+1}) \leq \epsilon) + (1 - \gamma) q(t_{k+1}) \quad (4.16)$$

$$\text{s. t. } i(t_j) \in \{0, i_l, i_h\} \quad \forall j = 2, \dots, M \quad (4.17)$$

$$i(t_j) = i_l \quad \text{for } j = 1 \quad (4.18)$$

$$P_e(j) \leq \hat{P}_e \quad \forall j = 1, \dots, M \quad (4.19)$$

$$V_c(t_{j+1}) \geq 0 \quad \forall j = 1, \dots, M \quad (4.20)$$

$$i(t_j)|_{q(t_j)=0} = 0 \quad \forall j = 2, \dots, M \quad (4.21)$$

where γ is a weight assuming an arbitrary value from 0 to 1, $V_c(t_{k+1})$ is the voltage within the ultra-nanocapacitor, $q(t_{k+1})$ is the number of enqueued packet, M represents the number of frames in each t_{ON} , T_f is the frame duration, P_e is the error probability derived in (4.15), and \hat{P}_e is the target BER.

4.2.1 Formulation of the Objective Function

The final formulation of the optimization problem reported in (4.16) is obtained by evaluating the impact of the selected load current values on the objective function. First, starting from the system model described in Section 4.1, it is formulated the probability that the voltage across the ultra-nanocapacitor at time t_{k+1} is lower than ϵ .

Theorem 12. *Let the OFF time, t_{OFF} , be an exponential random variable with parameter λ_{OFF} . The probability to have at the beginning of the successive ON time an amount of voltage, $V_c(t_{k+1})$, lower than ϵ is equal to:*

$$Pr(V_c(t_{k+1}) \leq \epsilon) = 1 - e^{-\lambda_{OFF}[-R_n C_n \ln((v_n - \epsilon)/\Phi)]}, \quad (4.22)$$

where $\Phi = (v_n - V_c(t_k))e^{-\frac{MT_f}{R_n C_n}} + (1 - e^{-\frac{T_f}{R_n C_n}})R_n \sum_{j=1}^M i(t_j)e^{-\frac{(M-j)T_f}{R_n C_n}}$.

Proof. Considering the equivalent circuit depicted in Figure 4.1 and the well-known capacitor charging formulation with an initial voltage, the voltage at the beginning of the successive ON time, $V_c(t_{k+1})$, can be calculated starting from the voltage in $t_k + MT_f$:

$$V_c(t_{k+1}) = V_c(t_k + MT_f + t_{OFFk}) = v_n + (V_c(t_k + MT_f) - v_n)e^{-\frac{t_{OFFk}}{R_n C_n}} \quad (4.23)$$

If $M = 1$, the voltage across the ultra-nanocapacitor at the end of the frame can be simply computed through (4.1).

If $M = 2$, instead, the voltage across the ultra-nanocapacitor after two frames becomes:

$$\begin{aligned} V_c(t_k + 2T_f) &= V_c(t_k + T_f)e^{-\frac{T_f}{R_n C_n}} + \left(e^{-\frac{T_f}{R_n C_n}} - 1\right) \left(i(t_k + T_f)R_n - v_n\right) = \\ &= V_c(t_k)e^{-\frac{2T_f}{R_n C_n}} + \left(e^{-\frac{T_f}{R_n C_n}} - 1\right) \left[\left(e^{-\frac{T_f}{R_n C_n}} i(t_k) + i(t_k + T_f)\right) R_n + \right. \\ &\quad \left. - v_n \left(e^{-\frac{T_f}{R_n C_n}} + 1\right) \right], \end{aligned} \quad (4.24)$$

where $V_c(t_k + T_f)$ is derived by (4.1).

By generalizing, the voltage across the ultra-nanocapacitor at the end of M frames is:

$$V_c(t_k + MT_f) = V_c(t_k)e^{-\frac{MT_f}{R_n C_n}} + \left(e^{-\frac{T_f}{R_n C_n}} - 1\right) \left[R_n \sum_{j=1}^M i(t_j)e^{-\frac{(M-j)T_f}{R_n C_n}} - v_n \sum_{m=0}^{M-1} e^{-\frac{mT_f}{R_n C_n}} \right]. \quad (4.25)$$

Moreover, given that $\sum_{m=0}^{M-1} e^{-\frac{mT_f}{R_n C_n}} = (1 - e^{-\frac{MT_f}{R_n C_n}}) / (1 - e^{-\frac{T_f}{R_n C_n}})$, the (4.25) becomes:

$$V_c(t_k + MT_f) = v_n + (V_c(t_k) - v_n)e^{-\frac{MT_f}{R_n C_n}} + \left(e^{-\frac{T_f}{R_n C_n}} - 1\right) R_n \sum_{j=1}^M i(t_j)e^{-\frac{(M-j)T_f}{R_n C_n}}. \quad (4.26)$$

Now, substituting (4.26) in (4.23), it is possible to derive the amount of voltage across the ultra-nanocapacitor at t_{k+1} , that is:

$$V_c(t_{k+1}) = v_n + (V_c(t_k) - v_n)e^{-\frac{MT_f + t_{OFFk}}{R_n C_n}} - \left(e^{-\frac{t_{OFFk}}{R_n C_n}} - e^{-\frac{T_f + t_{OFFk}}{R_n C_n}}\right) R_n \sum_{j=1}^M i(t_j)e^{-\frac{(M-j)T_f}{R_n C_n}}. \quad (4.27)$$

Starting from (4.27), the probability that the voltage in the ultra-nanocapacitor at time t_{k+1} is lower than ϵ can be written as:

$$Pr(V_c(t_{k+1}) \leq \epsilon) = Pr\left(v_n + (V_c(t_k) - v_n)e^{-\frac{MT_f + t_{OFF_k}}{R_n C_n}} - \left(e^{-\frac{t_{OFF_k}}{R_n C_n}} - e^{-\frac{T_f + t_{OFF_k}}{R_n C_n}}\right) \times \right. \\ \left. \times R_n \sum_{j=1}^M i(t_j)e^{-\frac{(M-j)T_f}{R_n C_n}} \leq \epsilon\right) = Pr\left(t_{OFF_k} \leq -R_n C_n \ln\left(\frac{v_n - \epsilon}{\Phi}\right)\right), \quad (4.28)$$

where $\Phi = (v_n - V_c(t_k))e^{-\frac{MT_f}{R_n C_n}} + (1 - e^{-\frac{T_f}{R_n C_n}})R_n \sum_{j=1}^M i(t_j)e^{-\frac{(M-j)T_f}{R_n C_n}}$. It corresponds to the cumulative distribution function of the exponential random variable t_{OFF} with parameter λ_{OFF} . Accordingly:

$$Pr(V_c(t_{k+1}) \leq \epsilon) = 1 - e^{-\lambda_{OFF}[-R_n C_n \ln((v_n - \epsilon)/\Phi)]}, \quad (4.29)$$

which concludes the proof. \square

On the other hand, it is also possible to estimate the impact of selected load current values on the second element of the objective function, i.e., the amount of packets enqueued at t_{k+1} .

Theorem 13. *Considering the number of packet in the queue at t_k , $q(t_k)$, the sequence of load currents, $i(t_j)$, and the average number of incoming packet per second, λ_I , the number of packet enqueued at the beginning of the successive ON time can be estimated as:*

$$q(t_{k+1}) = q(t_k) - \sum_{j=1}^M \frac{2 \arctan(Ki(t_j))}{\pi} + (MT_f + t_{OFF_k})\lambda_I. \quad (4.30)$$

Proof. Starting from an initial number of enqueued packets in t_k of $q(t_k)$, the number of packet in the queue at t_{k+1} can be evaluated by taking into account the number of transmitted and incoming packets. The former is computed by considering the number of frames that can be potentially transmitted, M , minus the number of times the selected load current is equal to 0, η_0 . The latter, instead, corresponds to the average amount of frames generated and enqueued during M frames, η_I . Accordingly:

$$q(t_{k+1}) = q(t_k) - M + \eta_0 + \eta_I. \quad (4.31)$$

The number of times the selected load current is 0, η_0 , can be estimated by introducing a saturation function which is equal to 0 if the selected load current is 0, otherwise it is equal to 1. Accordingly, it is introduced the following saturation function:

$$\eta_0 = M - \text{sat}(i(t_j)) = M - \sum_{j=1}^M \frac{2 \arctan(Ki(t_j))}{\pi}, \quad (4.32)$$

where

$$\frac{2 \arctan(Ki(t_j))}{\pi} = \begin{cases} 0 & \text{if } i(t_j) = 0 \\ 1 & \text{if } i(t_j) \in i_l, i_h \end{cases}$$

The average number of incoming packets η_I , instead, is described as the mean of a Poisson process with parameter λ_I , that is:

$$\eta_I = (MT_f + t_{OFF_k})\lambda_I. \quad (4.33)$$

Thus, substituting (4.32) and (4.33) in (4.31), it is possible to conclude the proof. \square

4.2.2 Formulation of the Constraints

The first constraint reported in (4.17) allows choosing the sequence of load currents $i(t_j)$ among a limited set of three possible values, that is $\{0, i_l, i_h\}$. The (4.18) imposes that the first frame (i.e., the one carrying the load currents which will be used for the current ON time) is transmitted by consuming the lower current value. The constraint in (4.19), instead, allows to transmit information guaranteeing a target performance requirement, while the constraint in (4.20) avoids to consume more energy than the available one. Finally, constraint (4.21) states that a load current equal to 0 must be chosen when there are no more packets to transmit and the queue is empty.

Specifically, constraint (4.20) can be explicitly written considering the generalized expression in (4.26), that is:

$$\begin{aligned} V_c(t_{j+1}) &= V_c(t_k + jT_f) = \\ &= v_n + (V_c(t_k) - v_n) e^{-\frac{jT_f}{R_n C_n}} + \left(e^{-\frac{T_f}{R_n C_n}} - 1 \right) R_n \sum_{l=1}^j i(l) e^{-\frac{(j-l)T_f}{R_n C_n}} \geq 0. \end{aligned} \quad (4.34)$$

Accordingly, after a bit of algebra, it becomes:

$$\sum_{l=1}^j i(l) e^{-\frac{(j-l)T_f}{R_n C_n}} \leq \frac{v_n - (v_n - V_c(t_k)) e^{-\frac{jT_f}{R_n C_n}}}{(1 - e^{-\frac{T_f}{R_n C_n}}) R_n}. \quad (4.35)$$

Furthermore, it is worthwhile to note that the result of the probability in (4.22) makes sense only if the logarithm is a negative value. Thus, its argument must be lower than 1, that is:

$$\frac{v_n - \epsilon}{\Phi} \leq 1 \quad (4.36)$$

where $\Phi = (v_n - V_c(t_k)) e^{-\frac{MT_f}{R_n C_n}} + (1 - e^{-\frac{T_f}{R_n C_n}}) R_n \sum_{j=1}^M i(t_j) e^{-\frac{(M-j)T_f}{R_n C_n}}$. Thus, the possible combination of $i(t_j)$ is further limited as follows:

$$\sum_{j=1}^M i(t_j) e^{-\frac{(M-j)T_f}{R_n C_n}} \geq \frac{v_n - \epsilon - (v_n - V_c(t_k)) e^{-\frac{MT_f}{R_n C_n}}}{(1 - e^{-\frac{T_f}{R_n C_n}}) R_n}, \quad (4.37)$$

which represents a new constraint of the optimization problem.

4.2.3 Final Formulation of the Optimization Problem

Finally, considering an objective function based on (4.22) and (4.30), the constraints already formulated in (4.17), (4.18), (4.19), and (4.21), and the ones derived in (4.35) and (4.37), the resulting optimization problem to be solved becomes:

$$\begin{aligned} \min_{i(j), \forall j \in [1, M]} & \gamma \left(1 - e^{-\lambda_{OFF} [-R_n C_n \ln(\frac{v_n - \epsilon}{\Phi})]} \right) + \\ & + (1 - \gamma) \left(q(t_k) - \sum_{j=1}^M \frac{2 \arctan(Ki(t_j))}{\pi} + (MT_f + t_{OFF_k}) \lambda_I \right) \end{aligned}$$

TABLE 4.2: List of Simulation Parameters

Parameters	Values	References
D	$10^{-9} \text{ m}^2/\text{s}$	[70]
T_s	1 s	[37]
T_b	1 ms	-
r	500	[68], [70], [200]
k_f	$0.2 \mu\text{m}^3/\text{s}$	[68], [70], [200]
k_r	10 s^{-1}	[68], [70], [200]
V_{rx}	$2000 \mu\text{m}^3$	[68], [70], [200]
h_n	6 pC	[94], [96], [114]
C_n	9 nF	[94], [96], [114]
v_n	0.42 V	[92], [94], [96]
t_n	1 s	[94]
ξ	40%	[187]
$V_c(0), \epsilon$	V_{min}	-
$q(0)$	2 pkt	-
λ_I	0.05 pkt/s	-
M	10	-

$$\begin{aligned}
\text{s.t. } & i(t_j) \in \{0, i_l, i_h\} & \forall j = 2, \dots, M \\
& i(t_j) = i_l & \text{for } j = 1 \\
& P_e(j) \leq \hat{P}_e & \forall j = 1, \dots, M \\
& \sum_{l=1}^j i(l) e^{-\frac{(j-l)T_f}{R_n C_n}} \leq \frac{v_n - (v_n - V_c(t_k)) e^{-\frac{jT_f}{R_n C_n}}}{(1 - e^{-\frac{T_f}{R_n C_n}}) R_n} & \forall j = 1, \dots, M \quad (4.38) \\
& i(t_j)|_{q(t_j)=0} = 0 & \forall j = 2, \dots, M \\
& \sum_{j=1}^M i(t_j) e^{-\frac{(M-j)T_f}{R_n C_n}} \geq \frac{v_n - \epsilon - (v_n - V_c(t_k)) e^{-\frac{MT_f}{R_n C_n}}}{(1 - e^{-\frac{T_f}{R_n C_n}}) R_n}
\end{aligned}$$

where $\Phi = (v_n - V_c(t_k)) e^{-\frac{MT_f}{R_n C_n}} + (1 - e^{-\frac{T_f}{R_n C_n}}) R_n \sum_{j=1}^M i(t_j) e^{-\frac{(M-j)T_f}{R_n C_n}}$.

Note that the optimization problem stated in (4.38) can be solved by a remote monitoring device having a higher computational capability than the nano-transmitter [196]. Accordingly, starting from system parameters (e.g., the communication distance, the diffusion coefficient, and the dimension of piezoelectric nano-generator and ultra-nanocapacitor), the remote device obtains the optimal sequence of load currents and delivers it to the nano-transmitter.

4.3 Numerical Results

The feasibility study of the proposed energy-aware transmission scheme and the goodness of the formulated analytical models are investigated in different conceivable scenarios through computer simulations, carried out by using Matlab. Most of parameters related to the communication system, the harvesting process, and the optimization problem are chosen according to the current state of the art, as summarized in Table 4.2. The threshold Θ is calculated in every configuration in order to

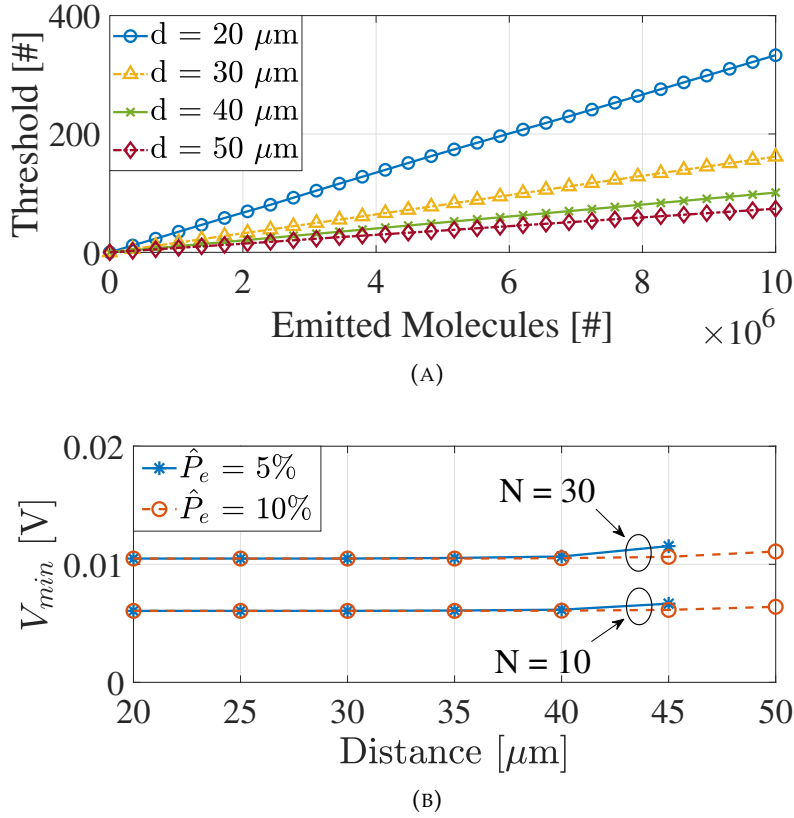


FIGURE 4.3: (a) Optimal threshold as a function of the communication distance d and the number of emitted molecules per bit m and (b) minimum required voltage as a function of the communication distance d , the frame size N , and the target BER \hat{P}_e .

minimize the error probability, while the minimum voltage V_{min} corresponds to the minimum required voltage across the ultra-nanocapacitor to reach the target BER (see Section 4.3.1 for more details).

The conducted study starts validating the noise contributions derived in Section 4.1.2. Then, it evaluates the optimal sequence of load currents addressing the optimization problem, also showing the resulting variation of the voltage across the ultra-nanocapacitor, the number of packets in the queue, the amount of energy consumed for transmission purposes, the probability that the voltage is lower than ϵ , and the achieved BER. Results are reported as a function of the time, the weight of the objective function γ , the distance between transmitter and receiver d (ranging from $20 \mu\text{m}$ to $50 \mu\text{m}$ [37]), the average off time \bar{t}_{OFF} (chosen in the range from 50 s to 200 s), the number of bit per frame N (ranging from 10 bits to 30 bits), and the target BER (set equal to 5% or 10%). Aggregated results are obtained by averaging 500 independent simulations in order to reduce the effect of statistical fluctuations.

4.3.1 Optimal Threshold and Minimum Voltage

Figure 4.3(a) depicts the optimal threshold calculated in every configuration in order to minimize the BER. The optimal threshold value decreases when the communication distance increases: according to the Fick's law of diffusion, the increment of the

distance between transmitter and receiver causes a decrement in the number of received molecules, thus decreasing the optimal threshold value. For the same reason, the threshold decreases when the number of emitted molecules per bit decreases.

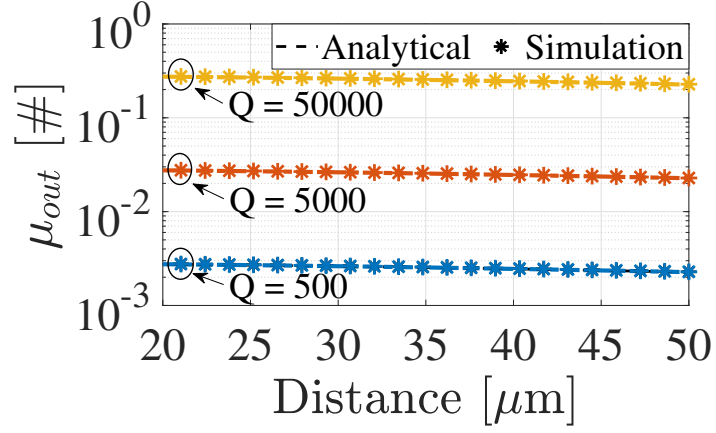
The minimum voltage across the ultra-nanocapacitor required to guarantee the target BER, instead, is shown in Figure 4.3(b). As expected, V_{min} increases when the target BER is lower, especially when the communication distance increases. In fact, a lower \hat{P}_e requires a higher number of emitted molecules when the communication is impaired by the increasing distance between transmitter and receiver. Note that a higher target BER allows to reach an increasing communication distance: when the target BER is set to 5%, the maximum reachable communication distance is 45 μm ; when the target BER increases to 10%, the communication distance increases to 50 μm as well. Moreover, considering that the frame is composed by $N/2$ bits equal to 1, the minimum voltage per frame increases with the frame size.

4.3.2 Validation of the Noise Model

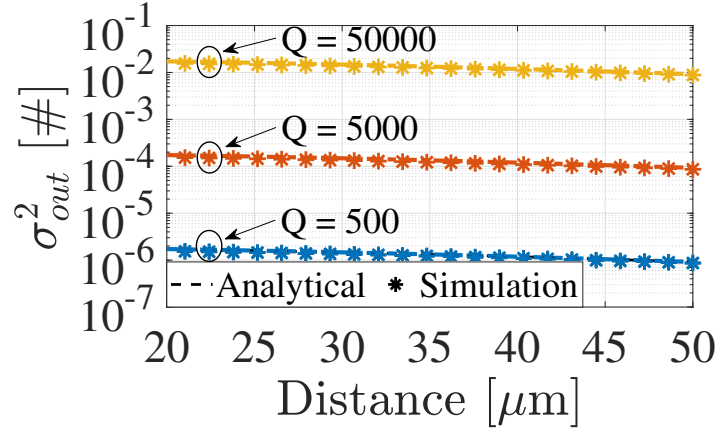
The noise model described in Section 4.1.2 is validated through computer simulations. Results reported in Figure 4.4 confirm the goodness of the formulated analytical model for different communication distances and number of emitted molecules. Furthermore, it is possible to note that, as the communication distance increases and the number of molecules decreases, the mean and the variance for both 0-bits and 1-bits at the output of the receiver decrease. In fact, increasing of the communication distance or decreasing of the emitted molecules cause a decrement in the number of received molecules due to the Fick's law of diffusion. Hence, given that the diffusion noise is strongly related to the molecules concentration reaching the receiver side and the inter-symbol interference depends on the number of received molecules, also the mean and the variance of the noise at the output of the receiver decrease.

4.3.3 Behavior of the Optimization Problem

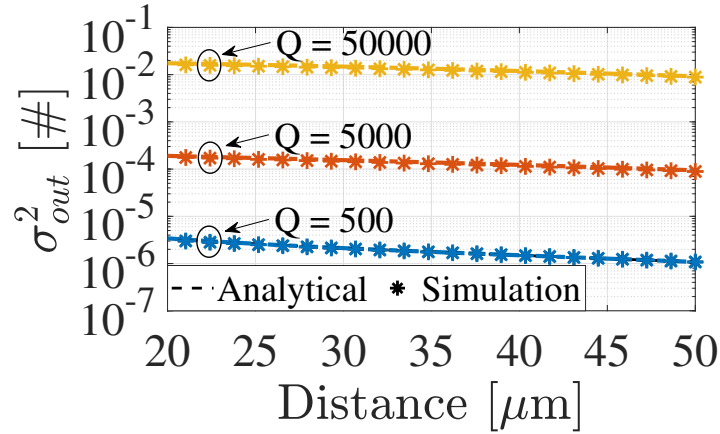
Figure 4.5 illustrates the behavior of the obtained communication system for a single realization, reported in terms of load current, voltage across the ultra-nanocapacitor, number of enqueued packets, and consumed energy during the time, by considering two different weights γ in the objective function and setting the frame size, the communication distance, the average off time, and the target BER equal to 10 bits, 30 μm , 100 s, and 5%, respectively. As expected, the resulting voltage across the ultra-nanocapacitor (i.e., the amount of available energy) and the number of enqueued packets are usually higher when a higher weight γ is used. In fact, considering the objective function in (4.38), a smaller weight γ corresponds to an optimization problem which aims at minimizing mostly the number of packets in the queue, while a higher γ envisages a stricter constraint in terms of voltage. Furthermore, since the voltage across the ultra-nanocapacitor increases with the weight γ , also the energy



(A)



(B)



(C)

FIGURE 4.4: Analytical and simulation results for (a) the mean, (b) the variance for 0-bits, and (c) the variance for 1-bits of the noise at the output of the receiver as a function of the communication distance and the number of emitted molecules.

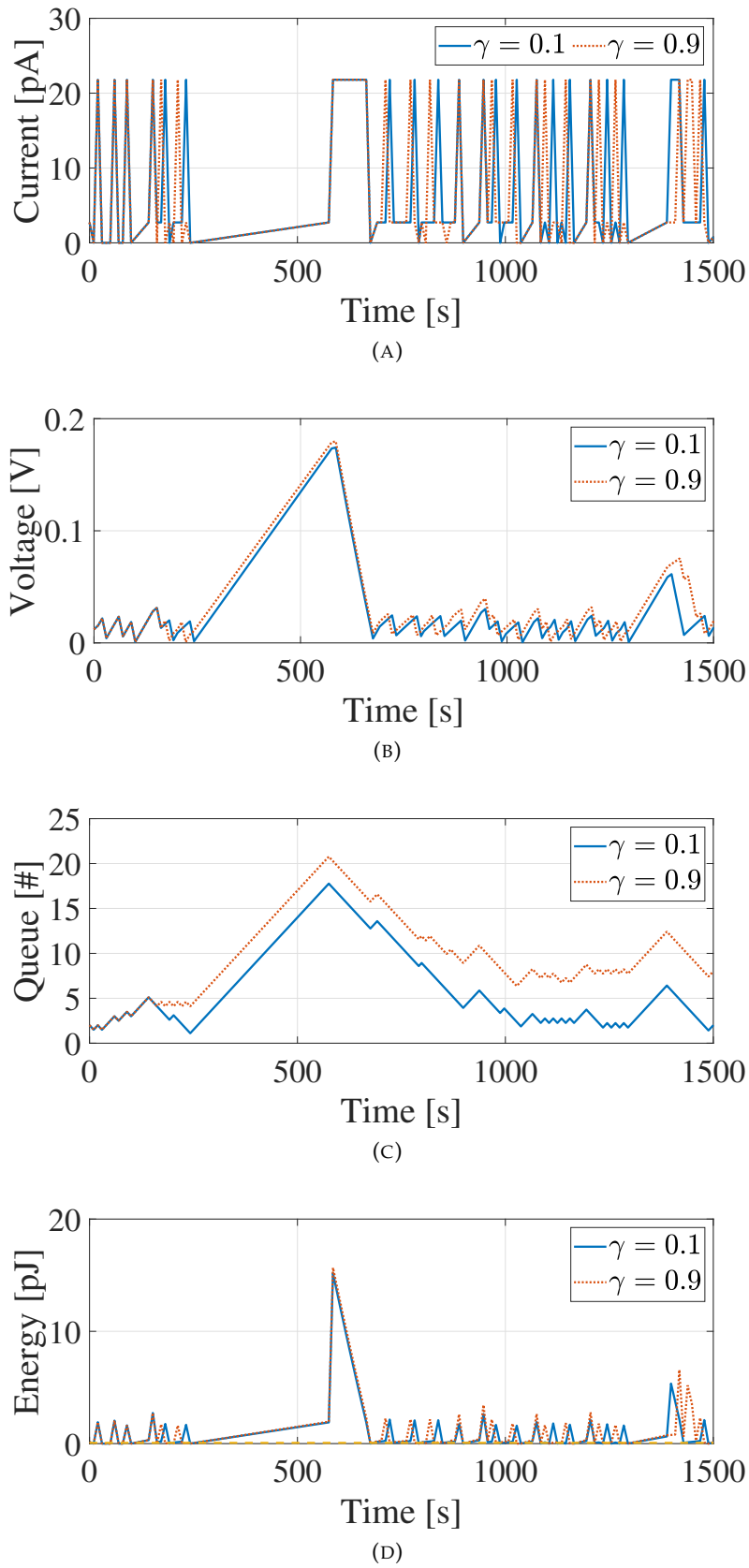


FIGURE 4.5: (a) Load current sequence, (b) voltage across the ultra-nanocapacitor, (c) number of packets in the queue, and (d) resulting consumed energy as a function of the time and the weight γ when a single realization is performed and with $N = 10$, $d = 30\mu\text{m}$, $\bar{t}_{OFF} = 100\text{s}$, and target BER = 5%.

consumed for transmission purposes is usually higher. Finally, it is important to note that the energy consumed for packets transmission is always higher than the minimum energy value required to accomplish performance requirements.

4.3.4 Average Performance of the Optimization Problem

To obtain average performance levels, the weight of the objective function γ is set to 0.5. In particular, it is studied the probability that the voltage is lower than the target value ϵ , the number of enqueued packets, the amount of energy consumed for the transmission process, and the resulting BER evaluated following the procedure described in Section 4.1.

Voltage probability

Considering the voltage across the ultra-nanocapacitor, the probability that this value goes under a target voltage ϵ is illustrated in Figure 4.6 as a function of the communication distance d , the average off time \bar{t}_{OFF} , the target BER, and the number of bit per frame N . Specifically, it is possible to note that the voltage probability usually decreases with the communication distance, especially when the number of bit per frame increases. In these cases, in fact, the optimization problem chooses more frequently a load current equal to zero in order to reach a voltage across the ultra-nanocapacitor which allows to consume an increasing amount of energy, thus releasing more information molecules and guaranteeing performance constraints. On the other hand, the probability of a voltage lower than ϵ always grows when the average off time decreases. Indeed, the increasing of the off time allows the transmitter to retrieve more energy and the voltage across the ultra-nanocapacitor increases as well.

Enqueued packets

Figure 4.7 depicts how the number of packets in the queue changes with the communication distance, the average off time, the frame size, and the target BER. In particular, the increasing of the communication distance usually leads to a growing enqueued packets due to the increment of the required energy to transmit each frame. This trend becomes more clear when also the frame size increases. In this case, the transmitter has to manage the available energy to emit an increasing number of molecules in order to guarantee performance requirements and simultaneously minimize both the probability that the voltage across the ultra-nanocapacitor goes under the threshold ϵ and the number of enqueued packets. Accordingly, in this extreme scenario, the transmitter chooses more frequently the zero load current, thus collecting more packets in the queue. Moreover, as expected, the number of incoming packets η_I grows with the increment of \bar{t}_{OFF} , thus increasing the number of total enqueued packets.

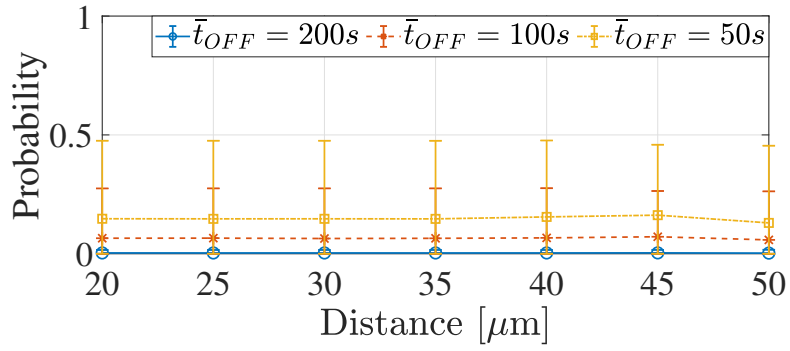
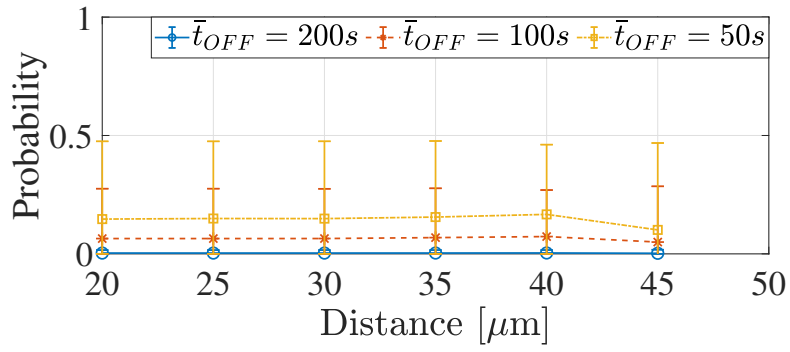
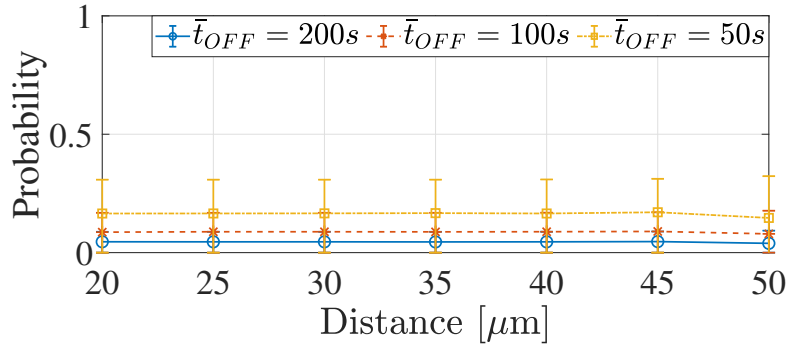
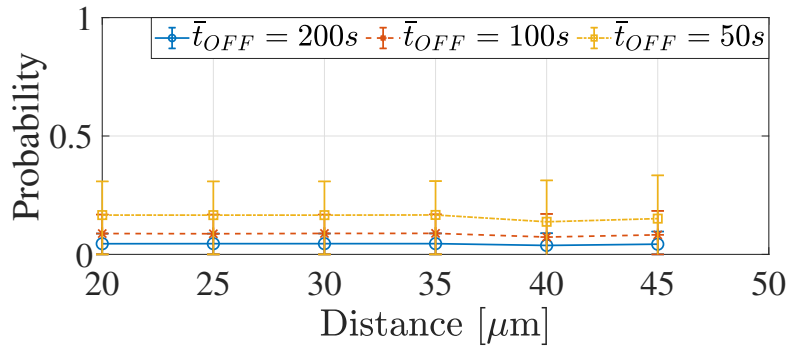


FIGURE 4.6: Probability that the voltage across the ultra-nanocapacitor is lower than ϵ as a function of the communication distance d , the average off time \bar{t}_{OFF} , the target BER, and the frame size N .

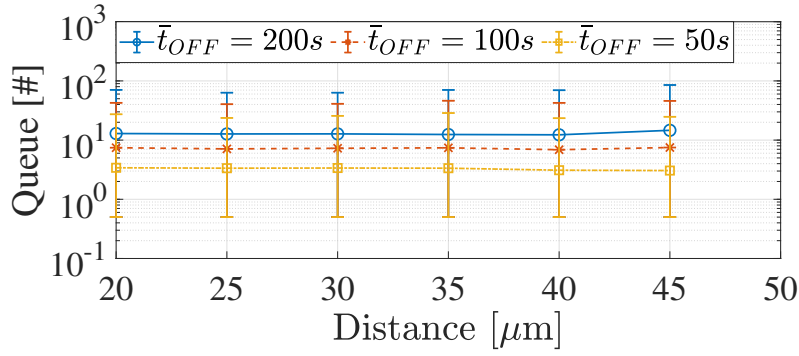
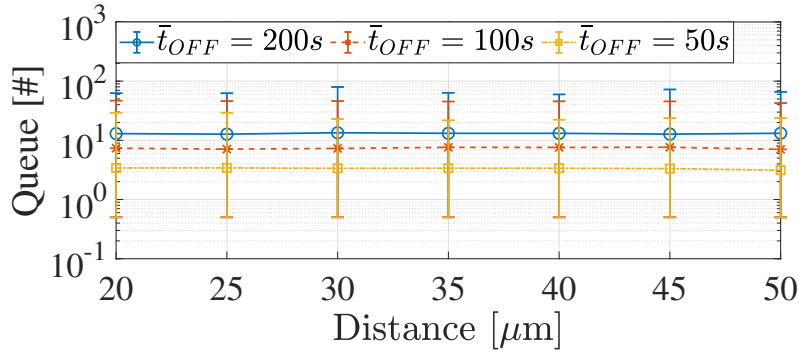
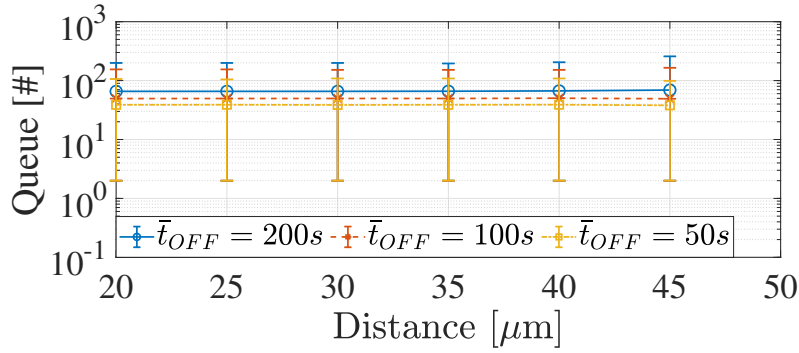
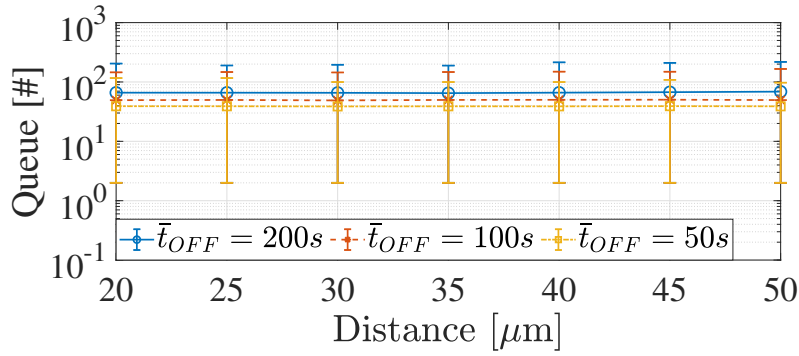
(A) Target BER = 5% and $N = 10$ bit(B) Target BER = 10% and $N = 10$ bit(C) Target BER = 5% and $N = 30$ bit(D) Target BER = 10% and $N = 30$ bit

FIGURE 4.7: Number of packets in the queue as a function of the communication distance d , the average off time \bar{t}_{OFF} , the target BER, and the frame size N .

Consumed Energy

Results reported in Figure 4.8 show the amount of energy consumed for the transmission process starting from the selected sequence of load currents for each configuration. In particular, the higher energy consumption values are reached with growing communication distances and frame sizes. In fact, as already explained, when the distance between transmitter and receiver increases, the number of information molecules required to properly transmit 1-bits and guarantee performance requirements inevitably grows, leading to an increasing energy consumption. For the same reason, a lower target BER usually demands more effort in terms of consumed energy. At the same time, the increasing of the number of bit per frame causes an increment of the number of molecules to be transmitted per frame and, in turns, higher energy consumption. The amount of consumed energy also increases when a high value of off time is used. In this case, in fact, the transmitter has more time to retrieve energy, thus increasing the amount of available and, in turns, consumed energy.

Resulting BER

Figure 4.9 presents the resulting BER as a function of the communication distance d , the average off time \bar{t}_{OFF} , the target BER and the frame size N . As expected, the measured BER increases with the communication distance because of the reduced number of molecules reaching the receiver and the high impact of both diffusion noise and inter-symbol interference. However, it is generally lower when a stricter constraint in terms of target BER is considered. The target BER is not only accomplished by the average BER, but also by the maximum obtained value in each simulation, as explicitly required by the constraint in (4.19) of the optimization problem. Finally, a lower average off time always corresponds to a higher BER: the transmitter has less time to retrieve energy, consumes less energy for transmission purposes, and uses less molecules to encode 1-bits, thus increasing the error probability.

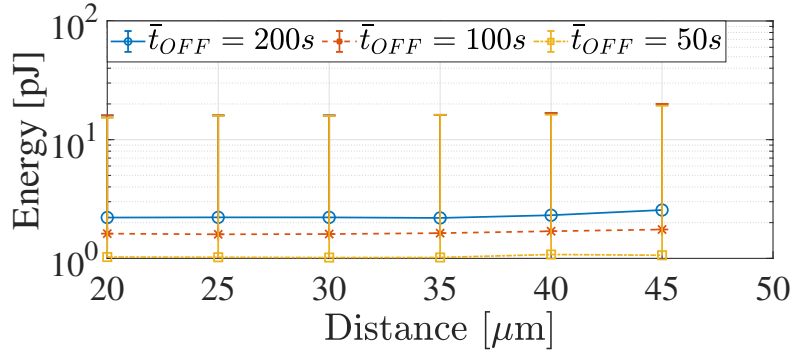
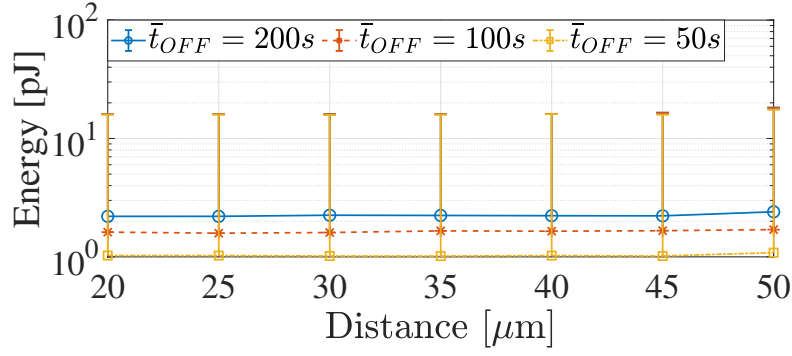
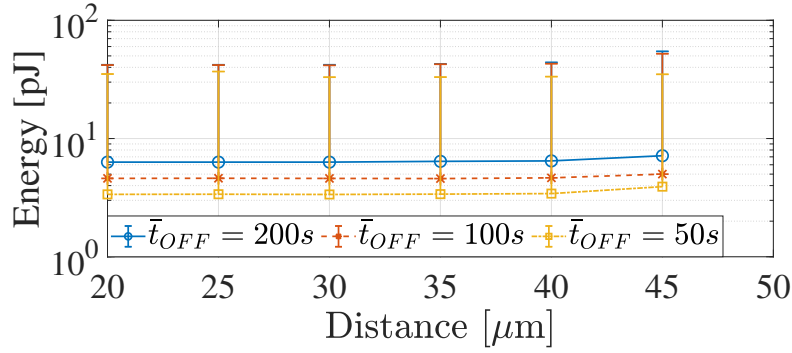
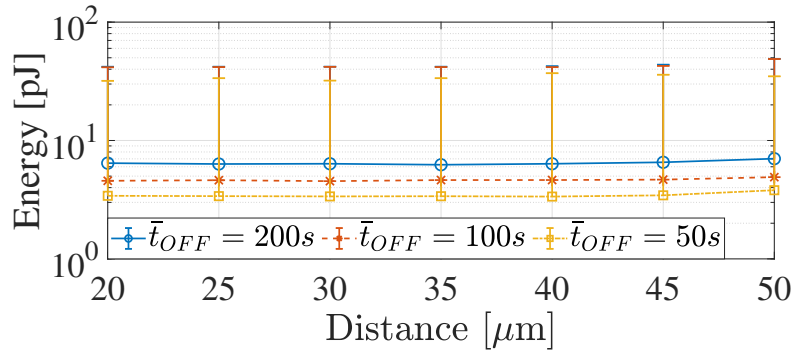
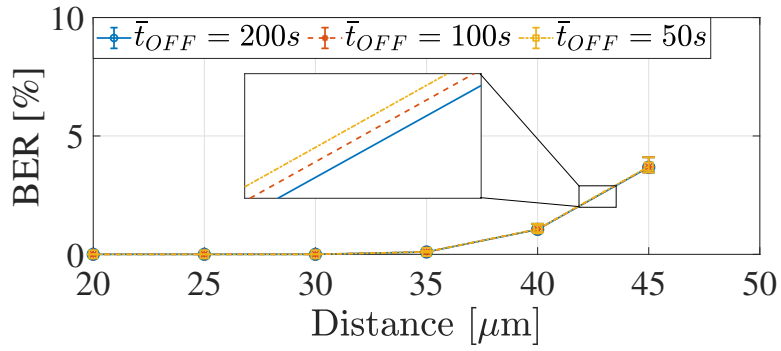
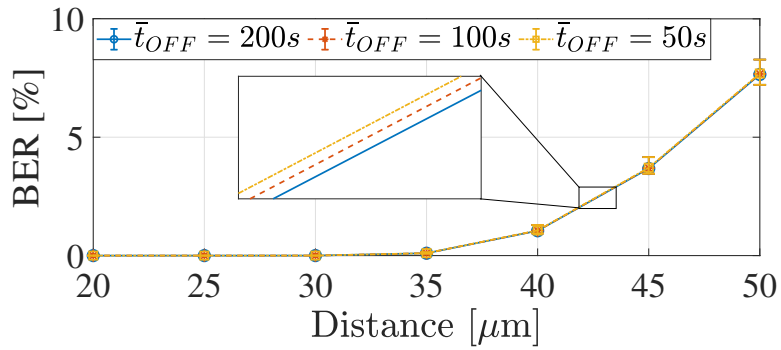
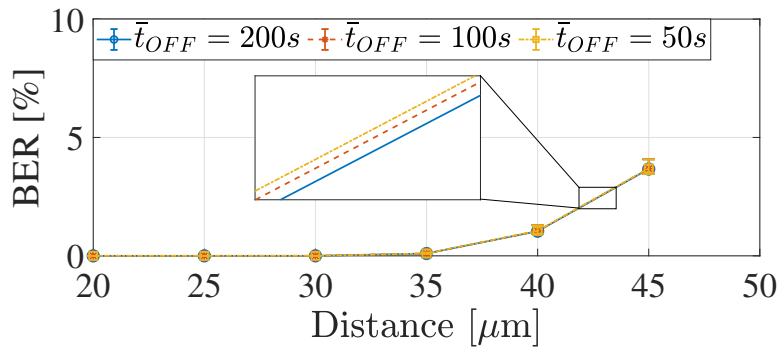
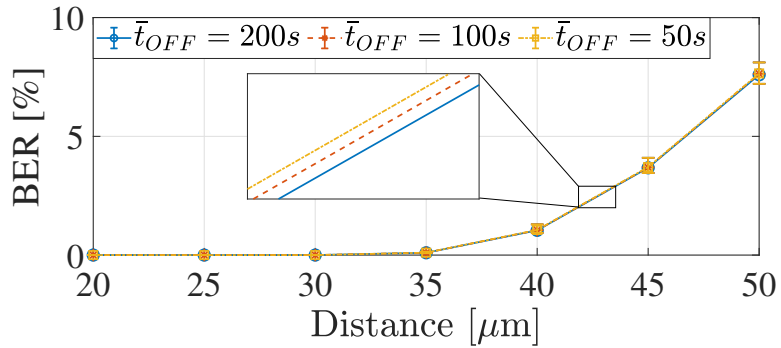
(A) Target BER = 5% and $N=10$ bit(B) Target BER = 10% and $N=10$ bit(C) Target BER = 5% and $N=30$ bit(D) Target BER = 10% and $N=30$ bit

FIGURE 4.8: Consumed energy as a function of the communication distance d , the average off time \bar{t}_{OFF} , the target BER, and the frame size N .

(A) Target BER = 5% and $N = 10$ bit(B) Target BER = 10% and $N = 10$ bit(C) Target BER = 5% and $N = 30$ bit(D) Target BER = 10% and $N = 30$ bitFIGURE 4.9: BER as a function of the communication distance d , the average off time \bar{t}_{OFF} , the target BER, and the frame size N .

4.4 Final Considerations

This Chapter presented an optimized energy-harvesting transmission scheme for a diffusion-based molecular communication system composed of nano-devices fed by piezoelectric nanogenerators. Specifically, an optimization problem that dynamically selects the transmission power (e.g., the number of molecules to release) is developed on a per-frame basis, while satisfying energy and performance constraints. To properly define objective function and constraints, this Chapter analytically derived the mean and the variance of the aggregated noise at the output of the receiver, the probability that the voltage across the ultra-nanocapacitor goes under a target value, and the number of enqueued packets based on the behavior of the transmission process. Then, computer simulations are used for validating the proposed analytical models and for evaluating the performance of the diffusion-based molecular communication system under different parameter settings. Obtained results clearly demonstrated that the proposed methodology always guarantees target performance levels.

Conclusions

The Internet of Nano-Things is a new promising networking paradigm for the interconnection of nano-devices and a powerful enabling technology for a wide area of innovative applications in different fields. Without any doubt, medical applications, such as cooperative drug delivery, regenerative medicine, and nanosurgery, emerged as the most challenging and encouraging scenarios. In this context, given the limited dimensions of involved devices, the possible restraints in the replacement of nano-batteries, and the non-negligible amount of energy consumption for communication procedures, the energy management surely represents an interesting research topic. Under these premises, this PhD thesis pursued the goal of integrating energy harvesting mechanisms and energy-aware transmission schemes to support long-lasting nanoscale wireless communications. To this end, the considered nano-devices are supposed to be equipped with Zinc Oxide-based piezoelectric nanogenerators to harvest energy from the vibrations in the surrounding environment (e.g., the human heartbeat for in-vivo applications), while the transmission power is dynamically adapted based on the available amount of energy budget.

The first investigated transmission scheme conceived a power control mechanism for a nano-device fed by a piezoelectric nanogenerator and willing to communicate in human tissues through wireless communications in the terahertz band. The resulting system has been modeled with a continuous-time nonlinear state equation and deeply studied to evaluate acceptable settings guaranteeing technological constraints and asymptotic stability. Regarding molecular communication scenarios, instead, feedback control approaches are proposed for energy-harvesting and diffusion-based communication systems, that dynamically tune the load current drained by the transmitter interface through a proportional controller on a per-bit and per-frame basis. After deriving the state equation of the resulting nonlinear systems, the analysis of their asymptotic stability and technological constraints provided the acceptable range of values for the proportional gain. To preserve the transmitter simplicity, this thesis also dealt with an optimized energy-harvesting transmission scheme for diffusion-based molecular communications. Specifically, an optimization problem that dynamically selects the transmission power (e.g., the number of molecules to release) is developed on a per-frame basis, while satisfying energy and performance constraints. Computer simulations are used throughout the thesis to validate the formulated analytical models, depict the behavior of the proposed transmission schemes in conceivable scenarios, and demonstrate the unique ability of the presented approaches to ensure the expected performance level.

Despite the growing interest of the scientific community for the Internet of Nano-Things paradigm, the research related to this topic is merely a starting point that opens up for several possible future works.

Regarding the proposed energy-aware transmission strategies, future research activities should investigate how the proposed control laws and optimization schemes affect system performance, while jointly considering other parameter settings for the proposed harvesting and discharging models, reception procedure, synchronization, and various network configurations. More in general, the scientific literature clearly demonstrated that the nanotechnology rapidly evolved and that it is now possible to think about applications, implementations, and research directions never seen before. At the time of this writing, the proposed transmission schemes can be practically implemented by integrating proportional controllers, piezoelectric nanogenerators, and nano-antennas within a bio-inspired or nanomaterial-based nano-device. Despite the current state of the art embraces preliminary studies demonstrating the possibility to implement every single part of the conceived power control mechanisms (e.g., the realization of computing, storage, and communication elements of a nano-device is feasible, bio-inspired machines communicating via molecular diffusion have been already realized in macroscale experimental testbeds, stand-up Zinc Oxide nanowires can be exploited to create ultra-nanocapacitor feeding nano-devices in molecular and electromagnetic domains, and proportional controllers can be implemented at the nanoscale), the practical implementation of a complete nano-device still represents one of the key challenges to face for the scientific community working in the field of nano-communications. Nevertheless, it is reasonable to affirm that the overall current state of the art on nanotechnology offers great opportunities to realize (i.e., practically implement) the approaches presented in this thesis in the near and far future. In addition, with particular reference to the molecular communication scenario, the research efforts currently follow the idea to use different types of molecules, including hormones, pheromones, proteins, DNA, and RNA. While the generation of these molecules at the macroscale has been widely investigated, only few contributions provide some preliminary details (i.e., chemical reactions and energy requirements) about the generation of molecules at the nanoscale. Accordingly, the study of electrochemical processes, the definition of the type of molecules, the reaction that generates/releases them and related requirements represent a key challenge to face to move from theory to practice in this promising research field.

Bibliography

- [1] J. M. Jornet and I. F. Akyildiz, "Channel Modeling and Capacity Analysis for Electromagnetic Wireless Nanonetworks in the Terahertz Band," *IEEE Transactions on Wireless Communications*, vol. 10, no. 10, pp. 3211–3221, 2011.
- [2] Q. H. Abbasi, K. Yang, N. Chopra, *et al.*, "Nano-communication for biomedical applications: A review on the state-of-the-art from physical layers to novel networking concepts," *IEEE Access*, vol. 4, pp. 3920–3935, 2016.
- [3] I. F. Akyildiz, M. Pierobon, and S. Balasubramaniam, "Moving Forward with Molecular Communication: from Theory to Human Health Applications [point of view]," *Proc. IEEE*, vol. 107, no. 5, pp. 858–865, 2019.
- [4] N. Farsad, H. B. Yilmaz, A. Eckford, C. Chae, and W. Guo, "A Comprehensive Survey of Recent Advancements in Molecular Communication," *IEEE Communications Surveys & Tutorials*, vol. 18, no. 3, pp. 1887–1919, 2016.
- [5] M. R. Da Costa, O. Kibis, and M. Portnoi, "Carbon nanotubes as a basis for terahertz emitters and detectors," *Microelectronics Journal*, vol. 40, no. 4–5, pp. 776–778, 2009.
- [6] G. J. Wilmink and J. E. Grundt, "Invited review article: Current state of research on biological effects of terahertz radiation," *Journal of Infrared, Millimeter, and Terahertz Waves*, vol. 32, no. 10, pp. 1074–1122, 2011.
- [7] T. Hogg and R. A. Freitas Jr, "Acoustic communication for medical nanorobots," *Nano Communication Networks*, vol. 3, no. 2, pp. 83–102, 2012.
- [8] G. E. Santagati and T. Melodia, "Opto-ultrasonic communications in wireless body area nanonetworks," in *2013 Asilomar Conference on Signals, Systems and Computers*, IEEE, 2013, pp. 1066–1070.
- [9] —, "Opto-ultrasonic communications for wireless intra-body nanonetworks," *Nano Communication Networks*, vol. 5, no. 1-2, pp. 3–14, 2014.
- [10] R. A. Freitas, *Nanomedicine, Volume I: Basic Capabilities*, 1st ed. Landes Bioscience, 1999.
- [11] S.-W. Hwang, H. Tao, D.-H. Kim, *et al.*, "A physically transient form of silicon electronics," *Science*, vol. 337, no. 6102, pp. 1640–1644, 2012.
- [12] S. Martel, M. Mohammadi, O. Felfoul, Z. Lu, and P. Pouponneau, "Flagellated magnetotactic bacteria as controlled mri-trackable propulsion and steering systems for medical nanorobots operating in the human microvasculature," *The International journal of robotics research*, vol. 28, no. 4, pp. 571–582, 2009.

- [13] Y. Chen, P. Kosmas, and R. Wang, "Conceptual design and simulations of a nano-communication model for drug delivery based on a transient microbot system," in *The 8th European Conference on Antennas and Propagation (EuCAP 2014)*, 2014, pp. 63–67. DOI: 10.1109/EuCAP.2014.6901693.
- [14] Y. Chen, P. Kosmas, P. S. Anwar, and L. Huang, "A touch-communication framework for drug delivery based on a transient microbot system," *IEEE transactions on nanobioscience*, vol. 14, no. 4, pp. 397–408, 2015.
- [15] I. F. Akyildiz, J. M. Jornet, and M. Pierobon, "Propagation Models for Nanocommunication Networks," in *Proceedings of the Fourth European Conference on Antennas and Propagation*, IEEE, 2010, pp. 1–5.
- [16] M. Kuscü, E. Dinc, B. Bilgin, H. Ramezani, and O. Akan, "Transmitter and Receiver Architectures for Molecular Communications: A Survey on Physical Design With Modulation, Coding, and Detection Techniques," *Proc. IEEE*, pp. 1–40, 2019. DOI: 10.1109/JPROC.2019.2916081.
- [17] N. A. Ali and M. Abu-Elkheir, "Internet of Nano-Things Healthcare Applications: Requirements, Opportunities, and Challenges," in *2015 IEEE 11th International Conference on Wireless and Mobile Computing, Networking and Communications (WiMob)*, IEEE, 2015, pp. 9–14.
- [18] D. Bi, A. Almpanis, A. Noel, Y. Deng, and R. Schober, "A Survey of Molecular Communication in Cell Biology: Establishing a New Hierarchy for Interdisciplinary Applications," *IEEE Communications Surveys & Tutorials*, 2021.
- [19] B. Atakan, O. B. Akan, and S. Balasubramaniam, "Body area nanonetworks with molecular communications in nanomedicine," *IEEE Communications Magazine*, vol. 50, no. 1, pp. 28–34, 2012.
- [20] T. Nakano, M. J. Moore, Y. Okaie, A. Enomoto, and T. Suda, "Cooperative drug delivery through molecular communication among biological nanomachines," in *2013 IEEE International Conference on Communications Workshops (ICC)*, IEEE, 2013, pp. 809–812.
- [21] U. A. Chude-Okonkwo, R. Malekian, B. T. Maharaj, and A. V. Vasilakos, "Molecular Communication and Nanonetwork for Targeted Drug Delivery: A Survey," *IEEE Communications Surveys & Tutorials*, vol. 19, no. 4, pp. 3046–3096, 2017.
- [22] J.-W. Yoo, D. J. Irvine, D. E. Discher, and S. Mitragotri, "Bio-inspired, bioengineered and biomimetic drug delivery carriers," *Nature reviews Drug discovery*, vol. 10, no. 7, pp. 521–535, 2011.
- [23] C. Sabu, C. Rejo, S. Kotta, and K. Pramod, "Bioinspired and biomimetic systems for advanced drug and gene delivery," *Journal of controlled release*, vol. 287, pp. 142–155, 2018.
- [24] E. K.-H. Chow and D. Ho, "Cancer nanomedicine: From drug delivery to imaging," *Science translational medicine*, vol. 5, no. 216, 216rv4–216rv4, 2013.

- [25] L. Felicetti, M. Femminella, G. Reali, and P. Liò, "Applications of molecular communications to medicine: A survey," *Nano Communication Networks*, vol. 7, pp. 27–45, 2016.
- [26] T. Nakano, Y. Okaie, S. Kobayashi, T. Hara, Y. Hiraoka, and T. Haraguchi, "Methods and Applications of Mobile Molecular Communication," *Proceedings of the IEEE*, vol. 107, no. 7, pp. 1442–1456, 2019.
- [27] S. Basu, Y. Gerchman, C. H. Collins, F. H. Arnold, and R. Weiss, "A synthetic multicellular system for programmed pattern formation," *Nature*, vol. 434, no. 7037, pp. 1130–1134, 2005.
- [28] B. P. Teague, P. Guye, and R. Weiss, "Synthetic morphogenesis," *Cold Spring Harbor perspectives in biology*, vol. 8, no. 9, a023929, 2016.
- [29] B. Song, R. Yang, N. Xi, K. C. Patterson, C. Qu, and K. W. C. Lai, "Cellular-level surgery using nano robots," *Journal of laboratory automation*, vol. 17, no. 6, pp. 425–434, 2012.
- [30] R. A. Freitas Jr, "Nanotechnology, nanomedicine and nanosurgery," *International journal of surgery (London, England)*, vol. 3, no. 4, pp. 243–246, 2005.
- [31] Y. Lu, R. Ni, and Q. Zhu, "Wireless communication in nanonetworks: Current status, prospect and challenges," *IEEE Transactions on Molecular, Biological and Multi-Scale Communications*, vol. 6, no. 2, pp. 71–80, 2020.
- [32] P. Kethineni, "Applications of internet of nano things: A survey," in *2017 2nd International Conference for Convergence in Technology (I2CT)*, IEEE, 2017, pp. 371–375.
- [33] C. M. Pieterse and M. Dicke, "Plant interactions with microbes and insects: From molecular mechanisms to ecology," *Trends in plant science*, vol. 12, no. 12, pp. 564–569, 2007.
- [34] V. Jamali, A. Ahmadzadeh, N. Farsad, and R. Schober, "Constant-Composition Codes for Maximum Likelihood Detection Without CSI in Diffusive Molecular Communications," *IEEE Trans. Commun.*, vol. 66, no. 5, pp. 1981–1995, 2018.
- [35] M. Ş. Kuran, H. B. Yilmaz, T. Tugcu, and I. F. Akyildiz, "Interference Effects on Modulation Techniques in Diffusion Based Nanonetworks," *Nano Commun. Netw.*, vol. 3, no. 1, pp. 65–73, 2012.
- [36] M. Zoofaghari and H. Arjmandi, "Diffusive Molecular Communication in Biological Cylindrical Environment," *IEEE Trans. NanoBiosci.*, vol. 18, no. 1, pp. 74–83, 2019.
- [37] M. Kuscü and O. B. Akan, "Maximum Likelihood Detection With Ligand Receptors for Diffusion-Based Molecular Communications in Internet of Bio-Nano Things," *IEEE Trans. Nanobiosci.*, vol. 17, no. 1, pp. 44–54, 2018.

- [38] H. Zhai, Q. Liu, A. V. Vasilakos, and K. Yang, "Anti-ISI Demodulation Scheme and Its Experiment-Based Evaluation for Diffusion-Based Molecular Communication," *IEEE Trans. NanoBiosci.*, vol. 17, no. 2, pp. 126–133, 2018.
- [39] N. Kim and C. Chae, "Novel Modulation Techniques using Isomers as Messenger Molecules for Nano Communication Networks via Diffusion," *IEEE J. Sel. Areas Commun.*, vol. 31, no. 12, pp. 847–856, 2013.
- [40] N. Garralda, I. Llatser, A. Cabellos-Aparicio, E. Alarcón, and M. Pierobon, "Diffusion-Based Physical Channel Identification in Molecular Nanonetworks," *Nano Commun. Netw.*, vol. 2, no. 4, pp. 196–204, 2011.
- [41] K. V. Srinivas, A. W. Eckford, and R. S. Adve, "Molecular Communication in Fluid Media: The Additive Inverse Gaussian Noise Channel," *IEEE Trans. Inf. Theory*, vol. 58, no. 7, pp. 4678–4692, 2012.
- [42] C. Berrou, A. Glavieux, and P. Thitimajshima, "Near shannon limit error-correcting coding and decoding: Turbo-codes. 1," in *Proceedings of ICC'93-IEEE International Conference on Communications*, IEEE, vol. 2, 1993, pp. 1064–1070.
- [43] T. K. Moon, *Error correction coding: mathematical methods and algorithms*. John Wiley & Sons, 2020.
- [44] P.-J. Shih, C.-H. Lee, P.-C. Yeh, and K.-C. Chen, "Channel codes for reliability enhancement in molecular communication," *IEEE Journal on Selected Areas in Communications*, vol. 31, no. 12, pp. 857–867, 2013.
- [45] M. S. Leeson and M. D. Higgins, "Forward Error Correction for Molecular Communications," *Nano Commun. Netw.*, vol. 3, no. 3, pp. 161–167, 2012.
- [46] C. Bai, M. S. Leeson, and M. D. Higgins, "Minimum energy channel codes for molecular communications," *Electronics Letters*, vol. 50, no. 23, pp. 1669–1671, 2014.
- [47] P.-Y. Ko, Y.-C. Lee, P.-C. Yeh, C.-h. Lee, and K.-C. Chen, "A new paradigm for channel coding in diffusion-based molecular communications: Molecular coding distance function," in *2012 IEEE global communications conference (GLOBECOM)*, IEEE, 2012, pp. 3748–3753.
- [48] J. Wang, B. Yin, and M. Peng, "Diffusion based molecular communication: Principle, key technologies, and challenges," *China Communications*, vol. 14, no. 2, pp. 1–18, 2017.
- [49] M. Pierobon and I. F. Akyildiz, "A Physical End-to-End Model for Molecular Communication in Nanonetworks," *IEEE J. Sel. Areas Commun.*, vol. 28, no. 4, pp. 602–611, 2010.

- [50] M. J. Moore, A. Enomoto, S. Watanabe, K. Oiwa, and T. Suda, "Simulating molecular motor uni-cast information rate for molecular communication," in *2009 43rd Annual Conference on Information Sciences and Systems*, IEEE, 2009, pp. 859–864.
- [51] M. A. Mangoud, M. Lestas, and T. Saeed, "Molecular motors mimo communications for nanonetworks applications," in *2018 IEEE Wireless Communications and Networking Conference (WCNC)*, IEEE, 2018, pp. 1–5.
- [52] S. Qiu, W. Haselmayr, B. Li, C. Zhao, and W. Guo, "Bacterial relay for energy-efficient molecular communications," *IEEE transactions on nanobioscience*, vol. 16, no. 7, pp. 555–562, 2017.
- [53] T. Nakano, M. Moore, A. Enomoto, and T. Suda, "Molecular communication technology as a biological ict," in *Biological functions for information and communication technologies*, Springer, 2011, pp. 49–86.
- [54] P. He, B. Pi, and Q. Liu, "Calcium signaling in mobile molecular communication networks: From a multimedia view," *IEEE Access*, vol. 7, pp. 164 825–164 834, 2019.
- [55] T. Nakano, T. Suda, M. Moore, R. Egashira, A. Enomoto, and K. Arima, "Molecular communication for nanomachines using intercellular calcium signaling," in *5th IEEE Conference on Nanotechnology, 2005.*, IEEE, 2005, pp. 478–481.
- [56] M. S. Kuran, T. Tugcu, and B. O. Edis, "Calcium signaling: Overview and research directions of a molecular communication paradigm," *IEEE Wireless Communications*, vol. 19, no. 5, pp. 20–27, 2012.
- [57] I. F. Akyildiz, M. Pierobon, and S. Balasubramaniam, "An Information Theoretic Framework to Analyze Molecular Communication Systems Based on Statistical Mechanics," *Proceedings of the IEEE*, vol. 107, no. 7, pp. 1230–1255, 2019.
- [58] M. B. Dissanayake, Y. Deng, A. Nallanathan, M. Elkahlan, and U. Mitra, "Interference Mitigation in Large-Scale Multiuser Molecular Communication," *IEEE Trans. Commun.*, 2019.
- [59] T. R. De Kievit and B. H. Iglewski, "Bacterial quorum sensing in pathogenic relationships," *Infection and immunity*, vol. 68, no. 9, pp. 4839–4849, 2000.
- [60] A. Noel, K. C. Cheung, and R. Schober, "Optimal Receiver Design for Diffusive Molecular Communication With Flow and Additive Noise," *IEEE Transactions on NanoBioscience*, vol. 13, no. 3, pp. 350–362, 2014.
- [61] V. Jamali, A. Ahmadzadeh, and R. Schober, "On the Design of Matched Filters for Molecule Counting Receivers," *IEEE Commun. Lett.*, 2017.

- [62] G. Chang, L. Lin, and H. Yan, "Adaptive Detection and ISI Mitigation for Mobile Molecular Communication," *IEEE Trans. NanoBiosci.*, vol. 17, no. 1, pp. 21–35, 2018.
- [63] A. Einolghozati, M. Sardari, and F. Fekri, "Design and Analysis of Wireless Communication Systems Using Diffusion-Based Molecular Communication among Bacteria," *IEEE transactions on wireless communications*, vol. 12, no. 12, pp. 6096–6105, 2013.
- [64] H. B. Yilmaz, A. C. Heren, T. Tugcu, and C. Chae, "Three-Dimensional Channel Characteristics for Molecular Communications with an Absorbing Receiver," *IEEE Commun. Lett.*, vol. 18, no. 6, pp. 929–932, 2014.
- [65] B. C. Akdeniz, A. E. Pusane, and T. Tugcu, "Optimal Reception Delay in Diffusion-Based Molecular Communication," *IEEE Commun. Lett.*, vol. 22, no. 1, pp. 57–60, 2018.
- [66] M. Damrath, S. Korte, and P. A. Hoeher, "Equivalent Discrete-Time Channel Modeling for Molecular Communication With Emphasize on an Absorbing Receiver," *IEEE Trans. NanoBiosci.*, vol. 16, no. 1, pp. 60–68, 2017.
- [67] Y. Wang, A. Noel, and N. Yang, "A Novel *A Priori* Simulation Algorithm for Absorbing Receivers in Diffusion-Based Molecular Communication Systems," *IEEE Trans. NanoBiosci.*, vol. 18, no. 3, pp. 437–447, 2019.
- [68] M. Pierobon and I. F. Akyildiz, "Noise Analysis in Ligand-Binding Reception for Molecular Communication in Nanonetworks," *IEEE Trans. Signal Process.*, vol. 59, no. 9, pp. 4168–4182, 2011.
- [69] A. Ahmadzadeh, H. Arjmandi, A. Burkovski, and R. Schober, "Comprehensive Reactive Receiver Modeling for Diffusive Molecular Communication Systems: Reversible Binding, Molecule Degradation, and Finite Number of Receptors," *IEEE Trans. NanoBiosci.*, vol. 15, no. 7, pp. 713–727, 2016.
- [70] M. M. Al-Zu'bi and A. S. Mohan, "Modeling of Ligand-Receptor Protein Interaction in Biodegradable Spherical Bounded Biological Micro-Environments," *IEEE Access*, vol. 6, pp. 25 007–25 018, 2018.
- [71] I. Llatser, A. Cabellos-Aparicio, M. Pierobon, and E. Alarcon, "Detection Techniques for Diffusion-based Molecular Communication," *IEEE Journal on Selected Areas in Communications*, vol. 31, no. 12, pp. 726–734, 2013.
- [72] Y. Deng, A. Noel, M. Elakashlan, A. Nallanathan, and K. C. Cheung, "Modeling and Simulation of Molecular Communication Systems With a Reversible Adsorption Receiver," *IEEE Transactions on Molecular, Biological and Multi-Scale Communications*, vol. 1, no. 4, pp. 347–362, 2015.
- [73] M. U. Mahfuz, D. Makrakis, and H. T. Mouftah, "A Comprehensive Study of Sampling-Based Optimum Signal Detection in Concentration-Encoded Molecular Communication," *IEEE Trans. NanoBiosci.*, vol. 13, no. 3, pp. 208–222, 2014.

- [74] D. Kilinc and O. B. Akan, "Receiver Design for Molecular Communication," *IEEE J. Sel. Areas Commun.*, vol. 31, no. 12, pp. 705–714, 2013.
- [75] X. Qian and M. Di Renzo, "Receiver Design in Molecular Communications: An Approach Based on Artificial Neural Networks," in *2018 15th International Symposium on Wireless Communication Systems (ISWCS)*, IEEE, 2018, pp. 1–5.
- [76] M. U. Mahfuz, D. Makrakis, and H. T. Mouftah, "A Comprehensive Analysis of Strength-Based Optimum Signal Detection in Concentration-Encoded Molecular Communication With Spike Transmission," *IEEE Trans. NanoBiosci.*, vol. 14, no. 1, pp. 67–83, 2015.
- [77] M. U. Mahfuz, D. Makrakis, and H. T. Mouftah, "Strength-Based Optimum Signal Detection in Concentration-Encoded Pulse-Transmitted OOK Molecular Communication with Stochastic Ligand-Receptor Binding," *Simulation Modelling Practice and Theory*, vol. 42, pp. 189–209, 2014.
- [78] G. H. Alshammri, M. S. Alzaidi, W. K. M. Ahmed, and V. B. Lawrence, "Low-Complexity Memory-Assisted Adaptive-Threshold Detection Scheme for On-Off-Keying Diffusion-Based Molecular Communications," in *Proc. of IEEE Sarnoff Symposium*, 2017, pp. 1–6.
- [79] M. Ş. Kuran, H. B. Yilmaz, T. Tugcu, and B. Özerman, "Energy Model for Communication via Diffusion in Nanonetworks," *Nano Commun. Netw.*, vol. 1, no. 2, pp. 86–95, 2010.
- [80] N. Farsad, H. B. Yilmaz, C. Chae, and A. Goldsmith, "Energy Model for Vesicle-based Active Transport Molecular Communication," in *Proc. of IEEE International Conference on Communications (ICC)*, 2016, pp. 1–6.
- [81] Y. Lu, M. D. Higgins, and M. S. Leeson, "Comparison of Channel Coding Schemes for Molecular Communications Systems," *IEEE Trans. Commun.*, vol. 63, no. 11, pp. 3991–4001, 2015.
- [82] C. Gonzalez-Solino and M. D. Lorenzo, "Enzymatic Fuel Cells: Towards Self-Powered Implantable and Wearable Diagnostics," *Biosensors*, vol. 8, no. 1, p. 11, 2018.
- [83] W. Jia, G. Valdés-Ramírez, A. J. Bandodkar, J. R. Windmiller, and J. Wang, "Epidermal Biofuel Cells: Energy Harvesting from Human Perspiration," *Angewandte Chemie International Edition*, vol. 52, no. 28, pp. 7233–7236, 2013.
- [84] I. Ivan, T. Vidaković-Koch, and K. Sundmacher, "Recent Advances in Enzymatic Fuel Cells: Experiments and Modeling," *Energies*, vol. 3, 2010.
- [85] S. Xu, Y. Qin, C. Xu, Y. Wei, R. Yang, and Z. L. Wang, "Self-Powered Nanowire Devices," *Nature nanotechnol.*, vol. 5, no. 5, p. 366, 2010.
- [86] Z. L. Wang, X. Wang, J. Song, J. Liu, and Y. Gao, "Piezoelectric Nanogenerators for Self-Powered Nanodevices," *IEEE Pervasive Computing*, vol. 7, no. 1, pp. 49–55, 2008.

- [87] Z. Wang, "Towards Self-Powered Nanosystems: From Nanogenerators to Nanopiezotronics," *Advanced Functional Materials*, vol. 18, pp. 3553–3567, Nov. 2008.
- [88] B. Saravanakumar, R. Mohan, K. Thiyagarajan, and S.-J. Kim, "Fabrication of a ZnO Nanogenerator for Eco-Friendly Biomechanical Energy Harvesting," *RSC Advances*, vol. 3, no. 37, pp. 16 646–16 656, 2013.
- [89] J. Briscoe, N. Jalali, P. Woolliams, *et al.*, "Measurement Techniques for Piezoelectric Nanogenerators," *Energy & Environmental Science*, vol. 6, no. 10, pp. 3035–3045, 2013.
- [90] Z. L. Wang and J. Song, "Piezoelectric Nanogenerators based on Zinc Oxide Nanowire Arrays," *Science*, vol. 312, no. 5771, pp. 242–246, 2006.
- [91] X. Wang, "Piezoelectric Nanogenerators—Harvesting Ambient Mechanical Energy at the Nanometer Scale," *Nano Energy*, vol. 1, no. 1, pp. 13–24, 2012.
- [92] S. Xu, B. Hansen, and Z. Wang, "Piezoelectric-Nanowire-Enabled Power Source for Driving Wireless Microelectronics," *Nature commun.*, vol. 1, p. 93, 2010.
- [93] X. Niu, W. Jia, S. Qian, *et al.*, "High-Performance PZT-Based Stretchable Piezoelectric Nanogenerator," *ACS Sustainable Chemistry & Engineering*, vol. 7, no. 1, pp. 979–985, 2018.
- [94] J. M. Jornet and I. F. Akyildiz, "Joint Energy Harvesting and Communication Analysis for Perpetual Wireless Nanosensor Networks in the Terahertz Band," *IEEE Trans. Nanotechnol.*, vol. 11, no. 3, pp. 570–580, 2012.
- [95] J. M. Jornet, "A Joint Energy Harvesting and Consumption Model for Self-Powered Nano-Devices in Nanonetworks," in *2012 IEEE International Conference on Communications (ICC)*, 2012, pp. 6151–6156.
- [96] S. Canovas-Carrasco, A.-J. Garcia-Sanchez, and J. Garcia-Haro, "On the Nature of Energy-Feasible Wireless Nanosensor Networks," *Sensors*, vol. 18, no. 5, p. 1356, 2018.
- [97] —, "A Nanoscale Communication Network Scheme and Energy Model for a Human Hand Scenario," *Nano Commun. Netw.*, vol. 15, pp. 17–27, 2018.
- [98] C. K. Sung, M. Egan, Z. Chen, and I. B. Collings, "Performance of Wireless Nano-Sensor Networks with Energy Harvesting," in *2014 IEEE 79th Vehicular Technology Conference (VTC Spring)*, 2014, pp. 1–5.
- [99] S. A. Wirdatmadja, M. T. Barros, Y. Koucheryavy, J. M. Jornet, and S. Balasubramaniam, "Wireless Optogenetic Nanonetworks for Brain Stimulation: Device Model and Charging Protocols," *IEEE Trans. NanoBiosci.*, vol. 16, no. 8, pp. 859–872, 2017.

- [100] M. Donohoe, B. Jennings, J. M. Jornet, and S. Balasubramaniam, "Nanodevice Arrays for Peripheral Nerve Fascicle Activation Using Ultrasound Energy-Harvesting," *IEEE Trans. Nanotechnol.*, vol. 16, no. 6, pp. 919–930, 2017.
- [101] D. Demiray, A. Cabellos-Aparicio, E. Alarcón, *et al.*, "Direct: A Model for Molecular Communication Nanonetworks Based on Discrete Entities," *Nano Commun. Netw.*, vol. 4, no. 4, pp. 181–188, 2013.
- [102] J.-T. Huang and C.-H. Lee, "On Capacity Bounds of Two-Way Diffusion Channel with Molecule Harvesting," in *Proc. IEEE ICC*, 2017, pp. 1–6.
- [103] H. G. Bafghi, A. Gohari, M. Mirmohseni, G. Aminian, and M. Nasiri-Kenari, "Diffusion-Based Molecular Communication with Limited Molecule Production Rate," *IEEE Trans. Mol. Biol. Multi-Scale Commun.*, 2019.
- [104] Y. Deng, W. Guo, A. Noel, A. Nallanathan, and M. ElKashlan, "Enabling Energy Efficient Molecular Communication via Molecule Energy Transfer," *IEEE Commun. Lett.*, vol. 21, no. 2, pp. 254–257, 2017.
- [105] W. Guo, Y. Deng, H. B. Yilmaz, *et al.*, "SMIET: Simultaneous Molecular Information and Energy Transfer," *IEEE Wireless Commun.*, vol. 25, no. 1, pp. 106–113, 2018.
- [106] Y. Alsaba, S. K. A. Rahim, and C. Y. Leow, "Beamforming in Wireless Energy Harvesting Communications Systems: A Survey," *IEEE Commun. Surveys Tuts.*, vol. 20, no. 2, pp. 1329–1360, 2018.
- [107] S. Sudevalayam and P. Kulkarni, "Energy Harvesting Sensor Nodes: Survey and Implications," *IEEE Commun. Surveys Tuts.*, vol. 13, no. 3, pp. 443–461, 2011.
- [108] M. Ku, W. Li, Y. Chen, and K. J. Ray Liu, "Advances in Energy Harvesting Communications: Past, Present, and Future Challenges," *IEEE Commun. Surveys Tuts.*, vol. 18, no. 2, pp. 1384–1412, 2016.
- [109] S. Basagni, M. Y. Naderi, C. Petrioli, *et al.*, "Wireless Sensor Networks with Energy Harvesting," *Mobile Ad Hoc Networking: Cutting Edge Directions*, S. Basagni, M. Conti, S. Giordano, and I. Stojmenovic, Eds. Hoboken, NJ: John Wiley & Sons, Inc, pp. 703–736, 2013.
- [110] S. Chandrasekaran, C. Bowen, J. Roscow, *et al.*, "Micro-Scale to Nano-Scale Generators for Energy Harvesting: Self Powered Piezoelectric, Triboelectric and Hybrid Devices," *Physics Reports*, 2018.
- [111] J. Briscoe and S. Dunn, "Piezoelectric Nanogenerators—a Review of Nanostructured Piezoelectric Energy Harvesters," *Nano Energy*, vol. 14, pp. 15–29, 2015.
- [112] S. Mohrehkesh, M. C. Weigle, and S. K. Das, "Energy Harvesting in Electromagnetic Nanonetworks," *Computer*, vol. 50, no. 2, pp. 59–67, 2017.

- [113] L. Wei, Q.-X. Liu, B. Zhu, *et al.*, "Low-Cost and High-Productivity Three-Dimensional Nanocapacitors Based on Stand-Up ZnO Nanowires for Energy Storage," *Nanoscale research lett.*, vol. 11, p. 213, 2016.
- [114] D. Pech, M. Brunet, H. Durou, *et al.*, "Ultrahigh-Power Micrometre-Sized Supercapacitors Based on Onion-Like Carbon," *Nature nanotechnol.*, vol. 5, no. 9, p. 651, 2010.
- [115] I. F. Akyildiz and J. M. Jornet, "Electromagnetic Wireless Nanosensor Networks," *Nano Communication Networks*, vol. 1, no. 1, pp. 3–19, 2010.
- [116] J. M. Jornet and I. F. Akyildiz, "Graphene-based plasmonic nano-antenna for terahertz band communication in nanonetworks," *IEEE Journal on selected areas in communications*, vol. 31, no. 12, pp. 685–694, 2013.
- [117] F. Lemic, S. Abadal, W. Tavernier, *et al.*, "Survey on terahertz nanocommunication and networking: A top-down perspective," *IEEE Journal on Selected Areas in Communications*, vol. 39, no. 6, pp. 1506–1543, 2021.
- [118] I. F. Akyildiz, C. Han, and S. Nie, "Combating the Distance Problem in the Millimeter Wave and Terahertz Frequency Bands," *IEEE Communications Magazine*, vol. 56, no. 6, pp. 102–108, 2018.
- [119] S. Walia, C. M. Shah, P. Gutruf, *et al.*, "Flexible Metasurfaces and Metamaterials: A Review of Materials and Fabrication Processes at Micro- and Nano-Scales," *Applied Physics Reviews*, vol. 2, no. 1, p. 011 303, 2015.
- [120] C. Liaskos, A. Tsioliaridou, A. Pitsillides, *et al.*, "Design and Development of Software Defined Metamaterials for Nanonetworks," *IEEE Circuits and Systems Magazine*, vol. 15, no. 4, pp. 12–25, 2015.
- [121] C. Liaskos, S. Nie, A. Tsioliaridou, A. Pitsillides, S. Ioannidis, and I. Akyildiz, "A New Wireless Communication Paradigm through Software-Controlled Metasurfaces," *IEEE Communications Magazine*, vol. 56, no. 9, pp. 162–169, 2018.
- [122] W. Tang, J. Y. Dai, M. Chen, *et al.*, "Programmable Metasurface-Based RF Chain-Free 8PSK Wireless Transmitter," *Electronics Letters*, vol. 55, no. 7, pp. 417–420, 2019.
- [123] L. Li, T. J. Cui, W. Ji, *et al.*, "Electromagnetic Reprogrammable Coding-Metasurface Holograms," *Nature communications*, vol. 8, no. 1, pp. 1–7, 2017.
- [124] S. Abadal, C. Liaskos, A. Tsioliaridou, *et al.*, "Computing and Communications for the Software-Defined Metamaterial Paradigm: A Context Analysis," *IEEE access*, vol. 5, pp. 6225–6235, 2017.
- [125] M. A. McEvoy and N. Correll, "Materials that Couple Sensing, Actuation, Computation, and Communication," *Science*, vol. 347, no. 6228, 2015.

- [126] N. Correll, P. Dutta, R. Han, and K. Pister, "Wireless Robotic Materials," in *Proceedings of the 15th ACM Conference on Embedded Network Sensor Systems*, 2017, pp. 1–6.
- [127] D. Bertozzi, G. Dimitrakopoulos, J. Flich, and S. Sonntag, "The Fast Evolving Landscape of On-Chip Communication," *Design Automation for Embedded Systems*, vol. 19, no. 1, pp. 59–76, 2015.
- [128] A. Ganguly, K. Chang, S. Deb, P. P. Pande, B. Belzer, and C. Teuscher, "Scalable Hybrid Wireless Network-on-Chip Architectures for Multicore Systems," *IEEE Transactions on Computers*, vol. 60, no. 10, pp. 1485–1502, 2010.
- [129] S. Saxena, D. S. Manur, N. Mansoor, and A. Ganguly, "Scalable and Energy Efficient Wireless Inter Chip Interconnection Fabrics Using THz-Band Antennas," *Journal of Parallel and Distributed Computing*, vol. 139, pp. 148–160, 2020.
- [130] S. Balasubramaniam and J. Kangasharju, "Realizing the Internet of Nano Things: Challenges, Solutions, and Applications," *Computer*, vol. 46, no. 2, pp. 62–68, 2012.
- [131] A. O. Balghusoon and S. Mahfoudh, "Routing protocols for wireless nanosensor networks and internet of nano things: A comprehensive survey," *IEEE Access*, vol. 8, pp. 200 724–200 748, 2020.
- [132] Z. Rong, M. S. Leeson, M. D. Higgins, and Y. Lu, "Simultaneous Wireless Information and Power Transfer for AF Relaying Nanonetworks in the Terahertz Band," *Nano communication networks*, vol. 14, pp. 1–8, 2017.
- [133] C. Liaskos and A. Tsioliariidou, "A Promise of Realizable, Ultra-Scalable Communications at Nano-Scale: A Multi-Modal Nano-Machine Architecture," *IEEE Transactions on Computers*, vol. 64, no. 5, pp. 1282–1295, 2014.
- [134] A. Tsioliariidou, C. Liaskos, S. Ioannidis, and A. Pitsillides, "Lightweight, Self-Tuning Data Dissemination for Dense Nanonetworks," *Nano Communication Networks*, vol. 8, pp. 2–15, 2016.
- [135] M. Pierobon, J. M. Jornet, N. Akkari, S. Almasri, and I. F. Akyildiz, "A Routing Framework for Energy Harvesting Wireless Nanosensor Networks in the Terahertz Band," *Wireless networks*, vol. 20, no. 5, pp. 1169–1183, 2014.
- [136] J. Xu, J. Jiang, Z. Wang, and Y. Zhao, "Energy Harvesting Based Opportunistic Routing for Mobile Wireless Nanosensor Networks," in *International Conference on Wireless Algorithms, Systems, and Applications*, Springer, 2018, pp. 760–766.
- [137] A. Oukhatar, M. Bakhouya, D. El Ouadghiri, and K. Zine-Dine, "Probabilistic-Based Broadcasting for EM-Based Wireless Nanosensor Networks," in *Proceedings of the 15th International Conference on Advances in Mobile Computing & Multimedia*, 2017, pp. 232–236.

- [138] F. Afsana, S. Mamun, M. Kaiser, and M. Ahmed, "Outage Capacity Analysis of Cluster-Based Forwarding Scheme for Body Area Network Using Nano-Electromagnetic Communication," in *2015 2nd international conference on electrical information and communication technologies (EICT)*, IEEE, 2015, pp. 383–388.
- [139] F. Afsana, N. Jahan, and M. Kaiser, "An Energy Efficient Cluster Based Forwarding Scheme for Body Area Network Using Nano-Scale Electromagnetic Communication," in *2015 IEEE International WIE Conference on Electrical and Computer Engineering (WIECON-ECE)*, IEEE, 2015, pp. 491–494.
- [140] F. Afsana, M. Asif-Ur-Rahman, M. R. Ahmed, M. Mahmud, and M. S. Kaiser, "An energy conserving routing scheme for wireless body sensor nanonet-work communication," *IEEE Access*, vol. 6, pp. 9186–9200, 2018.
- [141] G. Piro, G. Boggia, and L. A. Grieco, "On the Design of an Energy-Harvesting Protocol Stack for Body Area Nano-NETworks," *Nano Communication Networks*, vol. 6, no. 2, pp. 74–84, 2015.
- [142] N. Rikhtegar, R. Javidan, and M. Keshtgari, "Mobility Management in Wireless Nano-Sensor Networks Using Fuzzy Logic," *Journal of Intelligent & Fuzzy Systems*, vol. 32, no. 1, pp. 969–978, 2017.
- [143] C. Liaskos, A. Tsioliaridou, S. Ioannidis, N. Kantartzis, and A. Pitsillides, "A Deployable Routing System for Nanonetworks," in *2016 IEEE International Conference on Communications (ICC)*, IEEE, 2016, pp. 1–6.
- [144] A. Tsioliaridou, C. Liaskos, S. Ioannidis, and A. Pitsillides, "CORONA: A Co-ordinate and Routing System for Nanonetworks," in *Proceedings of the second annual international conference on nanoscale computing and communication*, 2015, pp. 1–6.
- [145] A. Tsioliaridou, C. Liaskos, L. Pachis, S. Ioannidis, and A. Pitsillides, "N3: Addressing and Routing in 3D Nanonetworks," in *2016 23rd International Conference on Telecommunications (ICT)*, IEEE, 2016, pp. 1–6.
- [146] A. Tsioliaridou, C. Liaskos, E. Dedu, and S. Ioannidis, "Stateless Linear-Path Routing for 3D Nanonetworks," in *Proceedings of the 3rd ACM International Conference on Nanoscale Computing and Communication*, 2016, pp. 1–6.
- [147] A. Tsioliaridou, C. Liaskos, E. Dedu, and S. Ioannidis, "Packet Routing in 3D Nanonetworks: A Lightweight, Linear-Path Scheme," *Nano communication networks*, vol. 12, pp. 63–71, 2017.
- [148] B. Liu, Y. Zhang, X. Jiang, and Z. Wu, "An Energy-Efficient Data Collection Scheme in Body Area Nanonetworks," in *2015 Third International Symposium on Computing and Networking (CANDAR)*, IEEE, 2015, pp. 240–245.
- [149] B. Liu, P. Lu, X. Hao, X. Jiang, and Z. Wu, "Data Collection Scheme Based on Wake-Up in Body Area Nanonetworks," in *2016 International Conference on Networking and Network Applications (NaNA)*, IEEE, 2016, pp. 438–443.

- [150] J. Chen, Z. Wu, H. Liu, X. Wang, and B. Liu, "Node Priority Strategy for Energy Efficient Data Collection Scheme in Wireless Body Area Networks," in *Proceedings of the 2017 2nd International Conference on Communication and Information Systems*, 2017, pp. 49–53.
- [151] R. Alsheikh, N. Akkari, and E. Fadel, "MAC Protocols for Wireless Nano-Sensor Networks: Performance Analysis and Design Guidelines," in *2016 Sixth International Conference on Digital Information Processing and Communications (ICDIPC)*, IEEE, 2016, pp. 129–134.
- [152] J. M. Jornet, J. C. Pujol, and J. S. Pareta, "PHLAME: A Physical Layer Aware MAC Protocol for Electromagnetic Nanonetworks in the Terahertz Band," *Nano Communication Networks*, vol. 3, no. 1, pp. 74–81, 2012.
- [153] S. Ghafoor, N. Boujnah, M. H. Rehmani, and A. Davy, "MAC Protocols for Terahertz Communication: A Comprehensive Survey," *IEEE Communications Surveys & Tutorials*, vol. 22, no. 4, pp. 2236–2282, 2020.
- [154] D. Arifler, "Link Layer Modeling of Bio-Inspired Communication in Nanonetworks," *Nano Communication Networks*, vol. 2, no. 4, pp. 223–229, 2011.
- [155] S. D'Oro, L. Galluccio, G. Morabito, and S. Palazzo, "A Timing Channel-Based MAC Protocol for Energy-Efficient Nanonetworks," *Nano Communication Networks*, vol. 6, no. 2, pp. 39–50, 2015.
- [156] S. J. Lee, C. Jung, K. Choi, and S. Kim, "Design of Wireless Nanosensor Networks for Intrabody Application," *International Journal of Distributed Sensor Networks*, vol. 11, no. 7, p. 176761, 2015.
- [157] S. J. Lee, H. Choi, and S. Kim, "Slotted CSMA/CA Based Energy Efficient MAC Protocol Design in Nanonetworks," *International Journal of Wireless & Mobile Networks (IJWMN) Vol*, vol. 10, 2018.
- [158] J. Xu, J. Kan, and Y. Zhang, "Centralized Energy Harvesting-Based TDMA Protocol for Terahertz Nanosensor Networks," *Sensors*, vol. 19, no. 20, p. 4508, 2019.
- [159] N. Akkari, P. Wang, J. M. Jornet, *et al.*, "Distributed timely throughput optimal scheduling for the internet of nano-things," *IEEE Internet of Things Journal*, vol. 3, no. 6, pp. 1202–1212, 2016.
- [160] R. Alsheikh, N. Akkari, and E. Fadel, "Grid Based Energy-Aware MAC Protocol for Wireless Nanosensor Network," in *2016 8th IFIP International Conference on New Technologies, Mobility and Security (NTMS)*, 2016, pp. 1–5.
- [161] H. Yu, B. Ng, and W. K. Seah, "Pulse Arrival Scheduling for Nanonetworks under Limited IoT Access Bandwidth," in *2017 IEEE 42nd Conference on Local Computer Networks (LCN)*, IEEE, 2017, pp. 18–26.

- [162] X.-W. Yao, C.-C. Wang, W.-L. Wang, and J. M. Jornet, "On the Achievable Throughput of Energy-Harvesting Nanonetworks in the Terahertz Band," *IEEE Sensors Journal*, vol. 18, no. 2, pp. 902–912, 2017.
- [163] S. Mohrehkesh, M. C. Weigle, and S. K. Das, "DRIH-MAC: A Distributed Receiver-Initiated Harvesting-Aware MAC for Nanonetworks," *IEEE Transactions on Molecular, Biological and Multi-Scale Communications*, vol. 1, no. 1, pp. 97–110, 2015.
- [164] S. Mohrehkesh and M. C. Weigle, "RIH-MAC: Receiver-Initiated Harvesting-Aware MAC for Nanonetworks," in *Proceedings of ACM The First Annual International Conference on Nanoscale Computing and Communication*, 2014, pp. 1–9.
- [165] —, "Optimizing Energy Consumption in Terahertz Band Nanonetworks," *IEEE Journal on Selected Areas in Communications*, vol. 32, no. 12, pp. 2432–2441, 2014.
- [166] P. Wang, J. M. Jornet, M. A. Malik, N. Akkari, and I. F. Akyildiz, "Energy and Spectrum-Aware MAC Protocol for Perpetual Wireless Nanosensor Networks in the Terahertz Band," *Ad Hoc Networks*, vol. 11, no. 8, pp. 2541–2555, 2013.
- [167] V Srikanth, S. Chaluvadi, *et al.*, "Energy Efficient, Scalable and Reliable MAC Protocol for Electromagnetic Communication among Nano Devices," *International Journal of Distributed and Parallel Systems*, vol. 3, no. 1, p. 249, 2012.
- [168] G. Piro, L. A. Grieco, G. Boggia, and P. Camarda, "Nano-Sim: Simulating Electromagnetic-Based Nanonetworks in the Network Simulator 3.," in *SimuTools*, 2013, pp. 203–210.
- [169] Q. Li, X.-W. Yao, and C.-C. Wang, "RBMP: A Relay-Based MAC Protocol for Nanonetworks in the Terahertz Band," in *Proceedings of the 4th ACM International Conference on Nanoscale Computing and Communication*, 2017, pp. 1–2.
- [170] A. Afsharinejad, A. Davy, and B. Jennings, "Dynamic Channel Allocation in Electromagnetic Nanonetworks for High Resolution Monitoring of Plants," *Nano Communication Networks*, vol. 7, pp. 2–16, 2016.
- [171] E. Zarepour, M. Hassan, C. T. Chou, and A. A. Adesina, "Frequency Hopping Strategies for Improving Terahertz Sensor Network Performance over Composition Varying Channels," in *Proceeding of IEEE International Symposium on a World of Wireless, Mobile and Multimedia Networks 2014*, IEEE, 2014, pp. 1–9.
- [172] Q. Xia, Z. Hossain, M. Medley, and J. M. Jornet, "A Link-Layer Synchronization and Medium Access Control Protocol for Terahertz-Band Communication Networks," *IEEE Transactions on Mobile Computing*, vol. 20, no. 1, pp. 2–18, 2019.

- [173] —, “A Link-Layer Synchronization and Medium Access Control Protocol for Terahertz-Band Communication Networks,” in *2015 IEEE Global Communications Conference (GLOBECOM)*, IEEE, 2015, pp. 1–7.
- [174] J. M. Jornet and I. F. Akyildiz, “Information Capacity of Pulse-Based Wireless Nanosensor Networks,” in *2011 8th Annual IEEE Communications Society Conference on Sensor, Mesh and Ad Hoc Communications and Networks*, IEEE, 2011, pp. 80–88.
- [175] F. Vullum and D. Teeters, “Investigation of Lithium Battery Nanoelectrode Arrays and Their Component Nanobatteries,” *Journal of Power Sources*, vol. 146, no. 1-2, pp. 804–808, 2005.
- [176] N. Liu, Z. Lu, J. Zhao, *et al.*, “A Pomegranate-Inspired Nanoscale Design for Large-Volume-Change Lithium Battery Anodes,” *Nature nanotechnology*, vol. 9, no. 3, pp. 187–192, 2014.
- [177] X. Yao, D. Ma, and C. Han, “ECP: A Probing-Based Error Control Strategy for THz-Based Nanonetworks With Energy Harvesting,” *IEEE Access*, vol. 7, pp. 25 616–25 626, 2019.
- [178] G. Piro, P. Bia, G. Boggia, D. Caratelli, L. A. Grieco, and L. Mescia, “Terahertz Electromagnetic Field Propagation in Human Tissues: A Study on Communication Capabilities,” *Nano Communication Networks*, vol. 10, pp. 51–59, 2016.
- [179] G. Piro, K. Yang, G. Boggia, N. Chopra, L. A. Grieco, and A. Alomainy, “Terahertz communications in human tissues at the nanoscale for healthcare applications,” *IEEE Transactions on Nanotechnology*, vol. 14, no. 3, pp. 404–406, 2015.
- [180] S. F. Bush, J. L. Paluh, G. Piro, V. Rao, R. V. Prasad, and A. Eckford, “Defining Communication at the Bottom,” *IEEE Transactions on Molecular, Biological and Multi-Scale Communications*, vol. 1, no. 1, pp. 90–96, 2015.
- [181] H. Khalil, *Nonlinear Systems: Pearson New International Edition*. Always Learning, Pearson Education Limited, 2013.
- [182] J. M. Jornet and I. F. Akyildiz, “Femtosecond-Long Pulse-Based Modulation for Terahertz Band Communication in Nanonetworks,” *IEEE Transactions on Communications*, vol. 62, no. 5, pp. 1742–1754, 2014.
- [183] V. Jamali, A. Ahmadzadeh, W. Wicke, A. Noel, and R. Schober, “Channel Modeling for Diffusive Molecular Communication—A Tutorial Review,” *Proc. IEEE*, vol. 107, no. 7, pp. 1256–1301, 2019.
- [184] M. Mukherjee, H. B. Yilmaz, B. Bhowmik, J. Lloret, and Y. Lv, “Synchronization for Diffusion-Based Molecular Communication Systems via Faster Molecules,” in *Proc. IEEE ICC*, 2019, pp. 1–5.

- [185] H. ShahMohammadian, G. G. Messier, and S. Magierowski, "Blind Synchronization in Diffusion-Based Molecular Communication Channels," *IEEE Commun. Lett.*, vol. 17, no. 11, pp. 2156–2159, 2013.
- [186] M. Pierobon and I. F. Akyildiz, "Diffusion-Based Noise Analysis for Molecular Communication in Nanonetworks," *IEEE Transactions on signal processing*, vol. 59, no. 6, pp. 2532–2547, 2011.
- [187] S. P. Badwal, S. S. Giddey, C. Munnings, A. I. Bhatt, and A. F. Hollenkamp, "Emerging Electrochemical Energy Conversion and Storage Technologies," *Frontiers in chemistry*, vol. 2, p. 79, 2014.
- [188] N. Farsad, W. Guo, and A. W. Eckford, "Tabletop Molecular Communication: Text Messages Through Chemical Signals," *PloS one*, vol. 8, no. 12, e82935, 2013.
- [189] K. Iniewski, *Circuits at the nanoscale: communications, imaging, and sensing*. CRC Press, 2018.
- [190] Z. Cheng, Y. Zhang, and M. Xia, "Performance Analysis of Diffusive Mobile Multiuser Molecular Communication With Drift," *IEEE Transactions on Molecular, Biological and Multi-Scale Communications*, vol. 4, no. 4, pp. 237–247, 2018.
- [191] T. Nakano, Y. Okaie, and A. V. Vasilakos, "Transmission Rate Control for Molecular Communication among Biological Nanomachines," *IEEE Journal on Selected Areas in Communications*, vol. 31, no. 12, pp. 835–846, 2013.
- [192] H. K. Rudsari, M. R. Javan, M. Orooji, N. Mokari, and E. A. Jorswieck, "Multiple-Type Transmission Multiple-Type Reception Framework on Molecular Communication," *IEEE Wireless Commun. Lett.*, vol. 9, no. 11, pp. 1825–1829, 2020.
- [193] B. C. Akdeniz, M. Egan, and B. Q. Tang, "Equilibrium Signaling: Molecular Communication Robust to Geometry Uncertainties," *IEEE Transactions on Communications*, 2020.
- [194] N. Tavakkoli, P. Azmi, and N. Mokari, "Performance Evaluation and Optimal Detection of Relay-Assisted Diffusion-Based Molecular Communication with Drift," *IEEE transactions on nanobioscience*, vol. 16, no. 1, pp. 34–42, 2016.
- [195] X. Chen, M. Wen, C.-B. Chae, L.-L. Yang, F. Ji, and K. K. Igorevich, "Resource allocation for multi-user molecular communication systems oriented to the internet of medical things," *IEEE Internet of Things Journal*, 2021.
- [196] S. K. Tiwari, T. R. T. Reddy, P. K. Upadhyay, and D. B. Da Costa, "Joint optimization of molecular resource allocation and relay positioning in diffusive nanonetworks," *IEEE Access*, vol. 6, pp. 67 681–67 687, 2018.

- [197] Y. Fang, A. Noel, N. Yang, A. W. Eckford, and R. A. Kennedy, "Symbol-by-symbol maximum likelihood detection for cooperative molecular communication," *IEEE Transactions on Communications*, vol. 67, no. 7, pp. 4885–4899, 2019.
- [198] A. Aijaz and A. Aghvami, "Error Performance of Diffusion-Based Molecular Communication Using Pulse-Based Modulation," *IEEE Trans. NanoBiosci.*, vol. 14, no. 1, pp. 146–151, 2015.
- [199] H. ShahMohammadian, G. G. Messier, and S. Magierowski, "Nano-Machine Molecular Communication over a Moving Propagation Medium," *Nano Communication Networks*, vol. 4, no. 3, pp. 142–153, 2013.
- [200] F. Zabini, "Spatially distributed molecular communications via diffusion: Second-order analysis," *IEEE Transactions on Molecular, Biological and Multi-Scale Communications*, vol. 5, no. 2, pp. 112–138, 2019.